Citation:

See this record in the RMIT Research Repository at:

http://researchbank.rmit.edu.au/view/rmit:22350

Version: Accepted Manuscript

Link to Published Version:

http://dx.doi.org/10.1016/j.pmatsci.2013.06.003

Transition metal oxides - thermoelectric properties

Sumeet Walia,[a]* Sivacarendran Balendhran,[a] Hussein Nili,[a,b] Serge Zhuiykov,[c] Gary Rosengarten,[d] Qing Hua Wang,[e] Madhu Bhaskaran,[a,b] Sharath Sriram,[a,b] Michael S. Strano[e] and Kourosh Kalantar-zadeh[a]*

[a] School of Electrical and Computer Engineering, RMIT University, Melbourne, Australia

[b] Functional Materials and Microsystems Research Group, RMIT University, Melbourne, Australia

[c] Materials Science and Engineering Division, CSIRO, Highett, Victoria, Australia

[d] School of Aerospace, Mechanical and Manufacturing Engineering, RMIT University, Melbourne, Australia

[e] Department of Chemical Engineering, Massachusetts Institute of Technology, Cambridge, Massachusetts, USA.

*Corresponding author emails: kourosh.kalantar@rmit.edu.au, and sumeet.walia@rmit.edu.au

RMIT University, GPO 2476, Melbourne-3000, Victoria, Australia.

Ph: + 61-3-9925-3254

Abstract

Transition metal oxides (TMOs) are a fascinating class of materials due to their wide ranging electronic, chemical and mechanical properties. Additionally, they are gaining increasing attention for their thermoelectric (TE) properties due to their high temperature stability, tunable electronic and phonon transport properties and well established synthesis techniques. In this article, we review TE TMOs at cryogenic, ambient and high temperatures. An overview of strategies used for morphological, composting and stoichiometric tuning of their key TE parameters is presented. This article also provides an outlook on the current and future prospects of implementing TMOs for a wide range of TE applications.

Keywords: transition metal oxides, thermoelectric, Seebeck coefficient, electrical conductivity, thermal conductivity, doping, stoichiometry, compositing, nanostructuring

Table of Contents

Nomenclature

Acronyms

TE	Thermoelectric
TMOs	Transition metal oxides
TPF	Thermoelectric power factor
QDSL	Quantum dot superlattice
SNW	Segmented nanowire
DOS	Density of states
2DEG	Two-dimensional electron gas
RTA	Relaxation time approximation
DFT	Density functional theory
SPS	Spark plasma sintering
EBE	Electron beam evaporation
RF	Radio frequency
PLD	Pulsed laser deposition
ALD	Atomic layer deposition
MBE	Molecular beam epitaxy
CVD	Chemical vapour deposition
MOCVD	Metal organic chemical vapour deposition
VDWE	Van der Waals epitaxy
SSR	Solid state reaction
GPR	Gas phase reaction
LPR	Liquid phase reaction
STEG	Solar thermoelectric generator
RITEG	Radio isotope thermoelectric generator
LED	Light emitting diode

1 Introduction

Thermoelectric (TE) materials are utilized for the conversion of a temperature gradient to a voltage gradient and *vice versa*. TE materials are widely regarded as the materials that can provide potential solutions for power generation and refrigeration technologies as well as their future advancements[1-4]. Additionally, they offer opportunities for the development of technologies in areas such as smart sensors, energy harvesting, and the new concept of thermopower wave sources[5-9].

Transition metal oxides (TMOs) are a vast but conventionally less widely studied family of TE materials, which include materials such as titanium, manganese, tungsten, zinc, copper, vanadium, cobalt, rhodium, and molybdenum oxides. However, these materials are now drawing increasing attention. Metal oxides can show a wide range of electronic properties ranging from insulating to semiconducting and conducting[10]. Their electronic properties can be engineered by changing their morphology, doping and stoichiometry. The phonon generation and propagation properties in many TMOs are well understood and molecular engineering methods have been developed for tuning them. Additionally, TMOs show a wide range of interesting thermal properties at cryogenic, ambient and high temperatures (Fig. 1). Many TMOs offer high Seebeck coefficients, with desired thermal and electrical conductivities and heat capacities, at targeted temperatures that can be exploited for different applications[11-14]. Their abundance in nature is another important advantage for technologies to be widely adopted.

Despite all the aforementioned promising properties, TMOs have yet to achieve their true potential in the TE realm. This review article will provide a comprehensive outlook on the TE properties of various TMOs and assess their performance. The critical parameters of thermal conductivity, electrical conductivity and Seebeck coefficient will be thoroughly discussed. The effect of changing the morphology and nanostructuring on the thermal and electrical

6

conductivities and Seebeck coefficient of TMOs will be presented. Critical discussions on different types of TMOs and the effect of oxidation, reduction and dopants on their TE properties will also be presented. This paper will discuss the most significant recent advances in the development of metal oxides for a wide range of applications including conventional purposes such as waste heat harvesting, refrigeration, and sensors as well as new concepts such as thermopower waves. Finally, we will provide an outlook for future directions and applications for TMOs in TEs at a range of operating temperatures.
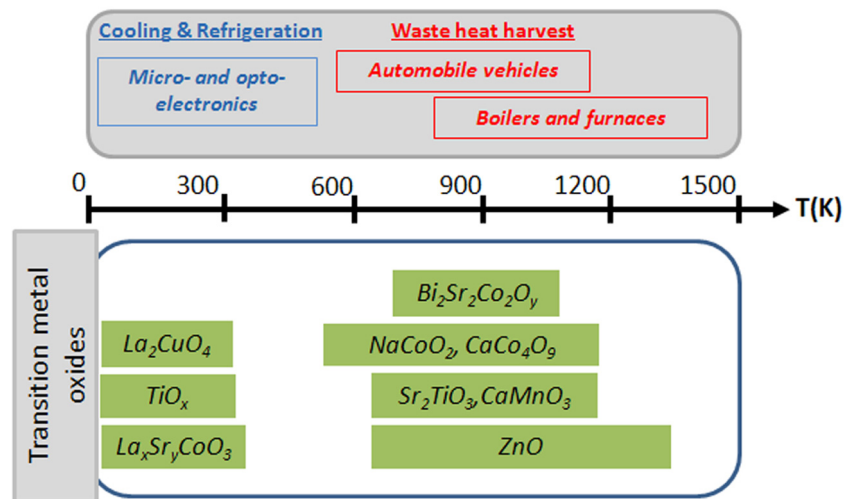
Fig. 1. Operating temperature ranges of various TMOs and TMO composites. (Reproduced with permission from [15].)

2 Basic principles of thermoelectricity in TMOs

The fundamental factors that govern TE properties are thermal conductivity (κ), electrical conductivity (σ) and Seebeck coefficient (S). The performance of TE materials is generally assessed by the figures of merit (ZT) defined as $S^2\sigma/\kappa$, and the thermoelectric power factor (TPF) defined as $S^2\sigma$. In this section, we present an overview of the main equations governing the aforementioned TE parameters for bulk three dimensional (3D) and low dimensional (2D, 1D and 0D) structures.

2.1 Thermal conductivity κ

Thermal conductivity is the ability of a material to conduct heat. The main contributors to the thermal conductivity are phonons and charge carriers (electrons and holes). The overall thermal conductivity (κ_{total}) of a material is defined as: [16, 17]

$$\kappa_{total} = \kappa_{phonon} + \kappa_{electron} \qquad (1)$$

where, κ_{phonon} is the lattice thermal conductivity due to acoustic phonons travelling through the crystal lattice and $\kappa_{electron}$ is the electronic thermal conductivity due to charge carriers. Phonons and charge carriers can undergo scattering due to other phonons, lattice defects, impurities, electrons, grain boundaries and interfaces[18]. Such scattering then results in changes of thermal conductivity. The fundamentals of κ_{phonon} and $\kappa_{electron}$ for bulk as well as low dimensional materials are discussed next.

2.1.1 Bulk (3D) materials

For semiconducting and insulating TMOs, acoustic phonons are the major contributors to κ_{total}. However, for highly doped and non-stoichiometric TMOs the electronic thermal conductivity also plays an important role. For bulk materials, the kinetic theory of gases defines the κ_{phonon} and $\kappa_{electron}$ as:

$$\kappa_{phonon} = \frac{1}{3} \upsilon_s C_v L_{ph} \tag{2a}$$

$$\kappa_{electron} = \frac{1}{3} c_v \upsilon \Lambda = L\sigma T \tag{2b}$$

where υ_s is the velocity of sound, C_v is the heat capacity at constant volume, L_{ph} is the phonon mean free path, c_v is the electronic specific heat per volume, v is the electron velocity that can be assumed to be the Fermi velocity v_F, Λ is the electron mean free path, L is the Lorenz number (2.45×10^{-8} $V^2.K^2$), σ is the electrical conductivity, and T is the temperature in Kelvin.

C_v and υ_s are typically temperature independent for $T > 300K$; hence at high temperatures, κ_{phonon} primarily depends on L_{ph} and can be largely attributed to phonon-phonon scattering[19].

On the other hand, $\kappa_{electron}$ depends on the electron mean free path. The Wiedemann-Franz law as shown in Eq. 2b states that $\kappa_{electron}$ is directly proportional to σ and T, so that any variation in $\kappa_{electron}$ affects σ. Hence, the only TE parameter that is independent of the electronic band structure is κ_{phonon}.

In semiconducting and insulating TMOs, phonons are the majority contributors to κ_{total}, making it possible to tune their κ_{total} with a negligible effect on σ. A comprehensive theoretical analysis of κ has been provided elsewhere[17]. In order to improve the performance of TE materials for conventional applications such as cooling and energy scavenging, a reduction in κ_{phonon} is desirable. In theory, the minimum κ_{phonon} is achieved when the mean free path of the phonons is no more than the interatomic spacing of the constituent atoms[4]. Limiting L_{ph} by confining phonons can help achieve this goal. Such a confinement can be obtained by creating low dimensional materials, which are described next.

2.1.2 2D materials

A two-dimensional (2D) quantum well structure consists of a very thin layer of material that is nanometers thick in one dimension and semi-infinitely large in the other two dimensions. 2D quantum well structures are likely to reduce the κ_{total} of TMOs compared to their bulk counterparts because phonons mainly scatter at the interfaces, while the motion of the electrons can be confined parallel to the layers. $\kappa_{electron2D}$ is a strong function of the thickness of layers (W). For 2D quantum well structures, $\kappa_{phonon2D}$ and $\kappa_{electron2D}$ along the x-axis (Fig. 2a) have been defined as:[20, 21]

$$\kappa_{phonon2D} = \frac{k_B}{2\pi^2 v}\left(\frac{k_B}{h}\right)^3 T^3 \int_0^{\theta/T} \frac{\tau_c \xi^4 e^\xi}{(e^\xi - 1)^2} d\xi \qquad (3a)$$

$$\kappa_{electron2D} = \frac{\tau h^2}{4\pi W}\left(\frac{2k_B T}{h^2}\right)^2 \left(\frac{m_y}{m_x}\right)^{1/2} k_B \left(3F_2 - 4\frac{F_1^2}{F_0}\right) \qquad (3b)$$

where, k_B is the Boltzmann constant, h is the Planck constant, e is the electron charge, $m_{x,y,z}$ are the three components of the effective mass, θ is the Debye temperature, $\xi = h\omega/k_B T$ ($h\omega$ being the phonon energy), T is the absolute temperature, τ is the electron relaxation time and is defined as $\tau = \mu_x m_x/e$ where μ_x is the mobility along the x-axis (Fig. 2a), v is the velocity of sound, F_i are the Fermi-Dirac functions and τ_c is the combined phonon relaxation time due to all resistive processes (which include boundary scattering, mass difference scattering, scattering at dislocations and Umklapp scattering processes), which is governed by the Matthiessen's rule (see ref. [21] for details). According to Eq. 3a, the theoretical value of $\kappa_{phonon2D}$ is strongly influenced by the phonon-phonon energy, its relaxation time τ_c, which is a function of the quantum well dimension and temperature.

$\kappa_{electron2D}$ depends only on two effective mass components of the electrons as shown in Eq.3b. This is because, unlike phonons, electrons can only move in a 2D motion parallel to the

10

layers due to the quantum confinement. Additionally, a stronger confinement (by decreasing W) is expected to increase $\kappa_{electron2D}$. However, the result of reducing W is generally a decrease in the overall thermal conductivity. This is especially useful in engineering ZT when both Seebeck coefficient and electrical conductivity of the material remain constant. There are practical examples of employing 2D TMOs such as TiO_2, cobalt oxides and manganese oxides[22] which will be discussed in their relevant sections. The application of 2D TMOs with increased ZT values [22] has been demonstrated in energy scavenging at elevated temperatures that will also be discussed later.

2.1.3 1D materials

Hicks *et al.* developed a theoretical model and predicted that materials in 1D form (such as quantum wires, nanobelts and nanorods) can result in further reduction of $\kappa_{electron}$, compared to bulk and 2D structures[23]. The thermal conductivity of phonons in 1D structures were theoretically modelled by Zou and Balandin.[24] The equations describing κ_{phonon} and $\kappa_{electron}$ for 1D structures are: [23, 24]

$$\kappa_{phonon1D} = \frac{k_B}{2\pi^2 v}\left(\frac{k_B}{h}\right)^3 T^3 \int_0^{\theta/T} \frac{\tau_c \xi^4 e^\xi}{(e^\xi - 1)^2}d\xi \times \left[1 - \frac{24}{\pi}G(\eta(\xi),p)\right]d\xi \qquad (4a)$$

$$\kappa_{electron1D} = \frac{2\tau}{\pi a^2}\left(\frac{2k_B T}{h^2}\right)^{1/2}(m_x)^{-1/2}k_B{}^2 T\left(\frac{5}{2}F_{3/2} - \frac{9F_{1/2}{}^2}{2F_{-1/2}}\right) \qquad (4b)$$

where, a is the width of a 1D structure with a square cross section, m_x is the effective mass component in the x direction (Fig. 2b), v is the phonon group velocity, T is the temperature, θ is the Debye temperature, $\xi = h\omega/k_B T$ ($h\omega$ being the phonon energy), Λ is the phonon mean free path ($\Lambda(\xi) = v(\xi)\tau_c(\xi)$), η is the ratio between the wire width and Λ ($\eta(\xi) = a\pi/\Lambda(\xi)$), p is a parameter which characterizes the interface roughness and its effect on the phonon scattering.

The value of p represents the probability of a phonon undergoing diffusive scattering (refer to [24] for additional details). Other parameters have been defined in Eq. 3a & 3b.

The theoretical ZT calculations using Eqs.4a and 4b for a 1D structure show that it strongly depends on its width. For widths smaller than the thermal de Broglie wavelength of the carriers, the ZT increases significantly with decreasing the width of the 1D structure. TMOs such as ZnO and TiO_2 have been extensively synthesised in 1D morphologies (nanorods, nanoribons and nanotubes) [25, 26] and the thermal conductivity of such materials are strongly affected by such morphological manipulations[25].

2.1.4 0D materials

Unlike 2D or 1D structures, the carriers in 0D structures such as quantum dots are confined in all directions. The transport mechanism in 0D structures is thus different from others, in the sense that unconventional conduction behaviour such as tunnelling is required to maintain its electronic conductivity. Therefore, 0D structures such as quantum dot superlattices (QDSLs) and segmented nanowires (SNWs) were proposed to provide a conduction pathway. As the name suggests, such segmented structures consist of a series of interwoven quantum dots of two different materials (Fig.2c). The electronic transport along the wire axis occurs by tunnelling between adjacent quantum dots. Furthermore, due to the wire boundaries and interfaces between the quantum dots, the phonon conduction along the wire axis is impeded, resulting in a reduced lattice thermal conductivity.

The lattice thermal conductivity for 0D structures ($\kappa_{phonon0D}$) such as QDSLs and SNWs comprising of two different materials A and B is defined as:[27, 28]

$$\frac{L}{\kappa_{phonon0D}} = \frac{L_A}{\kappa_{phononA}} + \frac{L_B}{\kappa_{phononB}} + 4\left(\frac{1}{C_A v_A t_{AB}} + \frac{1}{C_B v_B t_{BA}}\right)\left(1 - \frac{t_{AB} + t_{BA}}{2}\right) \quad (5)$$

$$+ \frac{3}{d_w}\left(\frac{L_A}{C_A v_A \propto_A} + \frac{L_B}{C_B v_B \propto_B}\right)$$

where, $C_{A,B}$ is the heat capacity, $v_{A,B}$ is the sound velocity of the nanodot material, $L_{A,B}$ is the length of the material's segment, t_{AB} and t_{BA} are the average transmissivity of phonons from quantum dot A to B and vice versa, $\alpha_{A,B}$ is the geometric factor that depends on the aspect ratio (L_A/d_w or L_B/d_w) of the quantum dots in which d_w is the diameter of the wire. The first two terms in Eq.5 account for the intrinsic phonon scattering events, while the third and fourth terms account for the contribution of the segment interface and the wire boundary scattering processes to the $\kappa_{phonon0D}$. It is evident that the segment length, the choice of materials A and B, as well as the aspect ratio of the quantum dots play a vital role in determining $\kappa_{phonon0D}$ and hence, the design of the QDSL or SNW structure is the most important factor governing the thermal properties. In order to quantify the electronic contribution of the thermal conductivity ($\kappa_{electron0D}$) in a QDSL or SNW structure, the Kroenig-Penney model is used. This model determines the dispersion relation $E_{n,m}(k)$ for the electrons that move along the axis in the n,m sub-band of the wire experiencing a square periodic potential[29], where k is a 1D wave vector that describes the energies of these electrons in the square potential[28]. The electronic band structure of each sub-band is highly dependent on the segment length (L_A or L_B), the potential barrier height and the transport effective masses[28].

The constant relaxation time approximation is used for calculating the following fundamental integrals for the conduction band: [27]

$$K_{(\alpha)} = \frac{4\tau}{\pi^2 h^2 d_w^2} \sum_{n,m} \int \frac{1}{g_{n,m}(E)} (E_{n,m} - E_F)^\alpha \left(-\frac{\delta f}{\delta E} \right) dE \tag{6a}$$

$$g_{n,m}(E) = \frac{2}{\pi} \left(\frac{\delta E_{n,m}}{\delta \kappa} \right)^{-1} \tag{6b}$$

where, α=0,1 or 2, τ is the relaxation time of the carriers, E_F is the Fermi energy, $f(E)$ is the Fermi-dirac distribution function and $g_{n,m}(E)$ is the density of states of the n,m sub-band,

13

which is defined in Eq. 6b. The electronic component of the lattice thermal conductivity in 0D structures ($\kappa_{electron0D}$) is defined as:[27]

$$\kappa_{electron0D} = \frac{1}{T}\left(K_{(2)} - \frac{K_{(1)}^2}{K_{(0)}}\right)^{1/2} \tag{7}$$

From Eq. 6a, b & 7, it is clear that $\kappa_{electron0D}$ is strongly dependent on the diameter of the SNWs, as well as the carrier relaxation time. However, as discussed before, the electronic contribution towards the thermal conductivity in semiconducting TMOs is generally much lower, compared to the phonon contribution at small diameters. The superlattice interfaces in TMO-based 0D structures such as SNWs are expected to enhance the phonon scattering to further suppress the thermal conductivity compared to the bulk form[30].

The above discussion shows that a reduction in the dimensionality of the system can result in a reduced lattice thermal conductivity, due to the phonon mean free paths being limited by the nanostructuring, and consequently increased phonon scattering. This can potentially enhance the efficiency of TE TMOs for energy scavenging applications, while can increase the performance of temperature sensors, which are based on such structures.

2.2 Electrical conductivity σ

The electrical conductivity of TMOs in bulk and low dimensional form has been extensively studied[31-34]. Most TMOs exhibit low σ in their bulk due to low mobilities of charge carriers[35]. However, it has been shown that quantum confinement of these carriers alters the electronic density of states (DOS). Various nanostructuring and doping techniques can be employed to alter the carrier concentrations by adjusting the bandgap and surface energy in TMOs[31]. In this section, we will discuss the theoretical equations that govern the electrical conductivity of TMOs in bulk and low dimensional forms.

2.2.1 Bulk (3D) materials

For bulk TMOs, the electrical conductivity can be defined in a simplistic form as follows:[16, 29]

$$\sigma = n(E)e\mu(E) = n(E)e^2 \frac{\tau(E)}{m^*} \tag{8}$$

where, $n(E)$ is the density of carriers which is a function of the density of states $g(E)$, e is the electronic charge, $\mu(E)$ is the differential carrier mobility, $\tau(E)$ is the relaxation time and m^* is the carrier effective mass.

The m^* of many TE TMOs such as TiO_2 and layered cobalt oxides is relatively large.[16, 36] Additionally, they also suffer due to short relaxation times[37-39]. As a result, the charge carrier mobilities of many TMOs are relatively small. The carrier concentrations of bulk TMOs, which is affected by the thermionic effect, depend on their bandgap and temperature. As a result, the carrier mobilities and concentrations in TMOs can be tuned using various doping and nanostructuring techniques.

2.2.2 2D materials

The electrical conductivity of TMOs can be enhanced by fabricating quantum well structures, which result in the quantum confinement of carriers. For a 2D quantum well structure discussed previously in section 2.1.2, Hicks *et al.* defined the electrical conductivity (σ_{2D}) as:[20]

$$\sigma_{2D} = \frac{1}{2\pi W}\left(m_x^* m_y^*\right)^{1/2} F_0 e\mu_x \left(\frac{2k_B T}{h^2}\right) \tag{9}$$

where, W is the quantum well width, m_x^* and m_y^* are the effective mass components in the x and y direction (in the plane of the 2D material) respectively, F_0 is the Fermi energy, e is the electron charge, μ_x is the mobility, T is the temperature, k_B is the Boltzmann constant and h is

the Planck's constant. In such structures the electrons are confined only to a 2D motion that is parallel to the layers. Eq.9 shows that a reduction in W enhances σ_{2D}. In TMOs, the Fermi level can be adjusted using various doping techniques and methods that control stoichiometry. In these materials, the Fermi level is a strong function of morphology and the temperature[40]. As expected, enhanced electrical conductivities have been demonstrated in various 2D TMOs such as MoO_3, CoO_2 and ZnO nanobelts[41] [42] [43].

2.2.3 1D materials

In morphologies such as one-dimensional nanorods, nanotubes or nanobelts of TMOs, σ is predicted to increase by reducing the cross sectional area of the structure. Such enhancement is mainly due to increased charge carrier mobilities *via* changes in DOS[44, 45]. σ in such 1D structures is defined as:[23]

$$\sigma_{1D} = \frac{1}{\pi a^2} (m_x^*)^{1/2} F_{-1/2} e \mu_x \left(\frac{2k_B T}{h^2}\right)^{1/2} \tag{10}$$

where, a is the width of a 1D structure with a square cross section, m_x^* is the effective mass component in the x direction. Other parameters have been defined in Eq. 9. Additionally, σ can be tuned by changing the Fermi level of the TMOs, which result in the carrier concentration change as well[46] [47].

TMOs such as TiO_2 and ZnO are widely synthesised in various 1D morphologies[25, 26]. As predicted, σ in such quasi-1D structures is shown to increase compared to the bulk forms[46]. The carrier concentrations in such structures can be adjusted by the use of suitable dopants[46, 48]. There are many good review articles that cover the topic of electrical conductivity in various 1D TE TMO structures[46, 49].

16

2.2.4 0D materials

QDSL or SNW structures, described in section 2.1.4, allow for electrical conduction through mechanisms such as tunnelling or hopping. Well-separated discrete energy states of the segments alter the fundamental properties such as DOS and bandgap energy in an alternating manner along the 1D wire[50, 51]. At the same time, the 0D characteristics, and in particular the electrical conductivity, of each quantum dot is maintained by the energy differential of the conduction or valence bands between the two constituent materials that form the wire[28]. The electrical conductivity for such 0D structures is defined as: [27, 28]

$$\sigma_{0D} = e^2 K_{(0)} \qquad (11)$$

$K_{(\alpha)}$ is defined in Eq. 6a. It can be seen from Eq.11 that the σ_{0D} is a strong function of the diameter as well as the electronic DOS. An enhanced σ is expected in QDSL and SNW structures with reducing diameters. This is mainly because of the increased carrier relaxation times in such low dimensional structures[51].

2.3 Seebeck coefficient S

The Seebeck coefficient is the magnitude of the induced voltage divided by the temperature gradient across a material. The Seebeck effect is caused by charge-carrier diffusion and phonon drag. Many TE TMOs such as TiO_2, ZnO, CoO and MnO_2 exhibit large Seebeck coefficients. High S values in TMOs usually arises from either high effective masses (m^*) due to electronic correlations[52] or from electron–electron interactions[53]. An enhancement in the S of TMOs can be achieved by altering the DOS through nanostructuring techniques. The theory governing the S of bulk and low dimensional TE TMOs is presented in this section.

2.3.1 Bulk (3D) materials

For semiconducting TMOs in bulk form, the simplified Seebeck coefficient can be estimated by the following expression:[16]

17

$$S_{bulk} = \frac{8m^*\pi^2 k_B^2}{3eh^2} T \left(\frac{\pi}{3n}\right)^{2/3} \qquad (12)$$

where, n is the carrier concentration, m^* is the carrier effective mass, e is the electronic charge, T is the temperature, h is Planck's constant and k_B is the Boltzmann constant.

Eq.12 shows that a higher m^* results in larger Seebeck coefficients. TMOs usually exhibit high effective carrier masses, which explain the high S values observed in many TMOs. From Eq. 12 it is also predicted that in an increase in T also enhances S. Dramatically enhanced S has been observed in many TMOs such as ZnO and MnO_2 at elevated temperatures[5, 9] and will be discussed in their relevant sections.

2.3.2 2D materials

2D quantum well structures can result in enhanced S of TE TMOs materials due to changes in the Fermi energy of the carriers as well as the electronic DOS. For a 2D quantum well structure, the Seebeck coefficient is defined as:[20]

$$S_{2D} = -\frac{k_B}{e}\left(\frac{2F_1}{F_0} - \chi_{2D}^*\right) \qquad (13a)$$

$$\chi_{2D}^* = \frac{1}{k_B T}\left(E_F - \frac{\pi^2 k_B^2 T^2}{12E_F} - \frac{h^2\pi^2}{2m_z^* W^2}\right) \qquad (13b)$$

where, k_B is the Boltzmann constant, e is the electron charge, E_F is the Fermi energy, T is the temperature, m_z^* is the component of the effective mass, W is the quantum well width and F_i are Fermi-Dirac functions. χ^*_{2D} is the reduced chemical potential for quasi-2D structures.

The decrease in W of the quantum well is predicted to result in an enhanced S as can be seen from Eq. 13a & b. Additionally, the electron filtering (i.e. only high energy electrons can pass while others are scattered)[54] in such low-dimensional heterostructures is expected to decouple the S and σ, allowing fairly independent control over these properties. The

18

phenomenon of electron filtering is explained in more detail elsewhere[51, 55]. In 2D TMOs, an increase in S has been experimentally observed. Ohta *et al.* demonstrated dramatic increases in S (up to ~ 5 times) for 2D electron gas (2DEG) systems based on doped TiO_2 which will be discussed in detail in Section 4.1.3[56, 57]. 2D layered cobalt oxides and rhodium oxide also show higher S compared to their bulk forms[58, 59].

2.3.3 1D materials

TMOs are widely synthesised in various 1D morphologies[26, 60-62]. Size reduction to a single dimension is expected to enhance S due to the altered DOS. The S for a 1D structure is defined as:[23]

$$S_{1D} = -\frac{k_B}{e}\left(\frac{3F_{1/2}}{F_{-1/2}} - \eta\right)$$
(14)

where, F_i is the Fermi Dirac function, e is the electronic charge, k_B is the Boltzmann constant and $\eta = \zeta/k_B T$ is the reduced chemical potential, in which ζ is the chemical potential relative to the lowest bound state. In a 1D structure, S is influenced by the Fermi level of the carriers (Eq.14), which in turn is strongly influenced by the width of the 1D structure.(see ref.[23] for details). Hence, an enhancement of S is predicted with decreasing width of the 1D structure. S is also a function of the energy derivative of the electronic DOS[35]. As the dimensionality decreases, an increase in Seebeck coefficient is expected because of changes in the DOS due to quantum confinement[20, 21, 23, 63]. Due to the extensive information that is available about the crystal structures of TMOs, such morphological tuning of the DOS can be conveniently carried out. As predicted, the S in 1D TE TMO such as ZnO nanowires is shown to increase due to quantum confinement[49] and exhibits a value of ~ –450 μV/K at room temperature.

19

2.3.4 0D materials

QDSL and SNW structures as described in section 2.1.4 exhibit sharper DOS compared to higher dimensional structures, due to the superlattice-like structure along the wire axis (Fig. 2c). An electronic structure with sharp maxima in the DOS like this is predicted to be the best for TE materials[50, 64]. Due to their unique electronic band structure and sharp density of states, an enhancement of S is expected in QDSLs and SNWs[50].

The Seebeck coefficient of a segmented nanowire is defined as:[27, 28]

$$S_{0D} = -\frac{1}{eT}\left(\frac{K_{(1)}}{K_{(0)}}\right) \tag{15}$$

From Eq. 6 a, b and 15 it is obvious that a sharp maximum in the electronic DOS (Fig. 2d) will result in a strong increase in the Seebeck coefficient. As the diameter is decreased, the size quantisation effects prevail, resulting in an enhanced S. The increase of S in such 0D TMO structures is expected to be more pronounced. Even though metal oxide based SNWs have been synthesised[46, 65], there are no reports investigating their Seebeck coefficients. This presents a vast potential for future work in the field of TE TMOs.

From the discussion in this section, it is evident that reducing the dimensionality of TMOs offers opportunities to tune the key TE parameters of κ, σ and S independently. There has been a continuous development in the synthesis techniques of TMOs and there is a vast amount of information available about their crystal structure, phases and various morphologies. This allows flexibility in their fabrication which can be carried out at both large and small scales using liquid and gas phase deposition techniques, allowing tuning of their TE properties at low dimensions to engineer TMOs with high TPFs and figures of merit. A recent review article comprehensively discusses the latest developments in the synthesis of metal oxide nanostructures[66].
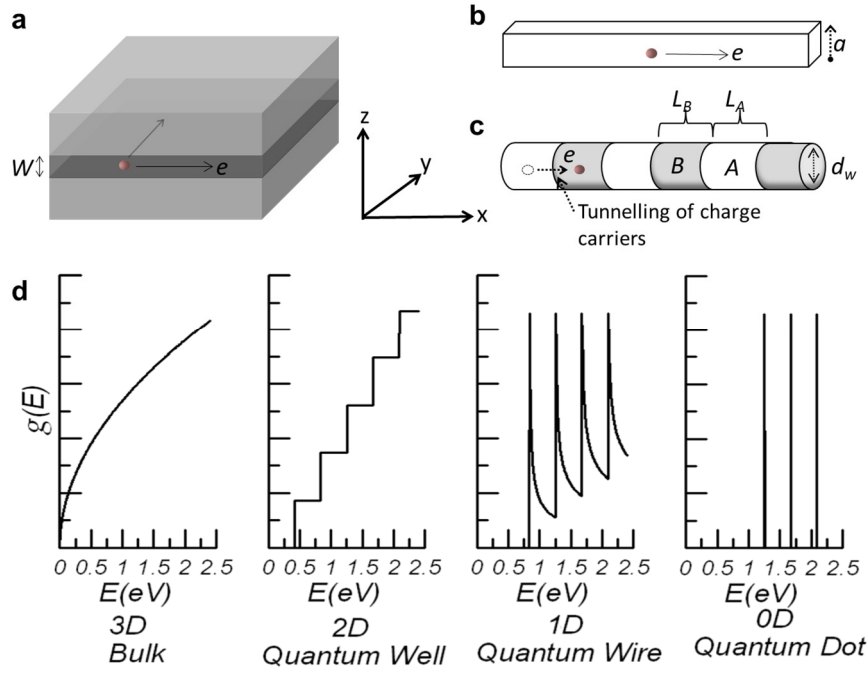
Fig. 2. (a) A 2D quantum well structure with width W, (b) 1D conductor (nanowire) with a square cross section of width a, (c) a segmented nanowire superlattice of diameter d_w comprising of quantum dots (0D) of alternating materials A and B, with respective segment lengths L_A and L_B. (d) Energy dependence of the electronic DOS in 3D, 2D, 1D and 0D materials. ((c), (d) Reproduced with permission from [28] and [29].)

3 Strategies to tune and alter TE parameters of TMOs

The TE performance of TMOs is assessed on the basis of the application. Applications of TE TMOs can be classified into four major categories: (1) cooling and refrigeration, (2) energy scavenging from heat, (3) sensors and (4) thermopower wave sources, all of which will be discussed in detail in section 5. For cooling, refrigeration, and energy scavenging, a high TPF along with a low κ is desirable[67, 68]. Sensors generally require high S and low κ, while σ can be either high or low depending on the type of sensor. Thermopower wave sources require a high TPF and benefit from a high κ [5-7, 69]. Hence, the tuning of the key TE parameters in TMOs depends on the application.

Furthermore, a fundamental understanding of the carrier transport processes contributing to the TE effect in TMOs is required. There are however, many complexities in determining the

21

key quantities in electron and phonon transport both theoretically and experimentally[70-72]. Tuning of transport properties of TE TMOs, such as reducing electronic thermal conductivity[73] or reducing the bipolar effect[74, 75], is possible. In their recent review papers, Minnich *et al.*[72] and Zebarjadi *et al.*[70] have extensively covered the challenges and strategies for improving our understanding of carrier transport processes.

In this section, the techniques that are commonly used to alter the TE parameters of TMOs are briefly discussed.

3.1 Optimization using stoichiometry and doping techniques

The incorporation of dopants and altering of stoichiometry are widely employed for adjusting the TE parameters of TMOs[76]. The type of application plays a crucial role in determining the correct technique in this regard[77]. For cooling, refrigeration, heat scavenging and sensing applications, methods that reduce κ_{phonon} are generally desirable. Crystal disorder in the unit cell can be created by doping or altering stoichiometry of the TMO crystal lattice[34]. Such manipulations change the vibrational properties of the crystal and influence κ_{phonon}[16] or by introducing additional scattering sites for phonons, thereby limiting κ_{phonon}[78-82]. $\kappa_{electron}$ is also affected by changing the stoichiometry and doping level of the TE TMOs. $\kappa_{electron}$ depends on the electrical conductivity of TMOs (Eq. 2b) and is also a function of the Fermi level and charge carrier concentration, which are directly affected by changes of stoichiometry or incorporation of dopants[17]. In many refrigeration and heat scavenging applications, high electrical conductivity is desired, which generally directly increases $\kappa_{electron}$. However, this is not desirable as it enhances the exchange of heat between two sides. Hence, doping, compositing and processes altering the oxygen deficiency can be implemented to achieve the desired thermal conductivity. Conversely, in thermopower wave sources, high TPF and κ are desirable. This can be achieved by the use of metallic dopants or reducing the TMOs to a degree that the Seebeck coefficient is not compromised. Such

22

dopants result in enhanced TPFs in TMOs such as ZnO and CoO_2, which will be discussed in details in sections 4.4 and 4.7 respectively[83-95] [96].

After incorporating dopants and altering the stoichiometry, the most challenging issue is the determination of electronic band structures[70]. Theoretical methods such as density functional theory (DFT) can help; however, underestimation of the band gap by DFT calculations generally results in inaccuracy of theoretical predictions of the Seebeck coefficient and the bipolar effect[70]. Many methods have been developed to address this issue, such as the dynamical mean-field theory (DMFT)[97] which has been successfully applied to the case of TMOs[98].

The calculation of electron mobility and carrier lifetime is even more challenging. First principles calculations can only be performed on limited supercell sizes and the inclusion of long range potentials is difficult[70]. More importantly, inelastic scattering mechanisms at the elevated operating temperatures of TE TMOs renders relaxation time approximations (RTA) calculated from first-principles and DFT mostly invalid[99, 100]. The details of carrier lifetime in many TE TMOs are still relatively unknown. Hence, an improved fundamental understanding of the mechanisms governing the formation, stability, and properties of interfaces is required[54].

3.2 Substructuring

In engineering TE TMOs, it is generally desirable to decouple κ_{phonon} and $\kappa_{electron}$. For many refrigeration and heat scavenging applications it is desired to adjust κ_{phonon} without affecting σ (hence $\kappa_{electron}$). Substructuring (or segmentation) approaches are suggested to be efficient for such manipulations. Substructuring relies on a periodic arrangement of layers with different electron and phonon transport characteristics, resulting in a complex material structure with distinct regions providing particular functionalities (Fig. 3). For many refrigeration and heat

23

scavenging applications, an ideal TE TMO would comprise a high mobility semiconductor region entwined with a phonon scattering region that houses disordered structures (dopants and lack of stoichiometry), without affecting the carrier mobilities of the other region[16]. A detailed discussion on the substructuring approach is provided in another review[16]. TMOs occurring as natural superlattices can provide an independent control of transport properties, providing an excellent platform to engineer high performance TE materials. TMOs such as the doped cobalt oxide systems are a classic example of the benefits of substructuring approach, which will be discussed in detail later[11]. Another advantage of TMOs is that they can be fabricated in a variety of well-studied structures and a large number of synthesis techniques to fabricate them in different morphologies and structures have been well-established, making the substructuring approach highly attractive in order to tune their TE parameters according to the desired application.
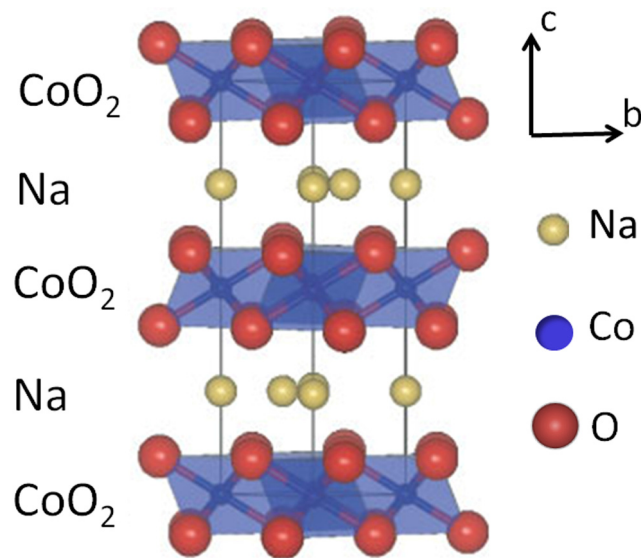

Fig. 3. Schematic depiction of the substructuring approach in doped cobalt oxide, comprising of ordered CoO_2 layers that are separated by disordered layers (of Na dopant) to achieve a good electrical conductivity and poor phonon conductivity. (Reproduced with permission from[42].)

3.3 Nanostructuring

As discussed earlier, the S, σ and κ for conventional 3D crystalline TMOs are interrelated and cannot be controlled independently. Any increase in σ results in an enhanced $\kappa_{electron}$ (Eq. 2b). Additionally, a change in the Fermi level and carrier concentration affects both $\kappa_{electron}$ and κ_{phonon}.

At the nanometer scale, there are significant changes to the electronics of TE TMOs (see section 2), which allow for alternative techniques to control the S, σ and κ in a relatively independent manner. In nanostructured materials, quantum confinement effects [51] and surface properties become much more important, and result in properties that are changed from those of the bulk forms. The quantum confinement of carriers in nanostructured TMOs is predicted to enhance both their TPF and ZT (see section 2.2 and 2.3) [63]. Additionally, it is well known that nanostructuring of TMOs alters their Fermi level and carrier concentration.[31] Nanostructures also introduce additional scattering mechanisms. If the spacing between the nanoparticles is larger than the electron mean free path (MFP), they will act as an additional source of electron scattering in the host material. If however, the spacing is smaller than the electron MFP, the scattering mechanisms will become much more complex since the leakage of the electron wave into the nanoparticles is no longer negligible.[70, 101] The nanostructuring technique has resulted in enhanced TPFs and ZTs in TMOs such as TiO_2, ZnO, cobalates and manganates which will be discussed in detail in Section 4[56] [91] [102, 103].

In addition to the electronics of TMOs, their phonon propagation properties and as a result κ_{phonon} can be tuned *via* nanostructuring (see section 2.1), resulting in enhanced phonon scattering and altered phonon mean free paths.[103] If the dimensions of semiconducting TE TMOs are smaller than the mean free path of the phonons, but larger than the mean free path of the charge carriers, a reduction in κ_{phonon} can be obtained due to boundary scatterings,

25

without affecting σ. Koumoto *et al.* have reviewed the progress in the development of nanostructured TE TMOs[22].

Nanostructuring can be implemented to decrease the lattice thermal conductivity by introducing many interfaces with spacing smaller than the phonon mean free path. Although reducing lattice thermal conductivity through alloying and/or nanostructuring techniques has been the most effective way to improve performance of TE TMOs for conventional applications, details of phonon transport mechanisms are still not very well understood[72]. Even in bulk form, theoretical and experimental determination of quantities such as phonon mean free path is still a challenge[72]. Phonon transport models based on Callaway model of thermal conductivity[104] usually require adjusting various fitting parameters causing inconsistency in the models fundamental predictions such as phonon's wavelength and mean free path. Calculations of the thermal conductivity and phonon mean free path in TE TMOs using combined density functional theory (DFT) [105, 106] and molecular dynamics (MD) [107-109] simulations on the other hand are difficult and computationally costly because of the extremely complex crystal structure of alloys and misfit layered oxides. Moreover, the introduction of many interfaces in the material *via* nanostructuring adds more complexity to the problem.

The problem is even more complex in case of electron transport. In case of heavily doped complex TE TMOs, the standard analysis based on the Boltzmann equation with the assumption that the mean free path is much larger than the de Broglie wavelength leads to inaccurate results[72, 110]. Nanostructuring further complicates the problem as the interfaces introduce complex scattering mechanisms that should be accounted for in theoretical analysis[111]. Therefore, modeling the transport phenomena in bulk and nanostructured TE TMOs would require more powerful tools such as the non-equilibrium Green's functions with the inclusion of electron wave effects[72].

3.4 Compositing

It is suggested that composites can be useful in controlling TE parameters of TMOs, as they can be designed to show high density of the interfaces[112], that can be used for adjusting both phonon and electron scattering. TMO composites' distinct advantages are their cost effectiveness and scalability[113]. An excellent review article discussing the impact of the bulk composite engineering approaches on S, σ and κ can be seen in ref. [72]. Composites of TMOs have resulted in enhanced TPFs, which will be discussed later in the relevant sections[91, 114].

4 Transition metal oxides and their TE properties

In this section, the most common TMOs that have been investigated for their TE properties will be discussed. An overview of their crystal structures and their TE properties in doped and various stoichiometry conditions will be presented. Additionally, different synthesis methods of these TE TMOs will be illustrated. For further information regarding the structures, properties and syntheses of TMOs, the readers can refer to comprehensive text books in this field[115-117].

4.1 Titanium oxides – TiO$_x$

4.1.1 Crystal structure

TiO$_2$ is one of the most investigated metal oxides for a wide variety of photocatalytic, TE, solar cell, biosensing and gas sensing applications. TiO$_2$ has a bandgap of ~3.2 eV in its intrinsic form[118]. The most common polymorphs of TiO$_2$ are anatase, rutile and brookite. Rutile and anatase exhibit a tetragonal structure, while brookite is orthorhombic[119]. The transformation with increasing temperature usually follows the sequence: anatase→ brookite→ rutile. Generally in between room temperature and 598 K anatase is the dominant polymorph. Above 625 K, the anatase transforms to brookite[120]. Heating of titania in the

temperature range of 873 to 1275 K leads to an alteration of phase stabilities, and it transforms almost completely to rutile. Many reviews on the various crystal structures, size and temperature dependence of the different polymorphs as well as different morphologies of stoichiometric and non-stoichiometric TiO_x exists[119-121].

4.1.2 TE properties of stoichiometric TiO_2

TiO_2 can be synthesised in many different morphologies such as spheroidal nanocrystallites, nanoparticles, nanotubes, nanosheets, nanofibers and epitaxial thin films[122]. The room temperature S of crystalline TiO_2 is reported to be approximately -600 μV/K, while σ of the order of 10^3 S/m is observed, resulting in a TPF of 360 μW/m.K^2. The κ at room temperature is ~ 5.8 W/m.K and is reduced with increasing temperature (~ 2.8 W/m.K at 1073 K) [123]. Owing to a moderate σ and high κ, the ZT in pure TiO_2 is low (< 0.025) [123, 124]. However, non-stoichiometric $TiO_{(2-x)}$ has been demonstrated to be promising for TE applications at both cryogenic [125] and elevated temperatures[124]. The TE properties of reduced, oxidized and doped TiO_2 are discussed next.

4.1.3 TE properties of non-stoichiometric, doped and composite TiO_x

Non-stoichiometric TiO_x can show fascinating TE properties both at elevated and cryogenic temperatures. Tsuyomoto *et al.* have shown that TiO_x (x=1.94) with an orthorhombic crystal structure, exhibits a peak S of -518 μV/K and σ of 2×10^3 S/m at $\sim$350 K. They demonstrated that both S and σ increase with temperature, resulting in a TPF of $\sim$540 μW/m.K^2 at 343 K[126]. Interestingly, single crystal rutile TiO_2 reduced to $TiO_{(2-x)}$ *via* annealing in H_2 at elevated temperatures as high as 1050 K shows exceptionally high TPFs at cryogenic temperatures. $TiO_{(2-x)}$ generates enlarged phonon scattering by the defect planes, resulting in low thermal conductivities (0.83 W/m.K). Fig. 4a & 4b depict that $TiO_{(2-x)}$ can exhibit an extraordinary S of up to $-60,000$ μV/K, with TPF and ZT of $\sim 1.7 \times 10^4$ μW/m.K^2 and 0.1, respectively, at temperatures in the range of 10 K[125]. Another study showed that non-

28

stoichiometric $TiO_{(2-x)}$ with a rutile crystalline structure, formed after annealing and reduction in a carbon environment at 1373 K, demonstrates a TPF of 100 $\mu W/m.K^2$ at temperatures of up to 550 K[124]. Obviously, the introduction of oxygen vacancies in the TiO_2 crystal result in enhanced σ due to an increase in carrier concentration (Eq. 8). In contrast, a prolonged oxidation of TiO_2 at elevated temperatures, results in lower σ and S (-600 to $+150$ $\mu V/K$) and therefore low TPFs and ZTs (<0.1). Additionally, a transition from n-type to p-type is also observed in the oxidation process, at temperatures around 1300 K[127].

In addition to the change of stoichiometry, the doping technique is usually employed to tune the TE properties in TiO_2. As discussed in section 3.1, metallic dopants are useful as they result in enhanced electrical conductivities. Additionally, the doping process creates crystal disorder, which reduces the lattice thermal conductivities. It has been shown that Na doped titanate nanotubes (DTNTs) with a composition such as $Na_{2-x}H_xTi_3O_7$ result in TPFs ranging between 174 - 280 $\mu W/m.K^2$, and a peak ZT of 0.3, at elevated temperatures (745-1032 K).[128] 2% Nb doped, anatase, n-type TiO_2 epitaxial films show a TPF and ZT of 250 $\mu W/m.K^2$ and 0.25, respectively, at 900 K[129]. Similar observations have also been made by Sheppard *et al.* at elevated temperatures[130, 131].
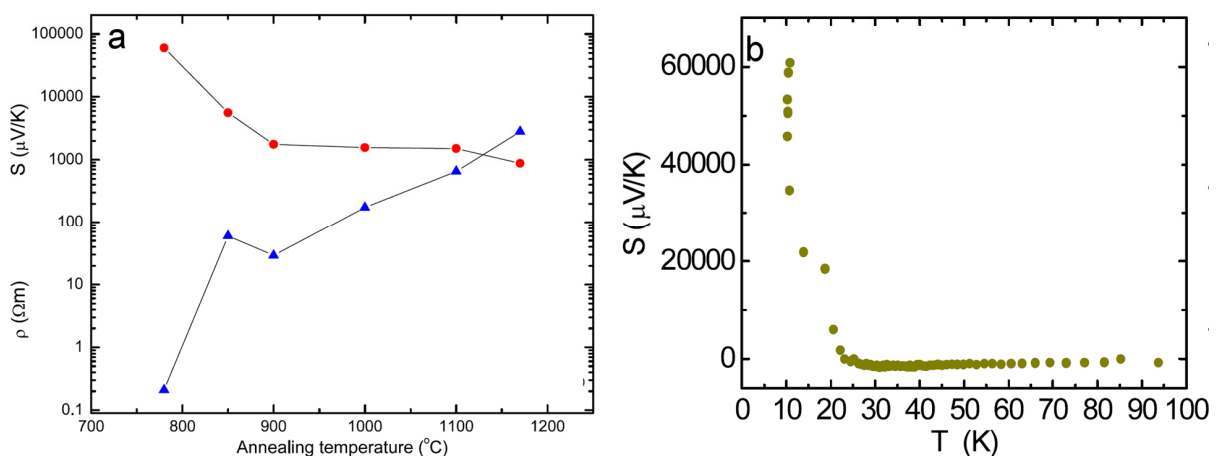

Fig. 4. (a) Seebeck coefficient (red) and electrical resistivity (blue) of reduced single crystal rutile TiO_x as a function of annealing temperature and (b) Seebeck coefficient as a function of temperature for a sample annealed in H_2 at 1053 K. (Reproduced with permission from [125].)

29

A TiO$_2$ composite commonly investigated for its excellent TE properties is strontium titanate (SrTiO$_3$), also known as STO[1, 57, 132]. STO is a perovskite type oxide that exists in an isotropic cubic crystal structure at temperatures above 100 K. Additionally, it shows a strong structural tolerance to substitutional doping. Due to its *d*-band nature, the effective mass of carriers is quite large in STO, resulting in a high S (Eq.12). Additionally, STO exhibits a very high melting point (~2350 K), suggesting its stability at high temperatures[22].

In its pure form, STO is essentially an insulator; however, it can be tuned to be semiconducting or metallic by substitutional doping with La^{3+} or Nb^{5+}[57]. The highest TPF and ZT for La and Nb doped STO single crystal has been reported to be 3600 μW/m.K^2 and 0.1, respectively at room temperature, while the corresponding values at 1000 K, are 865 μW/m.K^2 and 0.27, respectively (Fig. 5a-e) [133] [1, 132] [134]. A number of studies on the TE properties of La and Nb doped STO thin films exist[129] [134] [135]. The ZT values are limited primarily due to its high κ (~11.0-3.2 W/m.K in the temperatures of 300-1000 K respectively) [22]. This high κ value can be ascribed to the perovskite type structure of STO, which even in the presence of dopant cations as point defects, lacks effective phonon scattering centers.

Muta *et al.* suggested that a Ca^{2+} substitution at Sr^{2+} sites may result in reduced κ, as it is established that such substitutions result in the introduction of defects that usually lower κ[136]. However, Yamamoto *et al.* have reported that such an approach results in a dramatic reduction of the TPF, which indicates that any further improvement in ZT is almost impossible to achieve in a conventional 3D bulk state of STO[137].

A reduction in the STO dimensionality is a strategy that is predicted to enhance TE properties by offering independent control of the key TE parameters (section 2). The fabrication of a two-dimensional electron gas (2DEG) can be useful as it results in a 2D quantum

confinement of carriers. Ohta *et al.* utilized a high density 2DEG, which is confined within a layer of STO that has a thickness of a unit cell (0.3905 nm) [56]. Such 2DEG is realized in $SrTiO_3/SrTi_{0.8}Nb_{0.2}O_3$ superlattices and $TiO_2/SrTiO_3$ heterointerfaces. It was shown that in an optimised state, a 2DEG exhibits a massive TPF of 1.0×10^5 µW/m.K^2. The resultant ZT at room temperature was approximately 2.4 even if a κ value of a bulk single crystal STO is used (12 W/m.K). A recently published review article discusses new developments in STO based thermoelectrics in detail[78].
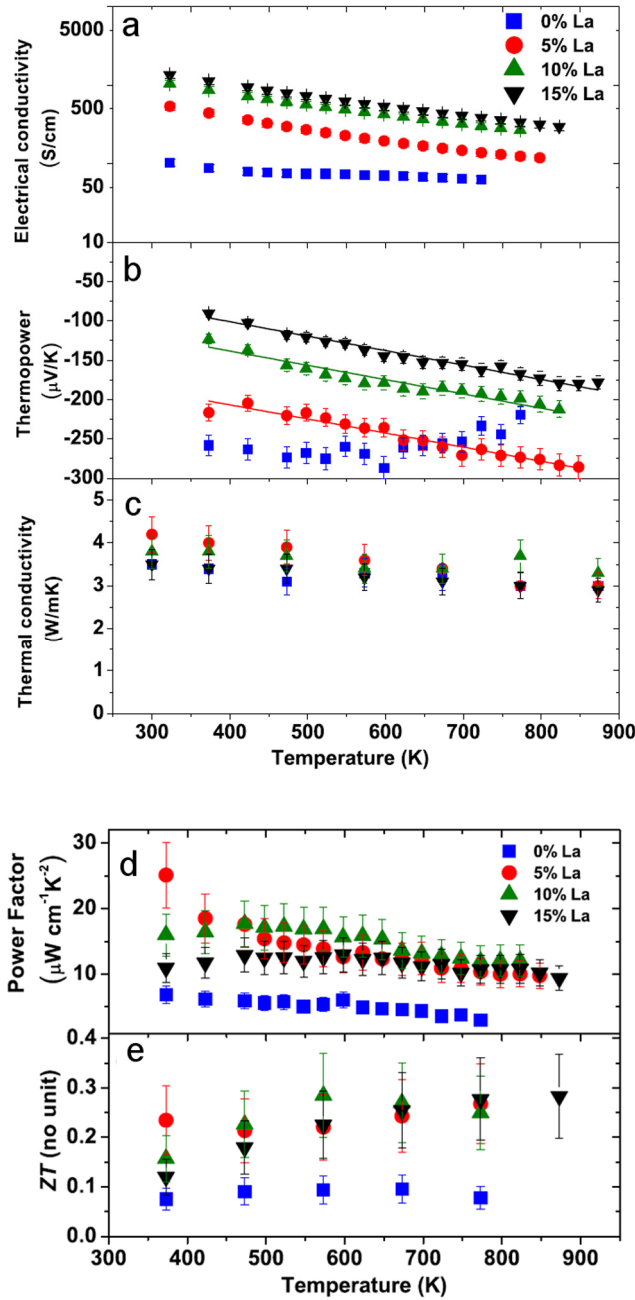
Fig. 5. (a) Electrical conductivity, (b) Seebeck coefficient, (c) thermal conductivity, (d) TPF and (e) ZT *vs* temperature for different concentrations of La dopant in STO thin films. (Reproduced with permission from [134].)

4.1.4 Methods of synthesis

Many different vapour chemical based methods have been used for forming TE TiO_2 materials. Chemical synthesis which involves sol gel hydrolysis, electrochemical methods such as anodization of Ti and hydrothermal synthesis have been commonly used for

producing doped or non-stoichiometric TiO₂, as the concentration of dopants and metal/oxygen ratios can be readily controlled in such methods[122],[138] [128].

Vapour deposition techniques including sputtering and pulsed laser deposition (PLD) have also been commonly used for forming highly crystalline TiO₂ with predetermined concentrations of dopants[129]. STO thin films doped with both La and oxygen vacancies have been shown to be synthesized using the PLD technique[134] [139]. PLD can also be used in forming 2DEG STO crystals comprised of superlattices of insulating/ Nb-doped layers of STO to achieve very high TPF of 1.0×10^5 μW/m.K^2[56, 57].

4.2 Manganese oxides – MnO$_x$

4.2.1 Crystal structure

MnO₂, the most common form of manganese oxide, is a small bandgap (~ 1.3 eV), n-type semiconductor and is widely used for electrodes in supercapacitors, electrochemical batteries and microbial fuel cells[140] and as a catalytic material[141]. It exists in a number of structural forms[142, 143]. The most common polymorphs are the α-MnO₂ (psilomelane - monoclinic structure) and β-MnO₂ (pyrolusite - rutile structure) [140]. Other forms known as δ-, γ- and λ-MnO₂ also exist, and differ in the way in which the MnO₆ octahedra are linked[138, 144, 145]. A detailed study of various crystal phases of MnO₂ is presented elsewhere[143].

4.2.2 TE properties of stoichiometric MnO₂

β-MnO₂ has been reported to be promising for TE applications at elevated temperatures[9, 142]. Although, the semiconducting properties of α-, β- and γ-MnO₂ have been studied in detail,[146] their TE properties have not been widely investigated, and only a limited number of studies exist. It has been reported that bulk and thin film β-MnO₂ exhibit S of

33

approximately -300 µV/K and σ of 10^3 S/m, resulting in a TPF of 90 µW/m.K^2[147]. Recently, Song *et al.* reported extremely high Seebeck coefficients in β-MnO$_2$ nanopowder[142]. The S and σ of the MnO$_2$ thin films have been shown to increase dramatically with temperature[9]. A Seebeck coefficient of approximately -1900 µV/K at a temperature of 623 K has been demonstrated. The σ of the thin films at such elevated temperatures is $\sim 10^3$ S/m, resulting in a TPF of 3600 µW/m.K^2. The κ for MnO$_2$ is reported to be approximately 4 W/m.K[9].

Although the TPF of MnO$_2$ is high, its ZT is still low. As suggested in section 3.3, nanostructuring can be used to tune the TE properties of a material. MnO$_2$ nanostructures such as nanorods and nanowires have been synthesized *via* various methods [9, 142].

4.2.3 TE properties of non-stoichiometric, doped and composite MnO$_x$

Doping and compositing are good strategies that can be used for increasing TE performance of MnO$_x$ by introducing defects in the crystal structure, thereby impeding the lattice thermal conduction. Polycrystalline, bi-layered LaSr$_2$Mn$_{2-x}$Co$_x$O$_7$ ($x<0.2$) has been reported to exhibit extremely low TPFs[148]. However, the most commonly reported manganate stoichiometry for TE applications is the perovskite type CaMnO$_3$. It exhibits an orthorhombic symmetry in which each Mn atom is surrounded by six Mn neighbours. It occurs in two anti-ferromagnetic crystal phases: the A-type and G-type, out of which the G-type phase is more stable. The G-type phase exhibits an indirect bandgap of 0.7 eV, which accounts for its perfect semiconducting behaviour[149]. The mixed valent, perovskite electron doped manganite CaMnO$_3$ has been shown to be a promising n-type TE material, especially at high temperatures[79]. This perovskite system exhibits S of -350 µV/K and σ of 50 S/m, resulting in a TPF of 6.1 µW/m.K^2, which is very low for TE applications. However, the electrical conductivity of such an oxide can be enhanced by introducing suitable dopants[22]. The manganate may be doped on either site. The most commonly used dopant is ytterbium (Y) on

34

the calcium site and niobium (Nb) on the manganese site. The Y doping is particularly beneficial as it results in a lower κ and has been shown to be the most effective dopant[78-81].

A peak TPF of 300 μW/m.K^2 has been reported in CaMn$_{0.96}$Nb$_{0.4}$O$_3$ at 1000 K. The highest reported value of ZT is 0.2 at 1000 K for the stoichiometry Ca$_{1-x}$R$_x$MnO$_3$, which is much less than the desired value of at least 1, to make it practically applicable in TE modules[150]. Unfortunately, it has been predicted, using the dynamical mean field theory, that ZT>1 in electron doped CaMnO$_3$ is rather unlikely to be achieved[79].

Koumoto *et al.* used a nanostructuring approach in an effort to enhance the TE performance as predicted in section 3.3[22]. They showed that Ca$_{0.9}$Yb$_{0.1}$MnO$_3$ nanoparticles synthesised using gas phase reaction (GPR) show a higher TPF and ZT compared to those synthesised using solid state reaction (SSR) or liquid phase reaction (LPR). This is because GPR generally results in smaller and impurity-free particles due to the nature of the reaction medium. The difference in the TE properties of the GPR and SSR synthesised nanoparticles over a temperature range of 300 to 1100 K is shown in Fig. 6a-c. The highest value of the TPF was 190 μW/m.K^2 at 973 K, for the GPR synthesised nanoparticles, mainly due to lower electrical resistivity. The change of ZT with temperature for the GPR and SSR synthesised nanoparticles is shown in Fig. 6d. The maximum ZT value was 0.13 at 1073 K for particles synthesised using the GPR, which was approximately 1.5 times higher compared to the one's synthesised using SSR at the same temperature[22]. In this case, there was no significant enhancement in the TPF and ZT after nanostructuring.
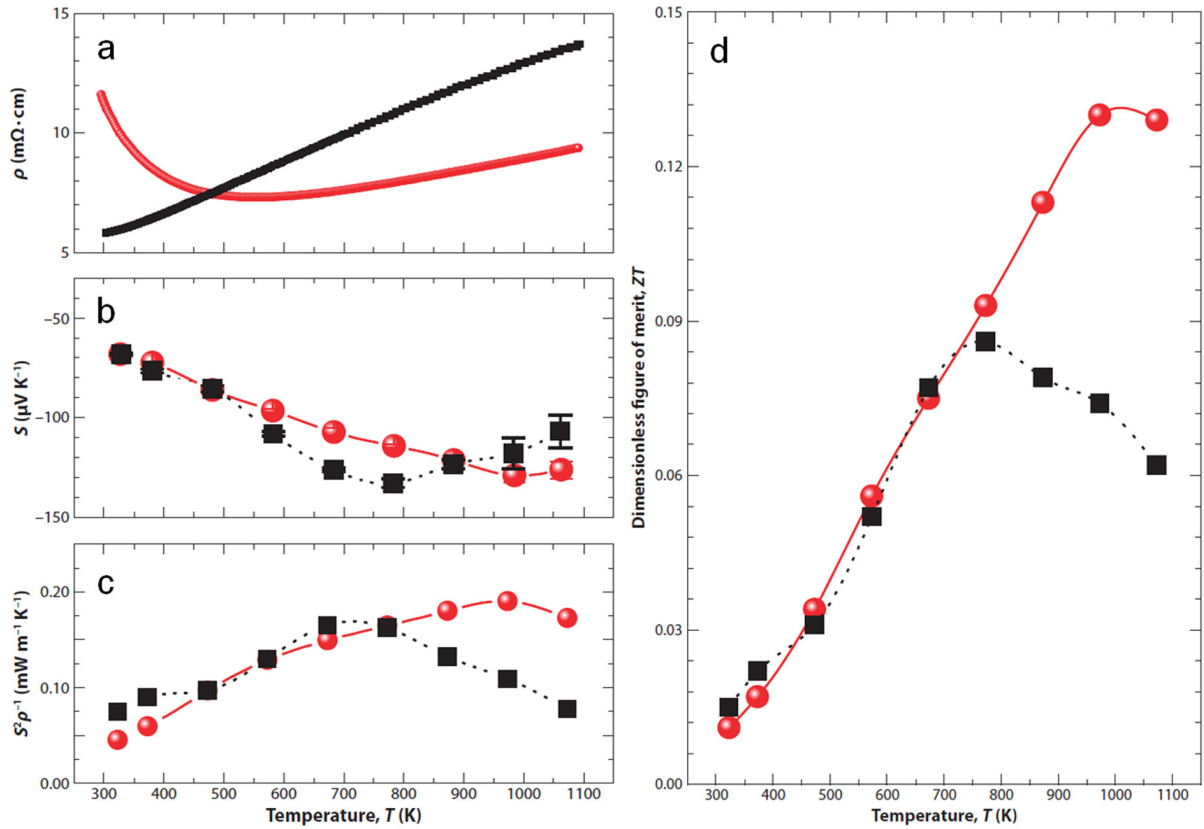
Fig. 6. (a) Resistivity, (b) Seebeck coefficient, (c) TPF and (d) ZT of GPR (red) and SSR synthesised (black) Yb-doped $CaMnO_3$ nanoparticles (Reproduced from [22].)

4.2.4 Methods of synthesis

Similar to other metal oxides, various liquid and gas phase synthesis techniques have been used for forming MnO_2. Electrochemical techniques such as anodization and electrodeposition are some of the commonly used liquid phase methods[151-154]. Chemical techniques such as the sol-gel and hydrothermal are also used to prepare crystalline α and β-MnO_2[155-157]. Vapour phase techniques such as PLD, atomic layer deposition (ALD) and molecular beam epitaxy (MBE) have also been used to synthesise MnO_2 thin films[158-160].

4.3 Tungsten oxides – WO$_x$

4.3.1 Crystal structure

Tungsten oxides (WO$_x$) are widely studied for sensing, chromic and photocatalytic properties[60] and WO$_3$ is the most commonly investigated stoichiometry of WO$_x$. WO$_3$ is an n-type TMO with a perovskite-like structure. It is well known for its various properties in a non-stoichiometric form, as its lattice can support a significant concentration of oxygen vacancies[60, 161]. Crystals of WO$_3$ are formed by the corner and edge sharing of WO$_6$ octahedra. Such corner sharing results in the following crystal phases: monoclinic I (γ), monoclinic II (ε), triclinic (δ), orthorhombic (β), tetragonal (α) and cubic (although cubic is not a commonly observed phase) [60]. Under different temperature conditions, bulk WO$_3$ follows the following sequence: monoclinic II (ε-WO$_3$, < 230 K) → triclinic (δ-WO$_3$, 230 to 290 K) → monoclinic I (γ-WO$_3$, 290 K to 603 K) → orthorhombic (β-WO$_3$, 603 K to 1013 K) → tetragonal (α-WO$_3$, > 1013 K) [162, 163]. At room temperature, γ-WO$_3$ is the most stable crystal phase[60]. The bandgap of WO$_3$ ranges between 2.6-3.25 eV depending on the crystal phase and size[60]. Tungsten oxide, which is synthesised or manipulated in liquid media, is very commonly found in hydrated form (yH$_2$O.WO$_3$).

4.3.2 TE properties of stoichiometric WO$_3$

There are only a few studies that have examined the TE properties of stoichiometric WO$_3$ and WO$_3$ hydrates[164, 165]. WO$_3$ exhibits σ ranging between 10–10^{-2} S/m depending on the stoichiometry[166]. Additionally, σ is also influenced by the grain size, film thickness and dopants. Hence, the electrical properties are strongly dependent on the synthesis techniques and conditions[167]. It has been shown that the S of WO$_3$ hydrates is highly temperature dependent and generally increases linearly with temperatures between sub-zero to 323 K. Beyond 373 K, S decreases exponentially and it also gradually loses the water content at

higher temperatures. A peak S with an absolute value of 480 µV/K is observed at 363 K[164]. Due to a low σ, the TPF is poor.

Hutchins *et al.* investigated the TE properties of α-WO$_3$ films of different thicknesses (100-500 nm) [168]. The S of the n-type WO$_3$ thin films varies with temperature (Fig. 7a), with the magnitude decreasing with increasing the film thickness, attaining a maximum absolute value of ~ 780 µV/K at a temperature of 350 K. Fig. 7b shows that σ of a 100 nm thick α-WO$_3$ film increases exponentially with temperature. The peak TPF of the α-WO$_3$ films was reported to be of the order of 1 µW/m.K^2[168]. Additionally, Patil *et al.* demonstrated S of 600 µV/K in stoichiometric WO$_3$ films at a temperature of 473 K[165]. The κ of stoichiometric WO$_3$ thin films is 1.63 W/m.K[169]. Undoped WO$_3$ films thus exhibit a maximum TPF of ~ 4 µW/m.K^2, which is rather too low to be considered for many TE applications except possibly in sensors for measuring temperatures.

4.3.3 TE properties of non-stoichiometric and doped WO$_x$

Non-stoichiometric tungsten oxides have not shown any improvement in TE performance compared to the stoichiometric counterparts owing to the poor σ[170]. However, using other TMOs for doping WO$_3$ appears to be an effective approach to manipulate its TE properties. Recently, the TE properties of ZnO doped WO$_3$ ceramics were investigated[161]. The introduction of ZnO was shown to result in an increased σ, by approximately two orders of magnitude, while causing only a slight drop in S. A ZnO doping concentration of 0.5 % was found to be optimal, resulting in a maximum TPF of 1.34 µW/m.K^2 at 973 K, which is similar to the values reported in stoichiometric WO$_3$ and at least four orders of magnitude higher than that of non-stoichiometric WO$_3$[171]. The variation of TPF with temperature for different levels of ZnO doping is shown in Fig. 7c. Aluminium oxide (Al$_2$O$_3$) doping has also been shown to enhance σ of WO$_3$ by a factor of 10^4[166]. Elevated σ was also observed by adding Co$_3$O$_4$, MnO$_2$, LiO$_2$ and TiO$_2$ dopants[172].

38

To make WO$_3$ a viable TE TMO, nanostructured WO$_3$ needs to be investigated for its TE properties. Although, WO$_3$ nanostructures are widely synthesised and reported for other applications, a detailed investigation of their TE properties has not been carried out.

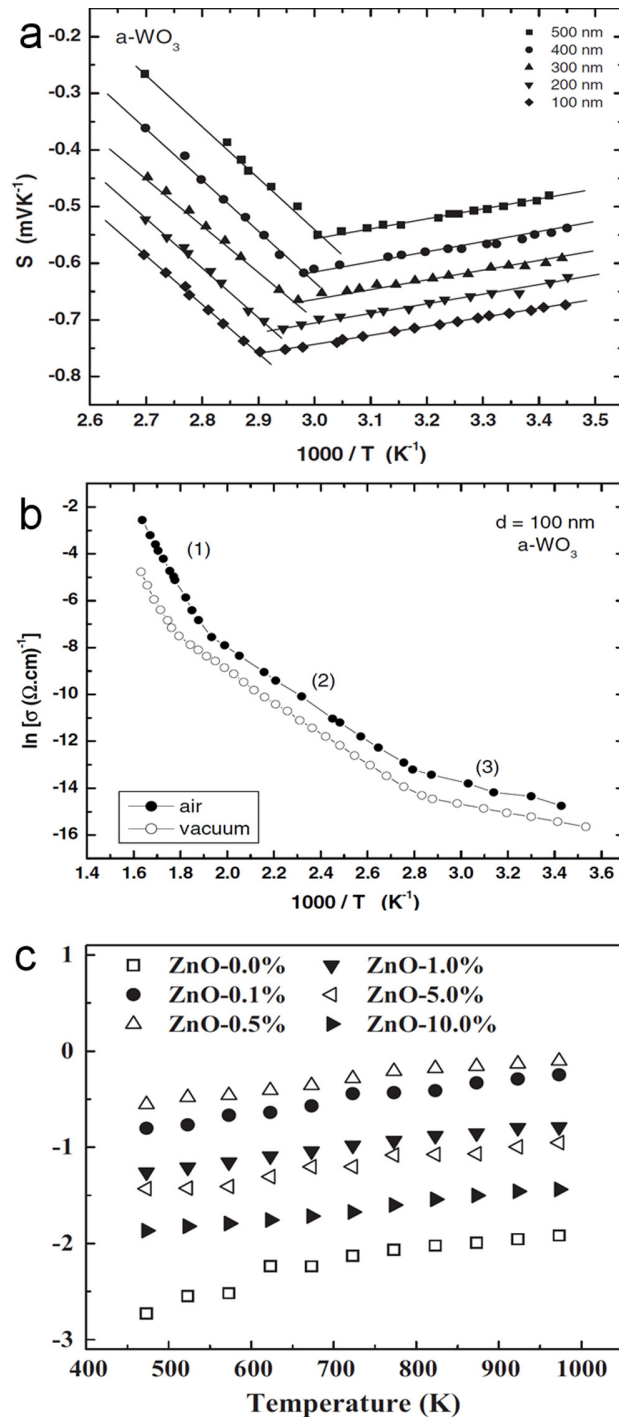**Fig. 7.** (a) Seebeck coefficient, (b) electrical conductivity variation with temperature for *α*-WO$_3$ films and (c) TPF obtained for varying ZnO doping concentrations in WO$_3$ ceramics. (Reproduced with permission from (a), (b) [168] and (c) [161].)

39

4.3.4 Methods of synthesis

Many liquid and vapour phase synthesis methods have been used to synthesise WO_3. Due to a high dependence of σ on the stoichiometry, the parameters of synthesis techniques play important roles in determining the TE properties of WO_3. The commonly used liquid phase techniques to synthesise crystalline WO_3 are sol-gel, hydrothermal synthesis and electrochemical techniques such as anodization and electrodeposition[173-175] [60, 176, 177]. The most common vapour phase techniques include RF sputtering, PLD, electron beam evaporation and thermal evaporation[60, 178, 179]. A detailed review of synthesis techniques for various WO_3 is presented elsewhere[60].

4.4 Zinc oxides – ZnO

4.4.1 Crystal structure

ZnO is the most widely investigated TMO for a wide variety of photovoltaic, sensing, optoelectronic, piezoelectric and TE applications[43, 180-183]. ZnO is a direct bandgap binary n-type semiconductor with a bandgap of 3.3 eV at room temperature and substantial ionic character residing at the borderline between a covalent and an ionic semiconductor[184]. It can show either a hexagonal wurtzite, cubic zinc-blende (which are both tetrahedral) or rarely rocksalt structure (which is formed at very high pressures) [43] [184]. In wurtzite structure, every Zn atom is surrounded by four oxygen atoms. In zinc-blende structure, each oxygen atom is surrounded by four Zn atoms in a similar fashion. At ambient temperatures and pressure wurtzite is the stable polymorph and a stable zinc-blende structure is generally obtained when ZnO is grown on cubic substrates[184].

4.4.2 TE properties of stoichiometric ZnO

ZnO is considered as a promising high temperature TE material and can be synthesised in a variety of morphologies such as poly- and single crystal ceramics, epitaxial thin films, nanorods, nanobelts, nanorings, hierarchical nanostructures[43].

At ambient temperatures, pure ZnO shows a TPF of ~800 μW/m.K^2. However, it also exhibits a high κ (~40 W/m.K). The κ of ZnO reduces at higher temperatures (~5 W/m.K at 1000 K). This has been attributed to increased phonon scattering possibly as a result of large and substantially anisotropic thermal expansion of ZnO[185]. Another study showed that sputtered ZnO thin films can exhibit TPFs as high as 1.0×10^3 μW/m.K^2[5].

Although it is possible to reach low κ's of 2-3 W/m.K at room temperature for nanograined ZnO ceramics[186], these structures exhibit highly reduced σ and therefore, neither TPF or ZTs improves. It has been postulated that the defects at grain boundaries are the major contributor to the drop in σ[186]. Overall, samples with larger grain sizes have been shown to exhibit higher σ.

As expected, nanostructuring approaches for bulk doped and undoped ZnO have also been shown to reduce κ[91, 186]. A large number of studies on TE properties of pure and doped ZnO have been conducted on polycrystalline ceramics[84-86, 88-90, 92, 93, 187-198]. TE properties of ZnO thin films[199-201] as well as nanostructures [87, 91, 94, 202, 203] have also been targeted in a number of studies. Commonly, nanostructuring results in a significant increase in S. As temperature increases, both S and σ are enhanced, resulting in higher TPFs and ZTs.

Of more interest however, are the TE properties of doped and co-doped ZnO, where the TPF and ZT can reach values as high as 1500 μW/m.K^2 and 0.65 respectively, making ZnO a viable candidate for a variety of TE applications.

4.4.3 TE properties of non-stoichiometric and doped ZnO

For heat scavenging applications, ZnO is commonly doped by n-type dopants such as Al, Ge, Ni and Ti to achieve improved TE properties. Al is the most common dopant for ZnO [83-94]. Generally, Al doping increases the carrier mobility and reduces the phonon mean free path in the crystal lattice of ZnO, resulting in higher σ and lower κ. ZT has been shown to increase to as high as 0.30 at 1273 K for Al concentrations of ~0.02 and a high TPF of 1500 µW/m.K^2 has been achieved at such elevated temperatures [83] Beneficial effects of Al doping can also be described in terms of its contribution to the high c-axis compression of the ZnO lattice leading to the increase in effective mass (m^*), resulting in enhanced S (Eq. 12) [89].

The dependence of TE properties of Al-doped ZnO (AZO), on the grain structure and secondary phases is further highlighted in a study by Jood $et\ al$[91]. Bulk pellets, obtained by cold-pressing and sintering the nanocrystals that comprise of ZnO nanograins with ZnAl$_2$O$_4$ nanoprecipitates, were shown to reduce κ to very low values (1.5 W/m.K at 300 K). These nanocomposites also showed high σ and S, resulting in a significantly high TPF and ZT of 900 µW/m.K^2 and 0.44 respectively, at 1000 K.

There are also reports of co-doping ZnO with Al and other n-type dopants. Co-doping of Fe, Ni and Sm metals with AZO has not shown significant improvement in TE properties, with the highest TPF and ZT of 675 µW/m.K^2 and 0.126 respectively, for Ni-co-doped AZO at 1073 K[93]. On the other hand, co-doping of AZO with Ga resulted in significant improvement in ZT. Ga co-doping seemed to increase the solubility of Al in ZnO and strongly reduce the κ value at 2 mol% of Ga. Also, much larger TPFs than those of AZO have been observed in co-doped samples (Fig. 8). The ZT value Zn$_{0.96}$Al$_{0.02}$Ga$_{0.02}$O reached a maximum of 0.47 at 1000K and 0.65 at 1247 K, a significant enhancement over conventional AZO[88].

A study on co-doped $Zn_{0.97}Al_{0.03-y}Ti_yO$ has shown an enhancement in both σ and S, resulting in TPFs as high as 3.8×10^2 µW/m.K^2 for $Zn_{0.97}Al_{0.02}Ti_{0.01}O$ at 1073 K.[86] κ and ZT values of these samples have however not been reported. Ga doping has also been reported to improve TE properties of ZnO resulting in ZT values close to the best Al-doped ZnO ceramics[198].
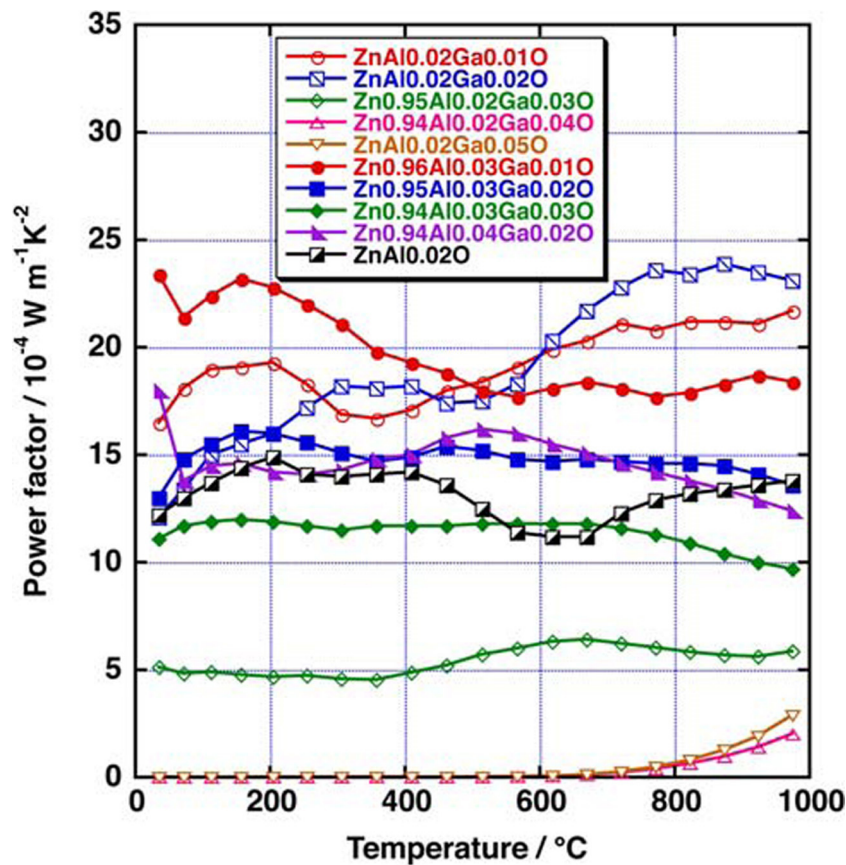
Fig. 8. Temperature dependence of TPF of $Zn_{1-x-y}Al_xGa_yO$ ceramics. (Reproduced with permission from [88].)

4.4.4 Methods of synthesis

ZnO is widely synthesised using various liquid and vapour phase fabrication techniques. It can be synthesised in many different morphologies such as nanowires, nanospikes, nanopillars, nanorods and nanobelts. Over the years, liquid phase fabrication techniques such as hydrolysis, spray pyrolysis, sol-gel and hydrothermal synthesis have been employed to

43

prepare ZnO for various applications[204-206] [207]. Other liquid phase methods to synthesise highly crystalline ZnO nanostructures include electrochemical techniques such as anodization and electrodeposition[208, 209].

Vapour deposition techniques such as RF/DC sputtering, ALD and MBE as well as chemical vapour deposition (CVD) technique and metal organic chemical vapour deposition (MOCVD) have been used to synthesise pure as well as doped ZnO thin films[210-213]. Other techniques such as spark plasma sintering (SPS) and PLD have also been widely used to synthesise densified ZnO in a powdered form[170][214, 215].

4.5 Copper oxides – Cu_2O and CuO

4.5.1 Crystal structure

Copper oxide occurs in two common phases: cuprous oxide (Cu_2O) and cupric oxide (CuO). Cu_2O (copper(I) oxide) has been commonly used for application in solar cells, catalysts, and sensors[216]. It exhibits a cubic crystal structure with a forbidden direct bandgap of ~1.9-2.2 eV, making it very challenging to study quantum confinement effects or modify its properties[217, 218]. Cu_2O has also been shown to depart from stoichiometry towards excess oxygen, leading to a p-type semiconducting nature and has been one of the most studied materials in semiconducting physics[219]. On the other hand, CuO (copper(II) oxide) belongs to the monoclinic crystal system with a direct bandgap of 1.2-1.5 eV and has been studied for photoconductive applications and is also the basis for several high temperature superconductors[217, 220]. In CuO, each Cu atom is coordinated by 4 oxygen atoms in an approximately square planar configuration. In a pure state and good stoichiometry, CuO behaves almost like an electrical insulator. However, non-stoichiometry leads to important semiconducting characteristics[221].

4.5.2 TE properties of stoichiometric copper oxides

A limited number of studies have been carried out on the TE properties of copper oxides in the 1990s. Jeong *et al.* examined the S and σ in uniaxially pressed CuO powder, which was subsequently sintered at different temperatures[222]. The CuO sample sintered at 1273 K in air, showed a peak S of ~650 µV/K between 400 to 500 K. Beyond 500 K, the S dropped rapidly. The corresponding σ as seen from Fig. 9a was approximately 1 S/m, resulting in a TPF of 0.42 µW/m.K^2[222].

It has been shown that single crystal Cu_2O exhibits a high S at elevated temperatures (~1050 µV/K at 923 K) [219]. On the other hand, the S of CuO thin films has been shown to change with varying film thicknesses (340 nm to 620 nm) and exhibits a maximum value of ~ 500 µV/K for ~600 nm thick films (Fig. 9b) [221]. However, none of these works reported electrical or thermal conductivities. The full TE properties of intrinsic copper oxides are yet to be investigated.

4.5.3 TE properties of non-stoichiometric, doped and composite copper oxides

The doping technique has been shown to result in significant effect on the TE properties of copper oxides. Koffyberg *et al.* have demonstrated the TE effect in polycrystalline samples of Li doped CuO[223]. They have shown an average p-type S of 770 µV/K and σ of 6.25 S/m, resulting in a TPF of 3.7 µW/m.K^2[223].

It seems that the most commonly investigated copper oxide composite for its TE properties is La_2CuO_4. It exhibits a simple layered structure comprising of 2D CuO_2 planes in a unit cell and is the parent compound for high temperature superconductivity, which is related to the excess oxygen content and the structural change as a result of phase transition[224]. This layered structure makes the anisotropy of conduction very strong. Due to the anisotropic

nature of their electrical conduction, such composites are potential TE materials. A detailed overview of its crystal phases is provided elsewhere[225].

For enhancing the TE properties of La_2CuO_4 metallic dopants can be incorporated. In this regard, TE properties of $La_{2-x}R_xCuO_4$ polycrystalline ceramics, where R can be Pr, Y or Nb have been investigated[226]. In this study, it has been shown that the choice of dopants plays a crucial role in determining the TE properties. Fig. 9c shows the variation of the TPF of $La_{2-x}R_xCuO_4$ with temperature for different dopants. As can be seen, with increasing temperature the TPFs of all composites decrease, eventually becoming stable above 700 K[226]. Samples show S ranging between 200 to 620 μV/K. Amongst them $La_{1.98}Y_{0.02}CuO_4$ ceramics exhibit a high TPF of 10^3 μW/m.K^2. The maximum ZT was reported to be 0.17 at 330 K, which is around 3 times higher than pure La_2CuO_4[226].

Studies on TE properties of n-type RE_2CuO_4 oxides, where RE is a rare earth element such as neodymium, samarium or gadolinium, have shown TPFs and ZTs of the order of 10 μW/m.K^2 and 0.005, respectively, at 950 K[227]. The electrical resistivities of such composites show a negative temperature dependence and is at least a magnitude higher than many conventional TE materials. Such RE_2CuO_4 type oxides exhibit a high κ of ~30 W/m.K at 300 K, which drops to ~ 8 W/m.K at 950 K [227], and can potentially be suitable for thermopower wave applications.
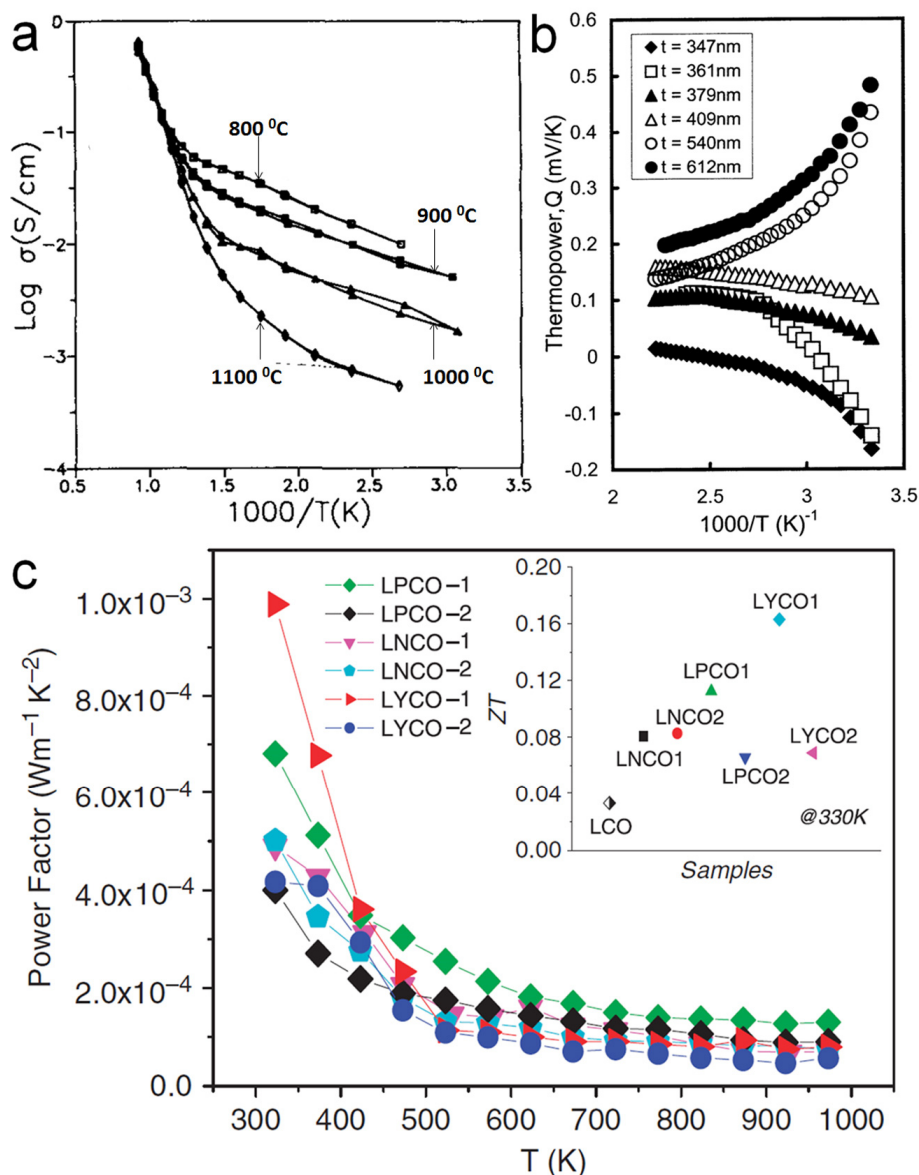
46

Fig. 9. (a) Electrical conductivity variation of CuO sintered at different temperatures, (b) Seebeck coefficient variation with temperature for CuO films of different thicknesses and (c) Temperature dependence of TPF for various La_2CuO_4 ceramics, (inset shows ZT values at 330 K) [LNCO (Nb doped La_2CuO_4), LPCO (Pr doped La_2CuO_4), LYCO (Y doped La_2CuO_4)]. (Reproduced with permission from (a) [222], (b)[226] and (c) [221].)

4.5.4 Methods of synthesis

Many liquid and vapour phase methods are used for synthesising Cu_2O and CuO. Liquid phase techniques of for the sol-gel[228], hydrothermal[229] and spray pyrolysis[230] have been used for the synthesis of copper oxides. Other liquid phase techniques commonly employed to prepare high purity copper oxides include electrochemical methods such as anodization and electrodeposition[231, 232]. The chemical synthesis methods, especially

hydrothermal are much desired for many applications as they are low cost, offer morphology control and facilitate low temperature synthesis and are therefore viable for large scale production[229]. Additionally, they result in a departure from stoichiometry when it is needed due to the introduction of point defects and impurities in the crystal lattice. Vapour phase techniques such as RF sputtering, PLD, various evaporation approaches and MBE have been demonstrated to synthesise crystalline copper oxide thin films at different oxygen contents[220]. Additionally, the CVD technique has also been utilized to synthesise copper oxides[233].

In most copper oxide synthesis methods a mixture of phases like Cu, Cu_2O and CuO is obtained. Post-deposition annealing or deposition at high temperature is usually needed to achieve the desired phase.

4.6 Vanadium oxides

4.6.1 Crystal structure

Vanadium oxide exists in many phases that include VO, VO_2, V_2O_3 or V_2O_5. However, only V_2O_5 demonstrates TE properties and shows highly anisotropic n-type electrical conduction[234]. It has a direct bandgap of ~2.4 eV and is a promising electrode material for energy storage systems such as Li-ion batteries[235-238] and possesses a high ionic storage capacity because of its layered structure[239]. Over the years, it has also been intensely investigated for its electrochromic properties[240, 241]. Unlike other configurations of vanadium oxide that have been known to exhibit multiple crystal phases, V_2O_5 exists only as an orthorhombic crystal, which is fundamentally comprised of VO_5 pyramids that form alternating double chains along the *b*-axis[242]. A detailed overview of the crystal structures of all phases of vanadium oxide is provided elsewhere[242].

4.6.2 TE properties of stoichiometric V_2O_5

Kounavis *et al.* have demonstrated that V_2O_5 gels exhibit a room temperature TPF of 0.3 $\mu W/m.K^2$[243]. V_2O_5 films synthesised by sol-gel method exhibit *S* of ~ −200 $\mu V/K$, but have very high resistances of the order of 10^3 to 10^4 Ω[239]. Hence, it is evident that the σ of V_2O_5 films requires significant enhancement for practical refrigeration and energy scavenging applications.

4.6.3 TE properties of nanostructured, doped and composite V_2O_5

Bahgat *et al.* have synthesized highly oriented nanocrystalline, hydrated vanadium pentoxide, ($V_2O_5.n$H_2O) films of 200 nm thickness. The *S* and σ of such films have been shown to increase with temperature, resulting in a peak TPF of 101.25 $\mu W/m.K^2$ at 480 K (Fig. 10a & b) [244].

49

Iwanaga *et al.* have studied the TE properties of V_2O_5 thin films and reported that the introduction of metallic dopants (Na in this case) can improve the TPF values dramatically. This is primarily due to an increase in σ by a factor of up to $\sim 10^4$. At the same time, the S reduces to almost half its value. The direct measurements of TPF have shown an enhanced TPF of 10 μW/m.K^2 (compared to $\sim 10^{-2}$ μW/m.K^2 for pure V_2O_5 films) for 35 % Na doping[245].

Liu *et al.* have shown that polyethylene oxide (PEO) intercalated layered V_2O_5 xerogel nanocomposites result in low TPFs.[246] PbO and ZnO based vandates have also been shown to exhibit S of up to -400 μV/K at room temperature[247]. However, σ in such composites is low, so they can possibly be used only in temperature sensors.
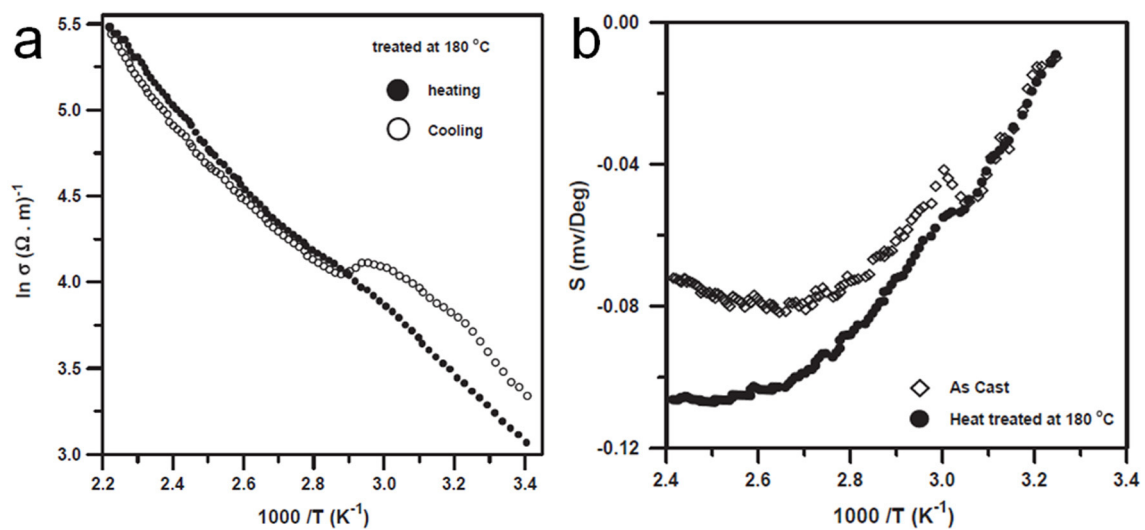
Fig. 10. Temperature dependence of (a) electrical conductivity, (b) Seebeck coefficient for the as-cast and heat treated films during heating and cooling cycles of hydrated V_2O_5. (Reproduced with permission from [244].)

4.6.4 Methods of synthesis

V_2O_5 films can be synthesised using various liquid and vapour phase techniques[248]. Commonly used liquid phase methods for the synthesis of V_2O_5 thin films are the sol-gel and the hydrothermal synthesis technique in which hydrated forms are obtained. The sol-gel

synthesised hydrated nanocrystalline V_2O_5 has been shown to exhibit the highest TPF[244]. A melt quench technique has also been employed to dope various concentrations of Na^+ ions into sol-gel solutions and subsequently, thin films of Na intercalated V_2O_5 can be prepared[243, 245]. Hydrothermal synthesis is often utilized to synthesise V_2O_5 nanostructures such as nanotubes and nanowires[249, 250]. Other liquid phase methods include the electrodeposition and anodization techniques which have also been shown to synthesise V_2O_5 nanostructures[251-253].

Vapour phase techniques such as RF sputtering[254], ALD[255] and PLD[256] have also been shown to deposit crystalline V_2O_5 thin films of various phases. Additionally, the CVD method has also been demonstrated to form highly crystalline V_2O_5 thin films[257]. However, there are few reports on the TE properties of V_2O_5 prepared using vapour deposition techniques.

4.7 Cobalt oxides

4.7.1 Crystal structure

Cobalt oxide based materials have received great attention for their application in gas sensing, heterogeneous catalysts, intercalation compounds for energy storages, electrochromic devices and more recently as TE materials [258, 259]. Cobalt oxides are generally found in two stable oxide compounds: Co_3O_4 and CoO. Co_3O_4 is the more stable of these two. Both Co_3O_4 and CoO exhibit a cubic lattice. Co_3O_4 is a spinel with the presence of both Co^{2+} and Co^{3+} ions in its lattice. Co_3O_4 exhibits a bandgap in the range of 1.4-1.8 eV, while CoO has a higher energy bandgap of 2.2-2.8 eV. Both Co_3O_4 and CoO are usually non-stoichiometric with excess oxygen, leading to p-type semiconducting behaviours[259].

4.7.2 TE properties of stoichiometric cobalt oxides

So far, the TE properties of pure cobalt oxides have not been investigated widely, mainly due to the fact that high resistivities result in a poor TE performance for many energy scavenging applications. It has been shown that in a bulk form CoO exhibits a TPF of ~ 80 μW/m.K^2 at 1000 K[260]. However, the use of various approaches suggested in section 3 such as the addition of metallic dopants, substructuring, and reducing the dimensionality have made doped cobalt oxides the best TMOs for various TE applications.

4.7.3 TE properties of non-stoichiometric, doped, composite and nanostructured cobalt oxides

Rare-earth cobalt oxides ($RECoO_3$) with perovskite crystal structures have been studied for their TE properties for energy scavenging and cooling properties and have shown relatively large figure of merits around the room temperature[82]. Their high-temperature performance is however limited.

P-type cobalt oxide composites are among the TE metal oxides with the largest ZT values reported to date. The most promising cobaltite composites for such TE applications are

52

Na$_x$CoO$_2$ and Ca$_3$Co$_4$O$_9$[78]. The high ZT values are associated with their crystal structures, which consist of CoO$_2^-$ planes composed of edge-sharing CoO$_6$ octahedra, and other structural components between these layers. Na$_x$CoO$_2$ exhibits a weak monoclininc distortion with respect to the hexagonal unit cell caused by the ordering of a layer of sodium ions in between CoO$_2$ planes, while Ca$_3$Co$_4$O$_9$ comprises of a distorted rock-salt type layer of Ca$_2$CoO$_3$, which lowers thermal conductivity by shortening the phonon mean free path (Eq. 2a), and is located between two CdI$_2$ type CoO$_2$ layers that are mainly responsible for providing the path for electrical conduction. Hence, these composites are a classic example of substructuring, which is predicted to enhance TE performance (section 3.2).

Terasaki *et al.* are the pioneers of layered cobalt oxide base TE materials. They were the first group to demonstrate large TPFs of the order of 5×10^3 μW/m.K^2 (compared to 4×10^3 μW/m.K^2 for Bi$_2$Te$_3$) and ZT as high as 0.75 in NaCo$_2$O$_4$ single crystals at room temperature[11]. Fig. 11a & b show the variation of resistivity and *S* with temperature for the NaCo$_2$O$_4$ single crystals[11]. Subsequent studies have shown that polycrystalline Na$_x$CoO$_2$ exhibits TPF as high as 1.4×10^3 μW/m.K^2 for *x* = 0.85 at room temperature[261, 262]. For Na$_x$CoO$_2$, silver (Ag) doping results in the enhancement of ZT[78]. Other metallic dopants such as Cu[95] and Zn[96] have also been shown to increase the TPFs, while Sr doping results in the improvement of ZT[263]. Polycrystalline Na$_x$CoO$_2$ typically shows a peak ZT of ~0.11. However, recently, two-dimensional (2D) and stacked Na$_x$CoO$_2$ nanostructures prepared by exfoliation/restacking method were reported to exhibit enhanced TE properties for energy scavenging applications, as expected from the discussion in section 2[264, 265]. The enhancement was attributed to the reduction of in-plane and cross-plane thermal conductivities in the super-lattice like structures, resulting in enhanced TPFs and ZTs of approximately 500 μW/m.K^2 and 0.4, respectively.

53

On the other hand, undoped $Ca_3Co_4O_9$ exhibits σ, S, κ, TPF and ZT of 10^4 S/m, 150 μV/K, 2 W/m.K, 225 μW/m.K^2 and 0.3, respectively, at elevated temperatures as large as 1000 K. Although, the room temperature TPFs performance of $Ca_3Co_4O_9$ is inferior to Na_xCoO_2, it is more commonly used in various TE applications due to its superior stability to compositional changes and better performance at high temperatures[78].

Similar to Na_xCoO_2, the addition of Ag as a dopant[266, 267] or a second phase composite [266, 268, 269] has been shown to improve TE properties of $Ca_3Co_4O_9$. A $Ca_{2.7}Ag_{0.3}Co_4O_9$/Ag-10 wt% composite showed an enhanced ZT of 0.5 at 1000 K. Bismuth (Bi) doping has also resulted in enhanced TPFs and reduced κ. However, the ZT of Bi-doped samples, is not as high as those of Ag doped oxides. $Ca_{2.75}Gd_{0.25}Co_4O_9$ ceramics have also been shown to exhibit TPF and ZT of 480 μW/m.K^2 and 0.23 respectively, at 923 K (Fig. 11c) [270]. It is seen that the $Ca_{2.75}Gd_{0.25}Co_4O_9$ ceramics synthesised using the SPS method exhibit slightly higher TPFs and ZTs compared to hot press (HP) synthesised samples (Fig. 11c). There are also reports on the doping of $Ca_3Co_4O_9$ with transition metals [271, 272] such as copper and nickel. Gallium addition has been demonstrated to improve TPFs and ZTs[273]. Doping with lanthanum and lanthanide elements has also been studied but the TE enhancements have not been as impressive[78].
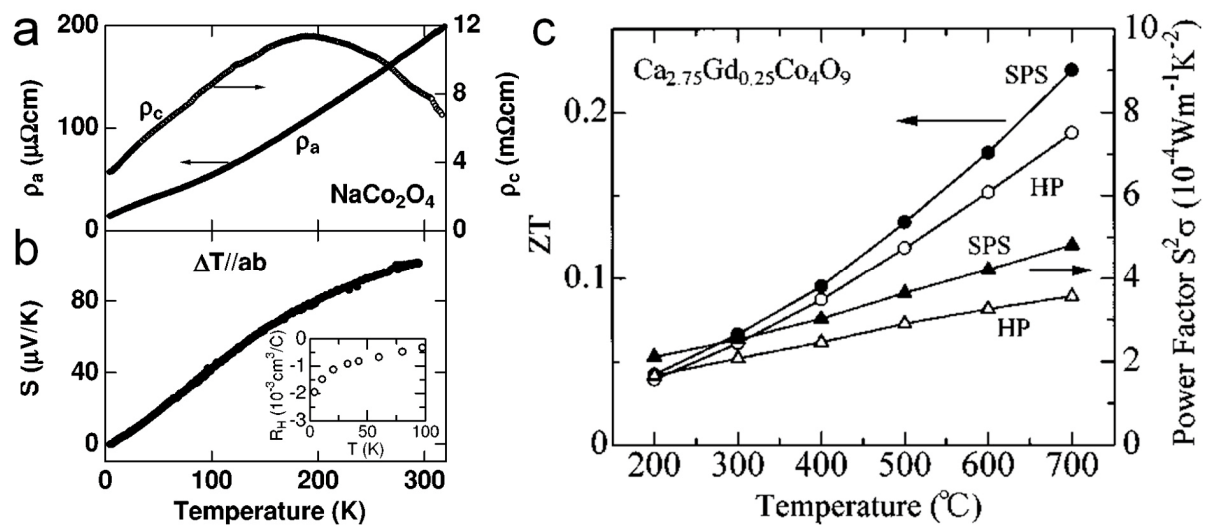
Fig. 11. (a) Resistivity and (b) Seebeck coefficient variations with temperature for $NaCo_2O_4$ single crystals in plane (ρ_a) and out of plane (ρ_c) and (c) comparison of ZT and TPF for SPS and hot pressed (HP) synthesised $Ca_{2.75}Gd_{0.25}Co_4O_9$ samples. (Reproduced with permission from (a), (b) [11] and (c) [270].)

4.7.4 Methods of synthesis

Cobalt oxide can be synthesised using various liquid and vapour phase methods. Epitaxial thin films are generally preferred as they result in highly oriented structures[1, 274, 275]. Liquid phase techniques such as spray pyrolysis, sol-gel and hydrothermal have been employed to fabricate cobalt oxide thin films as well as nanostructures in various morphologies such as nanorods, hierarchical nanocolumns, nanocubes, nanowires and nanorods [258, 276-278]. Although, other liquid phase methods such as electrodeposition have also been employed[279]. An excellent review article summarises various liquid phase synthesis techniques for fabricating cobalt oxide nanostructures[278].

Vapour phase methods that include MBE, PLD and EBE have conventionally been used for the growth of epitaxial $Ca_3Co_4O_9$ films. For Na_xCo_2 films however, the volatility of sodium ions poses difficulties in controlling stoichiometry. The CVD synthesis technique has been shown to be advantageous since it allows accurate tailoring of system composition, structure, morphology *via* suitable choice of a precursor compounds and deposition conditions[258].

4.8 Rhodium oxides – RhO$_x$

4.8.1 Crystal structure

Rhodium oxides are generally found in two crystal oxide compounds: RhO$_2$ and Rh$_2$O$_3$. RhO$_2$ exhibits a tetragonal rutile structure, which transforms into corundum type α-Rh$_2$O$_3$ after annealing above 1000 K[280]. Heating above such temperatures results in a transformation to orthorhombic type β-Rh$_2$O$_3$[281]. Rhodium oxides have been investigated primarily for applications in catalytic chemistry, electrochromisms and as a conductive transparent oxide[282-284]. Additionally, misfit-layered rhodium oxides with two-dimensional CdI$_2$-type crystal structures, analogous to that of cobalt oxides, are among the best candidates for forming p-type TE materials[59]. As in the case for cobalt oxides, their superior thermopower properties originate from CdI$_2$-type layers, which favour low spin state of Rh^{3+}/ Rh^{4+} with degeneracies of spin and orbital as the key factors[285]. The CdI$_2$-type layer has a hexagonal symmetry, while the misfit layer is generally a square lattice. However, a layered Bi-Sr-Rh-O system with fluorite-type misfit layers with a trigonal symmetry has also been reported to exhibit similar TE properties[59].

4.8.2 TE properties of stoichiometric RhO$_x$

There are no reports of stoichiometric RhO$_x$ being employed in TE systems. What follows is a brief overview of the studies on rhodium oxide based metal oxide systems that are among the best p-type TE TMOs.

4.8.3 TE properties of non-stoichiometric, composite and doped RhO$_x$

Okada *et al.* initially reported the first synthesized misfit-layered rhodium based metal oxide in polycrystalline form[286]. Samples of (Bi$_{1-x}$Pb$_x$)$_{1.8}$Sr$_2$Rh$_{1.6}$O$_y$ (*x*=0, 0.1, 0.2) and Bi$_{1.8}$Ba$_2$Rh$_{1.9}$O$_y$ were investigated for their TE properties, with the most promising results being 125 µV/K, 213 S/m and 3.3 µW/m.K^2 for *S*, σ and TPF, respectively, at room temperature (see Fig. 12a-c). In another study, polycrystalline samples of Co and Rh mixed

solutions $Bi_{1.7}Ba_2(Co_{1-z}Rh_z)O_y$ with hexagonal $(Co, Rh)O_2$ layers have been synthesized in an effort to further alter the TE properties by decreasing κ[287]. Although κ was reduced in the solid solution, the σ also dropped due to the distortions made by different ionic size elements in $(Co, Rh)O_2$ layers and therefore, TE performance did not improve.

Kobayashi *et al.* have synthesized rhodium oxide based single crystals in Br-Sr-Rh-O systems with alternately stacked conductive RhO_x and insulating in $(Bi_{0.75}Sr_{0.25})O_{1.5}$ fluorite-type layers[59]. Interestingly, the misfit layer showed a trigonal symmetry with a rhombohedral unit cell, rather than the square-lattice usually observed in other oxides. Room temperature S of up to 63 µV/K and σ of 6.25×10^4 S/m were obtained for $Bi_{0.78}Sr_{0.4}RhO_{3+y}$ crystals. The TPF of such a composite was estimated to be 248 µW/m.K^2, which is comparable to the values for cobalt oxide based systems[59]. Additionally, single crystals of $Ba_{1.2}Rh_8O_{16}$ have been shown to exhibit κ and ZT values of 3 W/m.K and 0.02 at 200 K, respectively[288].

A recent first principle investigation of layered K_xRhO_2 composites based on ab-initio calculations and Boltzmann transport theory has suggested that the material system has the potential for exceptionally remarkable TE properties[289]. Calculations found large Seebeck coefficients in the temperature range of 0 to 700 K for hydrated phase of K_xRhO_2. Moreover a peak value of ZT = 0.3 is predicted for $K_{7/8}RhO_2$ at 100 K, which is higher than Na_xCoO_2 systems. Even at room temperature, TPFs higher than Na_xCoO_2 are predicted[289].
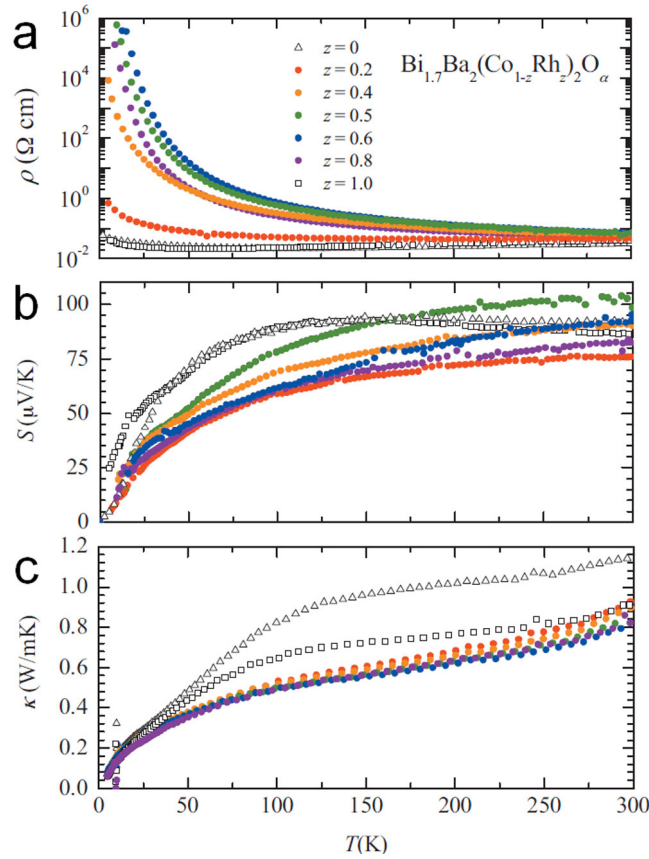
Fig. 12. Temperature (T) dependence of (a) resistivity (ρ), (b) Seebeck coefficient (S), and (c) thermal conductivity (κ) for $Bi_{1.7}Ba_2(Co_{1-z}Rh_z)O_y$ of varying rhodium concentration (z) (Reproduced with permission from [287].)

4.8.4 Methods of synthesis

Many liquid and vapour phase techniques are employed to synthesise rhodium oxides. Amongst the liquid phase synthesis techniques, sol-gel and hydrothermal are the most commonly used methods to synthesise Rh_2O_3 in various morphologies[290-292]. Vapour phase techniques such as RF sputtering, electron beam evaporation (EBE) and the CVD method are used for preparing crystalline rhodium oxide thin films[293]. Misfit, layered rhodium oxide composites such as $(Bi_{1-x}Pb_x)_{1.8}Sr_2Rh_{1.6}O_y$ are synthesised using the SSR technique[286, 287]. It should be considered that RhO_2 is insoluble even in hot aqua regia, hence solution based synthesis techniques are not employed for forming RhO_2. SSR is therefore commonly utilised[294].

4.9 Molybdenum oxides – MoO$_x$

4.9.1 Crystal structure

The most common stoichiometries of MoO$_x$ are MoO$_2$ and MoO$_3$. However, MoO$_3$ is the most widely investigated stoichiometry of MoO$_x$ for a variety of applications such as gas sensing, photochromic devices, light emitting diodes (LEDs), batteries and organic solar cells[238, 295-302]. The most common crystal phases of MoO$_3$ are the thermodynamically stable α-MoO$_3$ and the metastable β-MoO$_3$[303-306]. Bulk α-MoO$_3$ exhibits an indirect bandgap of ~3 eV and has an orthorhombic crystal structure, that comprises of dual layered planar crystals of distorted MoO$_6$ octahedra that are held together by weak van der Waals forces. β-MoO$_3$ on the other hand comprises of MoO$_6$ octahedra that share corners in all the three dimensions, resulting in a monoclinic 3D structure[302, 307]. At temperatures above 620 K, the β phase transforms into the more stable, layered α-MoO$_3$ phase[303, 304].

4.9.2 TE properties of stoichiometric MoO$_x$

There is no literature that reports the TE properties of stoichiometric molybdenum oxides, primarily due to their low σ. However, incorporation of various dopants and implementation of MoO$_x$ composites have been shown to result in high TPFs.

4.9.3 TE properties of non-stoichiometric, doped and composite MoO$_x$

Non-stoichiometric and doped molybdenum oxides have been shown to exhibit high TPFs. Xu *et al.* investigated the TE properties of highly reduced molybdenum oxides (RMo$_8$O$_{14}$) where R=La, Ce, Nd and Sm. Fig. 13a shows the TPFs of the four composites at different temperatures. It is seen that NdMo$_8$O$_{18}$ exhibits a peak TPF and ZT of 177 μW/m.K^2 and 0.1, respectively, at 1000 K. The κ of the composite has been reported to be 3.19 W/m.K at 322 K, which drops to 2 W/m.K at 1164 K[308, 309]. It is evident that the TPF is certainly large enough to make these molybdenum oxide composites promising for high temperature energy scavenging applications.

59

It has also been shown that the use of composites can result in enhanced TE performance as suggested in section 3.4. A study reports that the TPFs of polyaniline (a typical conductive polymer) molybdenum trioxide (PANI/MoO_3) composites, is high. A maximum TPF of ~10^2 μW/m.K^2 was observed for 10 wt% of MoO_3 (Fig. 13b) [310].
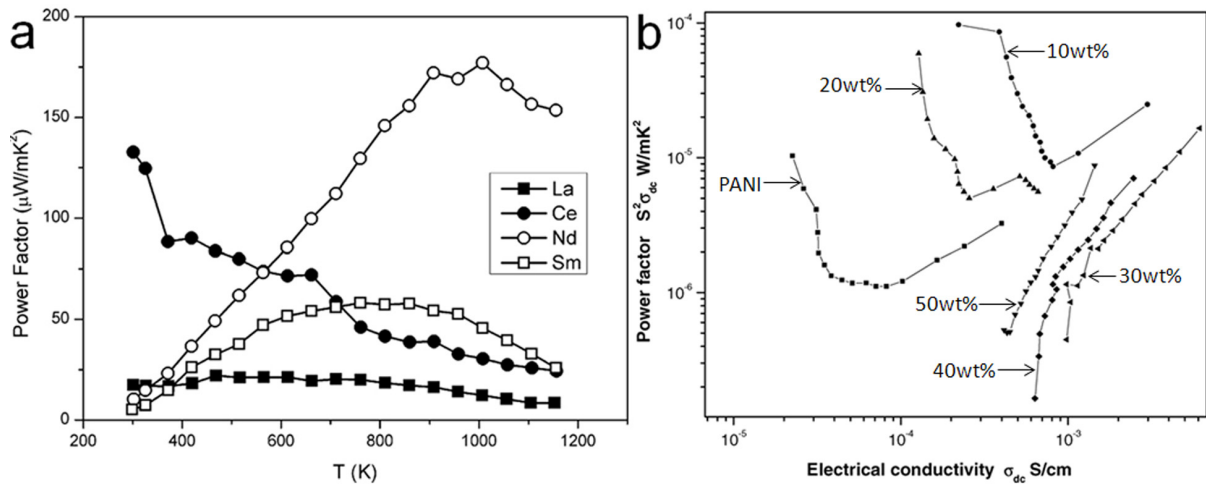
Fig. 13. (a) Temperature dependence of TPF of RMo_8O_{14} (R:La, Ce, Nd, Sm) pellets, and (b) electrical conductivity *vs* TPF of PANI/MoO_3 composites *vs* MoO_3 concentration in the composite. (Reproduced with permission from (a) [309] and (b) [310].)

4.9.4 Methods of synthesis

Similar to other TMOs, MoO_3 can be synthesised using many different liquid and vapour phase techniques. The commonly used liquid phase techniques include sol-gel, hydrothermal, and electrodeposition[304]. Vapour phase techniques such as thermal evaporation, electron beam epitaxy, PLD, RF/DC sputtering, MBE and van der Waal epitaxy (VDWE) have been used for synthesising MoO_3 in various thin film and nanostructured forms. Amongst these, MBE and VDWE have been shown to synthesise ordered, layered MoO_3 structures. Additionally, CVD techniques are also employed to synthesise crystalline MoO_3. A detailed overview of the synthesis techniques to produce various morphologies of MoO_3 is provided elsewhere[302].

4.10 Other transition metal oxides and their TE properties

In this section, we will discuss other TMOs, whose TE properties have not been widely investigated. Most of these TMOs are wide bandgap materials, resulting in extremely poor electrical conductivities. However, a few oxides such as iron oxide, cadmium oxide, nickel oxide and doped zirconium oxide exhibit promising TE properties for various applications. In this section, we provide a brief overview of the small number of reports on the TE properties of the remaining TMOs in their stoichiometric and/or doped states.

4.10.1 Iron oxides

There are many known stable iron oxide stoichiometries available. Amongst them, Fe_2O_3 is the iron oxide compound that has been studied for its TE properties. An analysis of a limited number of reports suggests that Fe_2O_3 can potentially be a promising TMO for TE applications at high temperatures as it exhibits high TPFs at room as well as elevated temperatures

Fe_2O_3 thin films have been shown to exhibit peak S of 1650 μV/K in the temperature range of 270-290 K. A peak σ of 5.5×10^3 S/m has been reported in the same temperature range, resulting in a high TPF of 1.5×10^4 μW/m.K^2[311]. Li- doped α-Fe_2O_3 has been reported to exhibit a TPF of 5.5×10^3 μW/m.K^2 at temperature over 800 K for which a κ of 4 W/m.K has been reported[312]. Fe_2O_3-NiO composites have also been shown to exhibit high TPFs at elevated temperatures (900 μW/m.K^2 at 823 K) [313]. Nanostructuring technique has been predicted to enhance TE performance (section 3.3). Although, 1D electronic quantum confinement has been demonstrated in α-Fe_2O_3 nanorods, they have not been examined for their TE properties[314].

4.10.2 Chromium oxides

There exists many crystalline phases of chromium oxides however, Cr_2O_3 is the most stable bulk form of this TMO,[315] with a few recent reports on its TE properties[311, 316]. Cr_2O_3 thin films have been shown to exhibit S of 3500-4500 μV/K at room temperature. However, we wish to add that such dramatically high S has not been confirmed by any other study so far. A σ of 5.8×10^3 S/m has been reported for stoichiometric Cr_2O_3[311]. Another study demonstrates a TPF of 3.5 μW/m.K^2 at a temperature of 1300 K in Cr_2O_3[316].

The effect of TiO_2 addition to Cr_2O_3 on its TE properties has also been investigated. A 2 % TiO_2 addition results in a slightly improved TPF of 5.6 μW/m.K^2[317].

The TE properties of chromium oxide compounds such as $CuCrO_2$ have also been studied. A maximum TPF and ZT of 236 μW/m.K^2 and 0.1 at 1100 K has been obtained[318]. $CrO_{0.1}N_{0.9}$ polycrystalline samples have also been reported to show a TPF of 80 μW/m.K^2 at 300 K[319].

The above discussion shows that sufficiently large TPFs have been demonstrated for Cr_2O_3 and its compounds. However, further studies are required to establish chromium oxide as a viable TE TMO for many applications.

4.10.3 Scandium oxides

Scandium oxide is a wide band gap (6 eV) insulating material, and is therefore not useful for TE conversion applications[118]. Doping can slightly improve electrical conduction; however, it is still insufficient for any meaningful TE energy scavenging applications. Cu doped scandium oxide epitaxial thin films exhibit S and σ of 40 μV/K and 110 S/m, respectively, at room temperature, resulting in extremely low TPF of 0.18 μW/m.K^2[320].

4.10.4 Zirconium oxides

Zirconium oxides are stable at extremely high temperatures and are generally used as ionic conductors at such temperatures. As such these oxides are frequently used in oxygen sensors and fuel cell membranes[321]. ZrO_2 is the most common crystal phase of zirconium oxides which is found in three phases: a cubic phase with a fluorite structure that occurs at temperatures >2850 K and transforms into a tetragonal phase at 2650 K, which on further cooling transforms to a monoclinic phase[322]. It exhibits a wide bandgap of 5 eV[118].

Pure ZrO_2 does not exhibit good TE properties due to its poor σ. However, ZrO_2/$CoSb_3$ nanocomposites show a peak S of 140 µV/K at 700 K for 5 % ZrO_2 and a corresponding σ and κ of 3.75×10^4 S/m and 2.75 W/m.K, respectively[114]. The resulting TPF and ZT is approximately 735 µW/m.K^2 and 0.2, respectively. Therefore, it is obvious that the incorporation of ZrO_2 can potentially be a good approach for obtaining enhanced TE properties for energy scavenging at elevated temperatures.

4.10.5 Cadmium oxides

Cadmium oxide is an n-type semiconductor, which exhibits a cubic rocksalt type crystal structure with a direct bandgap of ~2.1 eV at room temperature[323]. A study of highly crystalline CdO thin films have revealed high σ of the order of 10^5 S/m and a peak S of – 90 µV/K, resulting in a high TPF of ~800 µW/m.K^2[324]. Another study has demonstrated a TPF of 100 µW/m.K^2 at 700 K[325]. Other studies on pure as well as doped CdO have revealed similar order of magnitude TPFs[326-328]. Therefore, it is evident that CdO can potentially be a viable n-type TE TMO at elevated temperatures.

4.10.6 Nickel oxides

Nickel oxide is a p-type semiconductor that exhibits a cubic rocksalt type crystal structure with a rather large bandgap of 3.6-4.0 eV. Although the σ of stoichiometric NiO is extremely

low, Ni^{2+} vacancies are easily formed in undoped NiO, resulting in dramatic improvements in σ[329].

In the past, a few studies have examined TE properties of NiO[330, 331]. One such study has reported S, σ of 101 μV/K and 10^{-2} S/m respectively, at room temperature. The TPF is extremely low primarily due to poor electrical conductivity[331].

The use of metallic dopants such as Li and Na has been shown to result in enhanced TE properties[332] [333]. Li doped NiO exhibits TPFs of the order of 10^2 μW/m.K^2 at temperatures exceeding 1000 K, suggesting its suitability as a promising metal oxide for energy scavenging and thermopower wave sources[332].

4.10.7 Iridium oxides

IrO$_2$ is the most stable phase of iridium oxides and exhibits a TiO$_2$ like rutile crystal structure. The TE properties of pure IrO$_2$ have not been examined. However, Ca-Ir-O composites have been investigated for their TE properties by Keawprak *et al*[334-336]. They reported low TPFs and ZTs (~35 μW/m.K^2 and 0.01, respectively).

4.10.8 Other TMOs

Other transition metals such as Nb, La, Ac Y, Ta, Re, Hf, Ag and Te are usually employed as dopants in other TE TMOs for tuning their various TE properties in order to achieve higher TPFs and ZTs. However, reports on their stoichiometric TMOs are rare and yet to be fully investigated.

5 Applications of TE TMOs

As discussed in Section 3, the applications of TE TMOs can be classified into four major categories. In this section, a brief description of such TMO-based TE applications is provided.

5.1 Cooling and refrigeration

One of the practical implementation of TE materials is for cooling and refrigeration[3]. TMOs generally do not provide considerable efficiencies for cooling and refrigeration near room temperatures. However, many of them including titanium oxide, copper oxide compounds (La_2CuO_4) and doped cobalt oxides, are promising for cooling and refrigeration applications at low temperatures due to their large TPFs at cryogenic temperatures[337, 338]. The advantage of TMO-based cooling and refrigeration systems is their low cost and easy large-scale fabrication. Many TMOs can be synthesised in low dimensions, using well-established methods which were presented in Section 4, making them attractive for developing micro/nano cooling devices[339]. A schematic of such cooling devices is shown in Fig. 14, and consists of complementary arrays of n-type and p-type TE TMOs, which are electrically in series and thermally in parallel, transferring heat from one side of the module to another[261]. The need for micro-domain cooling is driven largely by the shrinking size of electronic devices. Most electronics and optoelectronic technologies require localised spot cooling of small components and TE modules are capable of very localised cooling[261]. Such modules are extensively used for maintaining laser diodes at constant temperatures in order to stabilise their operating wavelengths [340, 341]. They are also widely used for the temperature management of high power dissipating electronic equipment such as ICs, microprocessors, charge coupled devices (CCD), IR cooling in optoelectronic systems, air conditioners and laboratory cooling plates[67, 342, 343]. Additionally, a reversal of the

65

current allows these devices to act as spot heaters as well, rendering them with additional usage flexibility[344].

Military applications such as night vision systems and heat seeking missiles depend on sensors in their infrared imaging systems. These sensors work efficiently at extremely low temperatures. TE TMO based cooling systems can be used to produce such low temperatures of the order of ~190 K in these devices[67, 345]. Such cooling devices are also increasingly finding applications in the biological world. For a wide cryogenic implementation in the biological world, TMOs due to their non-toxicity and biological compatibility are potentially desirable.
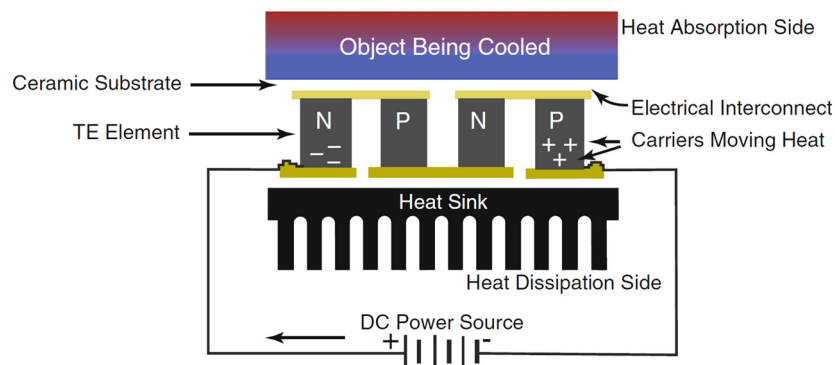

Fig. 14. Pictorial representation of a TE cooling device. (Reproduced with permission from [261].)

5.2 Energy harvesting from heat

The application of TMOs for waste heat recovery is particularly attractive, given their stability at very high temperatures, even though the maximum theoretical efficiencies for TMOs in the high temperature regimes is in the range of 4-6%[346]. Complex oxides such as p-type layered cobaltites and n-type doped $SrTiO_3$, $CaMnO_3$ and ZnO are among the best candidates for TE power generation modules operating at mid to high temperature ranges[12, 347, 348]. Among these, p-type $Ca_3Co_4O_9$ (either undoped or doped with bismuth) and n-type doped $CaMnO_3$ are commonly used in TE modules. TMO TE modules are being increasingly employed for waste heat recovery in vehicles by all major auto-makers in order to comply with stricter emission requirements[78, 349]. Such TE generators convert the waste heat from the exhaust into useful power that can be used to operate the on-board electrical systems, thereby increasing fuel efficiency[4]. Each kilogram of fuel saving reduces CO_2 emissions by 3.16 kg. Additionally, the application of TMO TE modules in the industrial waste heat recovery sector is also gaining increasing attention due to the tremendous economic and environmental benefits that can be realised especially in the aluminium smelting, glass manufacturing and cement production industries.

The first prototypes of power generation modules incorporating TMOs were reported by Shin *et al.* in which an output power of 14 mW was measured at a temperature gradient of 500 K (1000 K on the hot side and 500 K on the cool side) and the efficiency was calculated to be 0.64%[350, 351]. All-oxide TE modules were later developed by Matsubara *et al.* and Funahashi *et al.* that generated output powers as large as 94.4 mW[352, 353]. Subsequently, using the same p- and n-type oxides Funahashi *et al.* fabricated a module comprising of 140 oxide pairs on an alumina substrate resulting in an output power of 0.15 W with a temperature gradient of 551 K[354]. The power generation efficiency was estimated to be around 1.4%. A further improvement in the output power (0.28 W) was achieved through the

fabrication of a pipe-shaped module comprising 54 oxide pairs.[355]. Another plate-shaped module fabricated using 8 pairs of p-type Co-394 and n-type $CaMn_{0.98}Mo_{0.02}O_3$ (Mn-113) bulks on alumina substrate reached an output power of 0.34 W[356]. Other studies with cobalt and manganese based oxides have resulted in output powers of the same order[357-360].

The nanostructuring approach has also been implemented to improve the performance of TMO based TE modules. Such modules use nanostructured p-type cobalates, manganates or n-type ZnO and have been shown to generate powers as high as 0.4 W[361-363].

5.3 Photovoltaic (PV) – solar thermoelectric generators (STEGs) and radioisotope thermoelectric generators (RITEGs)

5.3.1 PV-STEG

Photovoltaic cells are widely deployed to harness solar energy and convert it to useful electrical energy. An interesting idea to improve the efficiency of these cells is the incorporation of TE devices, also known as solar thermoelectric generators (STEGs). These TE-solar hybrid systems can take advantage of the IR part of the solar spectrum, which is not effectively captured by conventional solar cells[364]. This idea was first proposed as early as 1954 by Telkes *et al.* and involves concentrating the solar energy to create heat which is harnessed by the TE systems to convert it into electricity[365]. A schematic of a STEG is shown in Fig. 15. The conversion efficiency of the STEG depends on the temperature difference between the hot (T_H) and the cold (T_C) side. The cooling on the opposite side is provided by circulating a liquid, which can simultaneously be utilised to drive a steam engine or a heating system for auxiliary solar heat utilisation[366]. Solar concentrator systems have been shown to achieve high temperatures of up to 1000 K[366]. At such high temperatures, TMOs are highly desirable due to their high thermal stabilities and acceptable ZT values. In fact, Robert *et al.* have shown that doped cobalt oxides are highly promising for STEGs[366,

367]. Weidenkaff *et al.* and Tomes *et al.* have also demonstrated STEGs based on TMOs such as cobalates, manganates and cuprates[102, 362].

5.3.2 RITEG

The use of radioisotope thermoelectric generators (RITEGs) for powering space missions has been well established. This is because TE converters are extremely reliable for long operating lifetimes. They are compact, rugged, adaptable, and radiation-resistant and they generate no noise, vibrations or torque during the course of operation. Additionally, they do not need any start up device[368]. Spacecraft that venture into the outer universe, where the availability of solar energy is diminished, benefit from the durability and consistency of the electrical as well as thermal energy derived from radioisotope energy sources[369]. The decay of radioactive isotopes generates a significant amount of heat and it is highly desirable to use this heat in spacecraft thermal control, as energy resources are limited. A detailed discussion on the operation of these systems has been presented by Obrien *et al*[370].

The efficiency in such systems is highly sensitive to temperature and high operating temperatures are desirable in order to achieve an effective radiative heat rejection. As such, TE TMOs such as ZnO, ZrO_2 and cobalt oxides offer promising alternatives for any stable and cost effective RITEG development. Lange *et al.* have provided a comprehensive review on the current state-of-the-art RITEG technology and also discussed the scope of future improvements[368].
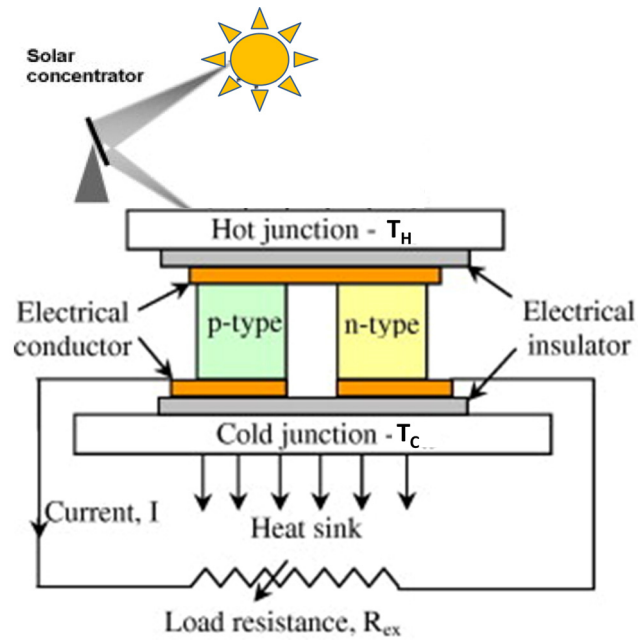
Fig. 15. Schematic of a solar thermoelectric generator (STEG), comprising of a solar concentrator and both p and n type TE elements. (Reproduced with permission from[371].)

5.4 Sensors

TMO-based TE transducers can be implemented for a wide variety of sensing applications. An overview of the different sensing capabilities can be found in ref. [8]. In brief, they can be widely used in measuring temperature[372-375], in measuring generated heat from chemical reactions[376], in gas sensing [377-381] and biological sensing[376, 382]and be incorporated into other sensing systems. In such sensors, a variation in the generated voltages induced due to the Seebeck effect in TE materials are used to assess the sensor performance[383].

For TMO-based temperature sensors, a high S (to generate large output voltage hence obtaining large signal to noise ratios) and low σ (to limit the wastage of energy), κ (to limit the exchange of heat between the measurement point and the rest of the measurment system) are desirable. This ensures that a high sensitivity is maintained for a prolonged time, without an unnecessary exchange of heat.

TMOs such as ZnO, TiO_2 CuO and V_2O_5 have been employed in temperature sensors and infrared detectors[372-375].

Additionally, such thermal sensors can be used to detect various electrical, magnetic, chemical and radiation signals[8, 384]. For high temperature sensing applications, TE TMOs such as ZnO, TiO_2, Fe_2O_3 and ZrO_2 are highly desirable, as they offer high temperature stability and high sensitivities at such elevated temperatures. TMO based sensors can also be integrated with microfluidics to measure very small heat exchanges in biological fluids and biochemical reactions at a wide range of operating temperatures. It is suggested that TMOs such as ZnO can also be ideal materials for such transducers due to their bio-compatibility and good TE properties[43, 385].

The TE properties of TMOs are also exploited for sensing a wide variety of gases. TE gas sensors based on TMOs such as NiO, Co_3O_4, TiO_2 and Fe_2O_3 have already been

71

reported[377-380]. Interestingly, such sensors can operate as both semiconducting and thermoelectric gas sensors, providing unique output information for the operators.

5.5 Thermopower wave sources

Miniaturization of energy sources is a key challenge to overcome in order to develop the next generation of micro/nano electronic devices. Current energy generation technologies cannot be scaled down to the micro/nano level, while maintaining their energy discharge capabilities.

A novel concept of thermopower waves has been demonstrated to be highly promising for the development of the next generation micro/nano scale power sources[5-7, 9, 386]. In such systems, thermopower waves are propagated along a TE system, which generally comprises of a modest to high thermally conductive material. A pictorial representation of a thin film thermopower device is shown in Fig. 16 a. As a result of the coupling of intense exothermic chemical reaction to free charge carriers in the TE material, which should also be highly electrically conducting, an output power is generated. A preferably modest to high κ of the core TE material is required in such thermopower wave sources in order to facilitate the sustained propagation of thermopower waves. High σ is needed to increase the output current and as a result output power. Therefore, thermopower wave sources require materials with a high TPF. TMOs such as ZnO and MnO_2 have resulted in the highest voltage outputs (500 mV and 1.8 V, respectively) (Fig. 16b & c) among all thermopower wave systems reported so far[5-7, 9, 69, 386, 387]. An added advantage is that the high temperature stability of TMOs provides the opportunity of refuelling such systems, as the TE materials remain largely intact after the reaction.
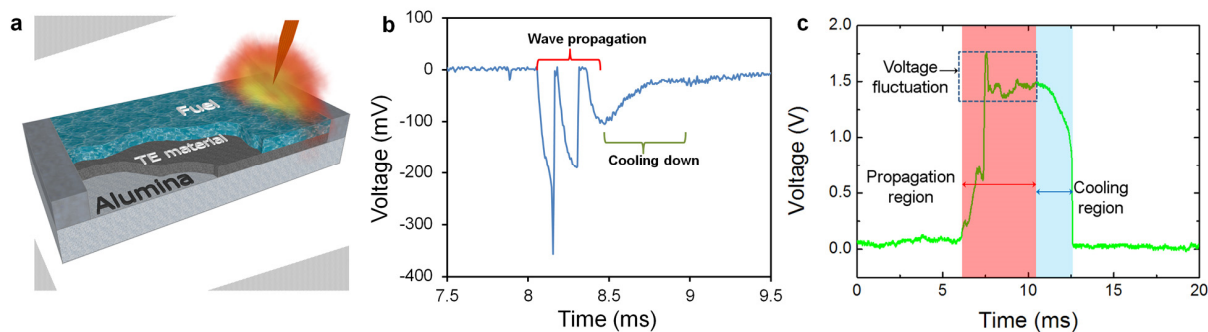
Fig. 16. (a) Schematic of thin film thermopower wave system and output voltage profiles for (b) ZnO and (c) MnO_2 based thermopower wave sources. (Reproduced with permission from (b) [5] and (c) [9].)

6 Conclusion and future outlook

In summary, we presented a comprehensive analysis of various TMOs and their TE properties. The article included an analysis of the theory governing the thermal and electrical conductivities, and Seebeck coefficients of bulk and low dimensional TMOs. An overview of the crystal structures of TMOs, along with various liquid and vapour phase techniques to synthesise them were presented. The effects of stoichiometry alteration, doping, compositing, and nanostructuring were discussed for target TE TMOs at cryogenic, ambient and elevated temperatures, where applicable. Additionally, a description of TE TMOs' major applications was also provided. It was shown that TMOs exhibit promising TE properties that can be exploited for a wide range of applications.

Modification strategies based on reducing dimensions of TMOs have already resulted in enhanced TPFs and ZTs through engineering of their density of states. Enhanced ZTs can certainly be achieved by nanostructuring, substructuring, compositing, doping and changing the stoichiometry of TMOs. Theoretical grounds suggest that even higher ZTs can be obtained. This will enable widespread implementation of such TMOs in a variety of highly efficient cooling and refrigeration, energy scavenging, sensing and thermopower systems even at micro/nano dimensions. Theoretical models predict extraordinary enhancements in

TPFs and figures of merits in TMO based segmented 1D (0D) structures such as QDSLs and SNWs. However, such structures based on TMOs are still in their infancy and there is a need to extensively investigate their TE properties. Such structures will potentially result in dramatic improvements in TPFs and ZTs of TMOs, allowing their widespread implementation.

TMOs offer exciting avenues to harness industrial waste heat, providing cost effective and environmentally friendly electricity generation capabilities. Additionally, TMOs can also be implemented in TE modules for scavenging waste heat from exhausts in automobiles and the heat from the sun for useful power. The efficient implementation of such applications on a large scale inevitably requires high operating temperature ranges for which TMOs are the ideal candidate materials.

TMOs with high Seebeck coefficients and tunable electrical properties can be implemented in temperature, gas and bio sensors with high sensitivities, for applications in which very small heat generations or alteration of electrical and thermal properties should be detected. Many TMOs are biocompatible so they are great candidates in bio-applications. They can also endure low or high extremes of temperatures. TE TMOs can also be used to generate voltages at low dimensions to detect very minute heat exchanges. Such heat exchanger systems can be integrated with nanofluidics in many lab-on-a-chip applications.

The high TPFs of many TMOs at elevated temperatures also makes them attractive materials for thermopower wave sources. Already, TMOs such as ZnO and MnO_2 have resulted in the highest output voltages in such energy sources. Considering that significant enhancements in TPF can be seen in TMOs, achieving output voltages as high as 10 V in thermopower wave sources is not beyond possibility.

74

The environmental compatibility, low cost and highly engineer-able properties are very attractive features that TMOs offer. Alteration of stoichiometry, addition of dopants, formation of composites, nanostructuring and substructuring approaches have already shown their invaluable capabilities to adjust the TE parameters in many TMOs. However, there are still many challenges to be addressed and a fundamental understanding of the TE parameters in TMOs should be fully gained. The low efficiency of TMO-based TE materials is still their major drawback for many applications. Therefore, incorporation of such TMOs into many TE modules has been limited.

The transport phenomena at the boundaries and interfaces will require in-depth investigations to enable further morphological tuning of electrical and thermal properties in TMOs, making them viable candidates in a wide variety of TE applications. There are many unknowns regarding the effects of oxygen deficiency and dopants in TMOs. The same can be said for the effects of nanostructuring, substructuring and compositing. Still, the TE parameters of many TMOs have not been measured at different temperatures. The effects of superconductivity, junctions and environmental conditions have not been investigated for many TMOs and should be studied to gain a complete understanding of their properties. We believe that TMOs will play a pivotal role in the future development of applications such as cooling, heat scavenging, sensing and thermopower wave sources.

Acknowledgements

7 References

[1] Ohta H, Sugiura K, Koumoto K. Recent progress in oxide thermoelectric materials: p-type $Ca_3CO_4O_9$ and n-type $SrTiO_3$. Inorg Chem 2008;47:8429-36.

[2] Biswas K, He JQ, Blum ID, Wu CI, Hogan TP, Seidman DN, et al. High-performance bulk thermoelectrics with all-scale hierarchical architectures. Nature 2012;489:414-8.

[3] Goldsmid HJ, Douglas RW. The use of semiconductors in thermoelectric refrigeration. Brit J Appl Phys 1954;5:386-90.

[4] Tritt TM. Thermoelectric Phenomena, Materials, and Applications. In: Clarke DR, Fratzl P, editors. Ann Rev Mater Res 2011;412011:433-48.

[5] Walia S, Weber R, Balendhran S, Yao D, Abrahamson JT, Zhuiykov S, et al. ZnO based thermopower wave sources. Chem Comm 2012;48:7462-4.

[6] Walia S, Weber R, Latham K, Petersen P, Abrahamson JT, Strano MS, et al. Oscillatory Thermopower Waves Based on Bi_2Te_3 Films. Adv Funct Mater 2011;21:2072-9.

[7] Walia S, Weber R, Sriram S, Bhaskaran M, Latham K, Zhuiykov S, et al. Sb_2Te_3 and Bi_2Te_3 based thermopower wave sources. Energ Environ Sci 2011;4:3558-64.

[8] Riffat SB, Ma XL. Thermoelectrics: a review of present and potential applications. Appl Therm Eng 2003;23:913-35.

[9] Walia S, Balendhran S, Yi P, Yao D, Zhuiykov S, Pannirselvam M, et al. MnO_2 based Thermopower Wave Sources with Exceptionally large Output Voltages. J Phys Chem C 2013;accepted.

[10] Pickett WE. Electronic structure of the high-temperature oxide superconductors. Rev Mod Phys 1989;61:433-512.

[11] Terasaki I, Sasago Y, Uchinokura K. Large thermoelectric power in $NaCo_2O_4$ single crystals. Phys Rev B 1997;56:12685-7.

[12] Koumoto K, Terasaki I, Funahashi R. Complex Oxide Materials for Potential Thermoelectric Applications. MRS Bull 2006;31:206-10.

[13] Terasaki I, Iwakawa M, Nakano T, Tsukuda A, Kobayashi W. Novel thermoelectric properties of complex transition-metal oxides. Dalton T 2010;39:1005-11.

[14] Terasaki I. High-temperature oxide thermoelectrics. J Appl Phys 2011;110.

[15] He J, Liu Y, Funahashi R. Oxide thermoelectrics: The challenges, progress, and outlook. J Mater Res 2011;26:1762.

[16] Snyder GJ, Toberer ES. Complex thermoelectric materials. Nat Mater 2008;7:105-14.

[17] Tritt TM. Thermal conductivity: theory, properties, and applications: Springer; 2005.

[18] Balandin AA. Thermal properties of graphene and nanostructured carbon materials. Nat Mater 2011;10:569-81.

[19] Keyes RW. High-temperature thermal conductivity of insulating crystals-Relationship to the melting point. Phys Rev 1959;115:564-7.

[20] Hicks LD, Dresselhaus MS. Effect of quantum-well structures on the thermoelectric figure of merit Phys Rev B 1993;47:12727-31.

[21] Balandin A, Wang KL. Effect of phonon confinement on the thermoelectric figure of merit of quantum wells. J Appl Phys 1998;84:6149-53.

[22] Koumoto K, Wang YF, Zhang RZ, Kosuga A, Funahashi R. Oxide Thermoelectric Materials: A Nanostructuring Approach. Ann Rev Mater Res 2010;402010:363-94.

[23] Hicks LD, Dresselhaus MS. Thermoelectric figure of merit of a one-dimensional conductor. Phys Rev B 1993;47:16631-4.

[24] Zou J, Balandin A. Phonon heat conduction in a semiconductor nanowire. J Appl Phys 2001;89:2932-8.

[25] Law M, Goldberger J, Yang P. Semiconductor nanowires and nanotubes. Annu Rev Mater Res 2004;34:83-122.

[26] Tian ZR, Voigt JA, Liu J, Mckenzie B, Mcdermott MJ, Rodriguez MA, et al. Complex and oriented ZnO nanostructures. Nat Mater 2003;2:821-6.

[27] Lin YM, Rabin O, Dresselhaus MS. Segmented nanowires: a theoretical study of thermoelectric properties. Inter Conf on Thermoelectrics, Proceedings ICT 2002 2002:265-68.

[28] Lin Y-M, Dresselhaus MS. Thermoelectric properties of superlattice nanowires. Phys Rev B 2003;68:075304.

[29] Heremans JP. Low-dimensional thermoelectricity. Acta Phys Pol A 2005;108:609-34.

[30] Yadav GG, Zhang G, Qiu B, Susoreny JA, Ruan X, Wu Y. Self-templated synthesis and thermal conductivity investigation for ultrathin perovskite oxide nanowires. Nanoscale 2011;3:4078-81.

[31] Tsuda N, Nasu K, Fujimori A, Siratori K. Electronic conduction in oxides. Springer; 2000.

[32] Forro L, Chauvet O, Emin D, Zuppiroli L, Berger H, Levy F. High mobility n-type charge carriers in large single crystals of anatase (TiO_2). J Appl Phys 1994;75:633-5.

[33] Tokura Y, Nagaosa N. Orbital physics in transition-metal oxides. Science 2000;288:462-8.

[34] Henrich VE, Cox PA. The surface science of metal oxides. Cambridge University Press; 1996.

[35] Shakouri A. Recent developments in semiconductor thermoelectric physics and materials. Mater Res 2011;41:399.

[36] Forro L, Chauvet O, Emin D, Zuppiroli L, Berger H, Levy F. High mobility n type charge carriers in large single crystals of anatase (TiO_2). J Appl Phys 1994;75:633-5.

[37] Bauer C, Boschloo G, Mukhtar E, Hagfeldt A. Ultrafast relaxation dynamics of charge carriers relaxation in ZnO nanocrystalline thin films. Chem Phys Lett 2004;387:176-81.

[38] Hendry E, Koeberg M, O'Regan B, Bonn M. Local field effects on electron transport in nanostructured TiO2 revealed by terahertz spectroscopy. Nano Lett 2006;6:755-9.

[39] Johnson JC, Knutsen KP, Yan H, Law M, Zhang Y, Yang P, et al. Ultrafast carrier dynamics in single ZnO nanowire and nanoribbon lasers. Nano Lett 2004;4:197-204.

[40] Canadell E, Whangbo MH. Conceptual aspects of structure-property correlations and electronic instabilities, with applications to low-dimensional transition-metal oxides. Chem Rev 1991;91:965-1034.

[41] Balendhran S, Deng J, Ou JZ, Walia S, Scott J, Tang J, et al. Enhanced Charge Carrier Mobility in Two-Dimensional High Dielectric Molybdenum Oxide. Adv Mater 2013;25:109-14.

[42] Takada K, Sakurai H, Takayama-Muromachi E, Izumi F, Dilanian RA, Sasaki T. Superconductivity in two-dimensional CoO_2 layers. Nature 2003;422:53-5.

[43] Wang ZL. Zinc oxide nanostructures: growth, properties and applications. J Phys: Cond Matter 2004;16:R829.

[44] Sakaki H. Scattering suppression and high-mobility effect of size-quantized electrons in ultrafine semiconductor wire structures. Jpn J Appl Phys 1980;19:L735-L8.

[45] Ramayya EB, Vasileska D, Goodnick SM, Knezevic I. Electron Mobility in Silicon Nanowires. Nanotechnology IEEE Trans 2007;6:113-7.

[46] Lu JG, Chang P, Fan Z. Quasi-one-dimensional metal oxide materials—Synthesis, properties and applications. Mat Sci Eng R: Rep 2006;52:49-91.

[47] Hosono H. Ionic amorphous oxide semiconductors: Material design, carrier transport, and device application. J Non-Cryst solids. 2006;352:851-8.

[48] Comini E, Baratto C, Faglia G, Ferroni M, Vomiero A, Sberveglieri G. Quasi-one dimensional metal oxide semiconductors: Preparation, characterization and application as chemical sensors. Prog Mat Sci 2009;54:1-67.

[49] Vomiero A, Concina I, Comini E, Soldano C, Ferroni M, Faglia G, et al. One-dimensional nanostructured oxides for thermoelectric applications and excitonic solar cells. Nano Energy. 2012;1:372-90.

[50] Wang RY, Feser JP, Lee J-S, Talapin DV, Segalman R, Majumdar A. Enhanced thermopower in PbSe nanocrystal quantum dot superlattices. Nano Lett 2008;8:2283-8.

[51] Dresselhaus MS, Chen G, Tang MY, Yang RG, Lee H, Wang DZ, et al. New directions for low-dimensional thermoelectric materials. Adv Mater 2007;19:1043-53.

[52] Limelette P, Hébert S, Hardy V, Frésard R, Simon C, Maignan A. Scaling behavior in thermoelectric misfit cobalt oxides. Phys Rev Lett 2006;97:46601.

[53] Wang YY, Rogado NS, Cava RJ, Ong NP. Spin entropy as the likely source of enhanced thermopower in $Na_xCo_2O_4$. Nature 2003;423:425-8.

[54] Medlin D, Snyder G. Interfaces in bulk thermoelectric materials: A review for Current Opinion in Colloid and Interface Science. Curr Opin Colloid In 2009;14:226-35.

[55] Zide JMO, Vashaee D, Bian ZX, Zeng G, Bowers JE, Shakouri A, et al. Demonstration of electron filtering to increase the Seebeck coefficient in $In_{(0.53)}Ga_{(0.47)}As/In_{(0.53)}Ga_{(0.28)}Al_{(0.19)}As$ superlattices. Phys Rev B 2006;74.

[56] Ohta H, Kim S, Mune Y, Mizoguchi T, Nomura K, Ohta S, et al. Giant thermoelectric Seebeck coefficient of two-dimensional electron gas in $SrTiO_3$. Nat Mater 2007;6:129-34.

[57] Ohta H. Thermoelectrics based on strontium titanate. Mat Tod 2007;10:44-9.

[58] Motohashi T, Naujalis E, Ueda R, Isawa K, Karppinen M, Yamauchi H. Simultaneously enhanced thermoelectric power and reduced resistivity of NaCoO by controlling Na nonstoichiometry. Appl Phys Lett 2001;79:1480.

[59] Kobayashi W, Hébert S, Pelloquin D, Pérez O, Maignan A. Enhanced thermoelectric properties in a layered rhodium oxide with a trigonal symmetry. Phys Rev B 2007;76:245102.

[60] Zheng HD, Ou JZ, Strano MS, Kaner RB, Mitchell A, Kalantar-Zadeh K. Nanostructured Tungsten Oxide - Properties, Synthesis, and Applications. Adv Funct Mater 2011;21:2175-96.

[61] Breedon M, Rahmani MB, Keshmiri S-H, Wlodarski W, Kalantar-zadeh K. Aqueous synthesis of interconnected ZnO nanowires using spray pyrolysis deposited seed layers. Mater Lett 2010;64:291-4.

[62] Lou XW, Zeng HC. Hydrothermal synthesis of α-MoO_3 nanorods via acidification of ammonium heptamolybdate tetrahydrate. Chem Mater 2002;14:4781-9.

[63] Boukai AI, Bunimovich Y, Tahir-Kheli J, Yu JK, Goddard WA, Heath JR. Silicon nanowires as efficient thermoelectric materials. Nature 2008;451:168-71.

[64] Mahan GD, Sofo JO. The best thermoelectric. P Natl Acad Sci USA. 1996;93:7436-9.

[65] Jie J, Wang G, Han X, Hou J. Synthesis and characterization of ZnO: In nanowires with superlattice structure. J Phys Chem B 2004;108:17027-31.

[66] Devan RS, Patil RA, Lin JH, Ma YR. One-Dimensional Metal-Oxide Nanostructures: Recent Developments in Synthesis, Characterization, and Applications. Adv Funct Mater 2012;22:3326-70.

[67] Bell LE. Cooling, heating, generating power, and recovering waste heat with thermoelectric systems. Science 2008;321:1457-61.

[68] Schieferdecker J, Quad R, Holzenkämpfer E, Schulze M. Infrared thermopile sensors with high sensitivity and very low temperature coefficient. Sensors and Actuat A: Phys 1995;47:422-7.

[69] Choi W, Hong S, Abrahamson JT, Han JH, Song C, Nair N, et al. Chemically driven carbon-nanotube-guided thermopower waves. Nat Mater 2010;9:423-9.

[70] Zebarjadi M, Esfarjani K, Dresselhaus MS, Ren ZF, Chen G. Perspectives on thermoelectrics: from fundamentals to device applications. Energ Environ Sci 2012;5:5147-62.

[71] Chiritescu C, Cahill DG, Nguyen N, Johnson D, Bodapati A, Keblinski P, et al. Ultralow Thermal Conductivity in Disordered, Layered WSe_2 Crystals. Science 2007;315:351-3.

[72] Minnich AJ, Dresselhaus MS, Ren ZF, Chen G. Bulk nanostructured thermoelectric materials: current research and future prospects. Energ Environ Sci 2009;2:466-79.

[73] Mukerjee S, Moore JE. Doping dependence of thermopower and thermoelectricity in strongly correlated materials. Appl Phys Lett 2007;90:112107-3.

[74] Nolas GS, Sharp J, Goldsmid J. Thermoelectrics: basic principles and new materials developments: Springer; 2001.

[75] Poudel B, Hao Q, Ma Y, Lan Y, Minnich A, Yu B, et al. High-thermoelectric performance of nanostructured bismuth antimony telluride bulk alloys. Science 2008;320:634-8.

[76] Sootsman JR, Chung DY, Kanatzidis MG. New and Old Concepts in Thermoelectric Materials. Angew Chem-Int Ed 2009;48:8616-39.

[77] Guilmeau E, Berardan D, Simon C, Maignan A, Raveau B, Ovono DO, et al. Tuning the transport and thermoelectric properties of In_2O_3 bulk ceramics through doping at In-site. J Appl Phys 2009;106:053715-7.

[78] Fergus JW. Oxide materials for high temperature thermoelectric energy conversion. J Eur Cer Soc 2012;32:525-40.

[79] Wang Y, Sui Y, Fan HJ, Wang XJ, Su YT, Su WH, et al. High Temperature Thermoelectric Response of Electron-Doped $CaMnO_3$. Chem Mater 2009;21:4653-60.

[80] Wang Y, Sui Y, Su WH. High temperature thermoelectric characteristics of $Ca_{(0.9)}R_{(0.1)}MnO_{(3)}$ (R=La, Pr, Yb). J Appl Phys 2008;104.

[81] Wang Y, Sui Y, Wang XJ, Su WH. Enhancement of thermoelectric efficiency in (Ca, Dy)MnO_3-(Ca, Yb)MnO_3 solid solutions. Appl Phys Lett 2010;97.

[82] Moon JW, Masuda Y, Seo WS, Koumoto K. Influence of ionic size of rare-earth site on the thermoelectric properties of $RCoO_3$-type perovskite cobalt oxides. Mater Sci Eng B-Solid State Mater Adv Technol 2001;85:70-5.

[83] Ohtaki M, Tsubota T, Eguchi K, Arai H. High-temperature thermoelectric properties of $(Zn_{1-x}Al_x)O$. J Appl Phys 1996;79:1816-8.

[84] Fujishiro Y, Miyata M, Awano M, Maeda K. Characterization of thermoelectric metal oxide elements prepared by the pulse electric-current sintering method. J Am Ceram Soc 2004;87:1890-4.

[85] Kaga H, Kinemuchi Y, Yihnaz H, Watarl K, Nakano H, Nakano H, et al. Orientation dependence of transport property and microstructural characterization of Al-doped ZnO ceramics. Acta Mater 2007;55:4753-7.

[86] Park K, Ko KY, Seo WS, Cho WS, Kim JG, Kim JY. High-temperature thermoelectric properties of polycrystalline $Zn_{1-x-y}Al_xTi_yO$ ceramics. J Eur Ceram Soc 2007;27:813-7.

[87] Cheng H, Xu XJ, Hng HH, Ma J. Characterization of Al-doped ZnO thermoelectric materials prepared by RF plasma powder processing and hot press sintering. Ceram Int 2009;35:3067-72.

[88] Ohtaki M, Araki K, Yamamoto K. High Thermoelectric Performance of Dually Doped ZnO Ceramics. J Electron Mater 2009;38:1234-8.

[89] Wiff JP, Kinemuchi Y, Kaga H, Ito C, Watari K. Correlations between thermoelectric properties and effective mass caused by lattice distortion in Al-doped ZnO ceramics. J Eur Ceram Soc 2009;29:1413-8.

[90] Ma N, Li JF, Zhang BP, Lin YH, Ren LR, Chen GF. Microstructure and thermoelectric properties of $Zn_{1-x}Al_xO$ ceramics fabricated by spark plasma sintering. J Phys Chem Solids 2010;71:1344-9.

[91] Jood P, Mehta RJ, Zhang YL, Peleckis G, Wang XL, Siegel RW, et al. Al-Doped Zinc Oxide Nanocomposites with Enhanced Thermoelectric Properties. Nano Lett 2011;11:4337-42.

[92] Qu XR, Wang W, Lv SC, Jia DC. Thermoelectric properties and electronic structure of Al-doped ZnO. Solid State Commun 2011;151:332-6.

[93] Yamaguchi H, Chonan Y, Oda M, Komiyama T, Aoyama T, Sugiyama S. Thermoelectric Properties of ZnO Ceramics Co-Doped with Al and Transition Metals. J Electron Mater 2011;40:723-7.

[94] Teehan S, Efstathiadis H, Haldar P. Thermoelectric power factor enhancement of AZO/In-AZO quantum well multilayer structures as compared to bulk films. J Alloy Compd 2012;539:129-36.

[95] Park K, Jang K, Kwon HC, Kim JG, Cho WS. Influence of partial substitution of Cu for Co on the thermoelectric properties of $NaCo_2O_4$. J Alloy Compd 2006;419:213-9.

[96] Park K, Lee J. Enhanced thermoelectric properties of $NaCo_2O_4$ by adding ZnO. Mater Lett 2008;62:2366-8.

[97] Georges A, Kotliar G, Krauth W, Rozenberg MJ. Dynamical mean-field theory of strongly correlated fermion systems and the limit of infinite dimensions. Rev Mod Phys 1996;68:13.

[98] Katsnelson MI, Lichtenstein AI. Electronic structure and magnetic properties of correlated metals. Eur Phys J - B 2002;30:9-15.

[99] Restrepo O, Varga K, Pantelides S. First-principles calculations of electron mobilities in silicon: Phonon and Coulomb scattering. Appl Phys Lett 2009;94:212103--3.

[100] Wang Z, Wang S, Obukhov S, Vast N, Sjakste J, Tyuterev V, et al. Thermoelectric transport properties of silicon: Toward an ab initio approach. Phys Rev B 2011;83:205208.

[101] Zebarjadi M, Esfarjani K, Bian Z, Shakouri A. Low-Temperature Thermoelectric Power Factor Enhancement by Controlling Nanoparticle Size Distribution. Nano Lett 2011;11:225.

[102] Weidenkaff A, Robert R, Aguirre M, Bocher L, Lippert T, Canulescu S. Development of thermoelectric oxides for renewable energy conversion technologies. Renew Ener 2008;33:342-7.

[103] Weidenkaff A, Robert R, Aguirre MH, Bocher L, Schlapbach L. Nanostructured thermoelectric oxides with low thermal conductivity. Physica Status Solidi-Rapid Res Lett 2007;1:247-9.

[104] Callaway J. Model for Lattice Thermal Conductivity at Low Temperatures. Phys Rev 1959;113:1046-51.

[105] Broido D, Malorny M, Birner G, Mingo N, Stewart D. Intrinsic lattice thermal conductivity of semiconductors from first principles. Appl Phys Lett 2007;91:231922--3.

[106] Ward A, Broido D. Intrinsic phonon relaxation times from first-principles studies of the thermal conductivities of Si and Ge. Phys Rev B 2010;81:085205.

[107] de Koker N. Thermal conductivity of MgO periclase from equilibrium first principles molecular dynamics. Phys Rev Lett 2009;103:125902.

[108] Esfarjani K, Stokes HT. Method to extract anharmonic force constants from first principles calculations. Phys Rev B 2008;77:144112.

[109] Henry AS, Chen G. Spectral phonon transport properties of silicon based on molecular dynamics simulations and lattice dynamics. J Comput Theoretical Nanosci 2008;5:141-52.

[110] Lundstrom M. Fundamentals of carrier transport: Cambridge University Press; 2009.

[111] Vining CB. A model for the high-temperature transport properties of heavily doped n-type silicon-germanium alloys. J Appl Physics 1991;69:331-41.

[112] Yang RG, Chen G, Dresselhaus MS. Thermal conductivity of simple and tubular nanowire composites in the longitudinal direction. Phys Rev B 2005;72.

[113] He J, Liu YF, Funahashi R. Oxide thermoelectrics: The challenges, progress, and outlook. Journal of Materials Research. 2011;26:1762-72.

[114] Stiewe C, He Z, Platzek D, Karpinski G, Müller E, Li S, et al. Control of thermoelectric properties in $ZrO_2/CoSb_3$ nano-dispersed composites. Materialwissenschaft und Werkstofftechnik. 2007;38:773-6.

[115] Maekawa S, Tohyama T, Barnes SE, Ishihara S, Koshibae W, Khaliullin G. Physics of transition metal oxides: Springer; 2004.

[116] Cox PA. Transition metal oxides: an introduction to their electronic structure and properties. Oxford Univ Pr; 2010.

[117] Rao CNR, Raveau B. Transition Metal Oxides: Structure, Properties, and Synthesis of Ceramic Oxides. Wiley; 1998.

[118] Emeline AV, Kataeva GV, Ryabchuk VK, Serpone N. Photostimulated generation of defects and surface reactions on a series of wide band gap metal-oxide solids. J Phys Chem B 1999;103:9190-9.

[119] Matsui M, Akaogi M. Molecular dynamics simulation of the structural and physical properties of the four polymorphs of TiO_2. Molecular Simulation 1991;6:239-44.

[120] Zhang HZ, Banfield JF. Understanding polymorphic phase transformation behavior during growth of nanocrystalline aggregates: Insights from TiO_2. J Phys Chem B 2000;104:3481-7.

[121] Diebold U. The surface science of titanium dioxide. Surf Sci Rep 2003;48:53-229.

[122] Bavykin DV, Friedrich JM, Walsh FC. Protonated titanates and TiO_2 nanostructured materials: Synthesis, properties, and applications. Adv Mater 2006;18:2807-24.

[123] He QY, Hao Q, Chen G, Poudel B, Wang XW, Wang DZ, et al. Thermoelectric property studies on bulk TiO_x with x from 1 to 2. Appl Phys Lett 2007;91.

[124] Lu Y, Hirohashi M, Sato K. Thermoelectric properties of non-stoichiometric titanium dioxide TiO_{2-x} fabricated by reduction treatment using carbon powder. Mater Trans. 2006;47:1449-52.

[125] Tang JK, Wang WD, Zhao GL, Li Q. Colossal positive Seebeck coefficient and low thermal conductivity in reduced TiO_2. J Phys-Cond Matter 2009;21.

[126] Tsuyumoto I, Hosono T, Murata M. Thermoelectric power in nonstoichiometric orthorhombic titanium oxides. J Am Ceram Soc 2006;89:2301-3.

[127] Bak T, Nowotny MK, Sheppard LR, Nowotny J. Effect of prolonged oxidation on semiconducting properties of titanium dioxide. J Phys Chem C 2008;112:13248-57.

[128] Miao L, Tanemura S, Huang R, Liu CY, Huang CM, Xu G. Large Seebeck Coefficients of Protonated Titanate Nanotubes for High-Temperature Thermoelectric Conversion. ACS Appl Mater Interfaces 2010;2:2355-9.

[129] Kurita D, Ohta S, Sugiura K, Ohta H, Koumoto K. Carrier generation and transport properties of heavily Nb-doped anatase TiO_2 epitaxial films at high temperatures. J Appl Phys 2006;100.

[130] Sheppard LR, Bak T, Nowotny J. Electrical properties of niobium-doped titanium dioxide. 3. Thermoelectric power. J Phys Chem C 2008;112:611-7.

[131] Sheppard LR, Bak T, Nowotny J. Electrical properties of niobium-doped titanium dioxide. 1. Defect disorder. J Phys Chem B 2006;110:22447-54.

[132] Okuda T, Nakanishi K, Miyasaka S, Tokura Y. Large thermoelectric response of metallic perovskites: $Sr_{1-x}La_xTiO_3$ ($0 <= x <= 0.1$). Phys Rev B 2001;63.

[133] Ohta S, Nomura T, Ohta H, Koumoto K. High-temperature carrier transport and thermoelectric properties of heavily La- or Nb-doped $SrTiO_3$ single crystals. J Appl Phys 2005;97.

[134] Ravichandran J, Siemons W, Oh DW, Kardel JT, Chari A, Heijmerikx H, et al. High-temperature thermoelectric response of double-doped $SrTiO_3$ epitaxial films. Phys Rev B 2010;82.

[135] Jalan B, Stemmer S. Large Seebeck coefficients and thermoelectric power factor of La-doped SrTiO3 thin films. Appl Phys Lett 2010;97.

[136] Muta H, Kurosaki K, Yamanaka S. Thermoelectric properties of rare earth doped $SrTiO_3$. J Alloy Compd 2003;350:292-5.

[137] Yamamoto M, Ohta H, Koumoto K. Thermoelectric phase diagram in a $CaTiO_3$-$SrTiO_3$-$BaTiO_3$ system. Appl Phys Lett 2007;90.

[138] Lakshmi BB, Patrissi CJ, Martin CR. Sol-gel template synthesis of semiconductor oxide micro- and nanostructures. Chem Mater. 1997;9:2544-50.

[139] Zhang LH, Tosho T, Okinaka N, Akiyama T. Thermoelectric properties of combustion-synthesized lanthanum-doped strontium titanate. Mater Trans 2007;48:1079-83.

[140] Wei WF, Cui XW, Chen WX, Ivey DG. Manganese oxide-based materials as electrochemical supercapacitor electrodes. Chem Soc Rev 2011;40:1697-721.

[141] Xiao W, Wang DL, Lou XW. Shape-Controlled Synthesis of MnO_2 Nanostructures with Enhanced Electrocatalytic Activity for Oxygen Reduction. J Phys Chem C 2010;114:1694-700.

[142] Song FF, Wu LM, Liang S. Giant Seebeck coefficient thermoelectric device of MnO_2 powder. Nanotechnology 2012;23.

[143] Cockayne E, Li L. First-principles DFT+U studies of the atomic, electronic, and magnetic structure of alpha-MnO_2 (cryptomelane). Chem Phys Lett 2012;544:53-8.

[144] Post JE, Vondreele RB, Buseck PR. Symmetry and cation displacements in hollandites-Structure refinements of hollandite, cryptomelane and priderite. Acta Cryst Sect B-Struct Sci 1982;38:1056-65.

[145] Devaraj S, Munichandraiah N. Effect of crystallographic structure of MnO_2 on its electrochemical capacitance properties. J Phys Chem C 2008;112:4406-17.

[146] Preisler E. Semiconductor properties of manganese dioxide. J Appl Electrochem 1976;6:311-20.

[147] Ul Islam A, Islam R, Khan KA. Studies on the thermoelectric effect in semiconducting MnO_2 thin films. Journal of Materials Science-Materials in Electronics. 2005;16:203-7.

[148] Ang R, Lu WJ, Zhang RL, Zhao BC, Zhu XB, Song WH, et al. Effects of Co doping in bilayered manganite $LaSr_2Mn_2O_7$: Resistivity, thermoelectric power, and thermal conductivity. Phys Rev B 2005;72.

[149] Zhang FP, Lu QM, Zhang X, Zhang JX. First principle investigation of electronic structure of $CaMnO_3$ thermoelectric compound oxide. J Alloy Compd 2011;509:542-5.

[150] Flahaut D, Mihara T, Funahashi R, Nabeshima N, Lee K, Ohta H, et al. Thermoelectrical properties of A-site substituted $Ca_{1-x}Re_xMnO_3$ system. J Appl Phys 2006;100.

[151] Sato H, Enoki T, Isobe M, Ueda Y. Transport properties and magnetism of a helically Hund-coupled conductor: beta-MnO_2. Phys Rev B 2000;61:3563-9.

[152] Zhang X, Yang WS, Yang JJ, Evans DG. Synthesis and characterization of alpha-MnO_2 nanowires: Self-assembly and phase transformation to beta-MnO_2 microcrystals. J Cryst Growth 2008;310:716-22.

[153] Wang X, Li YD. Synthesis and formation mechanism of manganese dioxide nanowires/nanorods. Chem- Eur Jour 2003;9:300-6.

[154] Devenney M, Donne S, Gorer S. Application of combinatorial methodologies to the synthesis and characterization of electrolytic manganese dioxide. J Appl Electrochem 2004;34:643-51.

[155] Chou S, Cheng F, Chen J. Electrodeposition synthesis and electrochemical properties of nanostructured γ-MnO_2 films. J Power Sour 2006;162:727-34.

[156] Dong B, Xue T, Xu C-L, Li H-L. Electrodeposition of mesoporous manganese dioxide films from lyotropic liquid crystalline phases. Micropor Mesopor Mat 2008;112:627-31.

[157] Wang X, Wang X, Huang W, Sebastian P, Gamboa S. Sol–gel template synthesis of highly ordered MnO_2 nanowire arrays. J Power Sour 2005;140:211-5.

[158] Nilsen O, Fjellvåg H, Kjekshus A. Growth of manganese oxide thin films by atomic layer deposition. Thin Solid Films 2003;444:44-51.

[159] Isber S, Majdalani E, Tabbal M, Christidis T, Zahraman K, Nsouli B. Study of manganese oxide thin films grown by pulsed laser deposition. Thin Solid Films 2009;517:1592-5.

[160] Guo LW, Peng DL, Makino H, Hanada T, Hong SK, Sumiyama K, et al. Structural characteristics and magnetic properties of MnO_2 films grown by plasma-assisted molecular beam epitaxy. J Appl Phys 2001;90:351-4.

[161] Wang HQ, Dong X, Peng SJ, Dong L, Wang Y. Improvement of thermoelectric properties of WO_3 ceramics by ZnO addition. J Alloy Compd 2012;527:204-9.

[162] Salje EKH, Rehmann S, Pobell F, Morris D, Knight KS, Herrmannsdorfer T, et al. Crystal structure and paramagnetic behaviour of epsilon-WO_{3-x}. J Phys-Cond Matter. 1997;9:6563-77.

[163] Vogt T, Woodward PM, Hunter BA. The high-temperature phases of WO_3. J Sol State Chem 1999;144:209-15.

[164] Goulding MR, Thomas CB. Transport properties of amorphous films of tungstic oxide sublimed under different conditions. Thin Solid Films 1979;62:175-88.

[165] Patil PS, Patil PR, Ennaoui EA. Characterization of ultrasonic spray pyrolyzed tungsten oxide thin films. Thin Solid Films 2000;370:38-44.

[166] Makarov VO, Trontelj M. Sintering and electrical conductivity of doped WO_3. J Eur Cer Soc 1996;16:791-4.

[167] Vemuri RS, Bharathi KK, Gullapalli SK, Ramana CV. Effect of Structure and Size on the Electrical Properties of Nanocrystalline WO_3 Films. ACS Appl Mater Inter 2010;2:2623-8.

[168] Hutchins MG, Abu-Alkhair O, El-Nahass MM, Abdel-Hady K. Electrical conduction mechanisms in thermally evaporated tungsten trioxide (WO_3) thin films. J Phys-Cond Matter. 2006;18:9987-97.

[169] Wang HT, Xu YB, Goto M, Tanaka Y, Yamazaki M, Kasahara A, et al. Thermal conductivity measurement of tungsten oxide nanoscale thin films. Mater Trans 2006;47:1894-7.

83

[170] Molenda J, Kubik A. Transport properties and reactivity of tungsten trioxide. Solid State Ionics. 1999;117:57-64.

[171] Wang HQ, Hua ZQ, Peng SJ, Dong X, Dong L, Wang Y. Effect of CeO_2 on the thermoelectric properties of WO_3-based ceramics. Cer Inter 2012;38:1133-7.

[172] Patil PS, Mujawar SH, Inamdar AI, Shinde PS, Deshmukh HP, Sadale SB. Structural, electrical and optical properties of TiO_2 doped WO_3 thin films. Appl Surf Sci 2005;252:1643-50.

[173] Marsen B, Miller EL, Paluselli D, Rocheleau RE. Progress in sputtered tungsten trioxide for photoelectrode applications. Int J Hydrogen Ener 2007;32:3110-5.

[174] Cantalini C, Sun H, Faccio M, Pelino M, Santucci S, Lozzi L, et al. NO_2 sensitivity of WO_3 thin film obtained by high vacuum thermal evaporation. Sensors and Actuat B: Chem 1996;31:81-7.

[175] Breedon M, Spizzirri P, Taylor M, du Plessis J, McCulloch D, Zhu J, et al. Synthesis of Nanostructured Tungsten Oxide Thin Films: A Simple, Controllable, Inexpensive, Aqueous Sol− Gel Method. Cryst Growth & Des 2009;10:430-9.

[176] Baeck S, Jaramillo T, Stucky G, McFarland E. Controlled electrodeposition of nanoparticulate tungsten oxide. Nano Lett 2002;2:831-4.

[177] Kalantar-zadeh K, Sadek AZ, Zheng H, Bansal V, Bhargava SK, Wlodarski W, et al. Nanostructured WO_3 films using high temperature anodization. Sensors and Actuat B: Chem 2009;142:230-5.

[178] Zhao Y, Feng Z-C, Liang Y. Pulsed laser deposition of WO_3-base film for NO_2 gas sensor application. Sensors and Actuat B: Chem 2000;66:171-3.

[179] Sivakumar R, Gopalakrishnan R, Jayachandran M, Sanjeeviraja C. Preparation and characterization of electron beam evaporated WO_3 thin films. Opt Mater 2007;29:679-87.

[180] Buchine BA, Hughes WL, Degertekin FL, Wang ZL. Bulk acoustic resonator based on piezoelectric ZnO belts. Nano Lett 2006;6:1155-9.

[181] He JH, Hsin CL, Liu J, Chen LJ, Wang ZL. Piezoelectric gated diode of a single ZnO nanowire. Adv Mater 2007;19:781-4.

[182] Lu M-P, Song J, Lu M-Y, Chen M-T, Gao Y, Chen L-J, et al. Piezoelectric nanogenerator using p-type ZnO nanowire arrays. Nano Lett 2009;9:1223-7.

[183] Wang ZL, Song J. Piezoelectric nanogenerators based on zinc oxide nanowire arrays. Science 2006;312:242-6.

[184] Coleman V, Jagadish C. Basic properties and applications of ZnO. Zinc Oxide Bulk, Thin films and Nanostructures, Processing, Properties and Applications. 1st ed. Elsevier; 2006.

[185] Ong KP, Singh DJ, Wu P. Analysis of the thermoelectric properties of n-type ZnO. Phys Rev B 2011;83.

[186] Kinemuchi Y, Mikami M, Kobayashi K, Watari K, Hotta Y. Thermoelectric Properties of Nanograined ZnO. J Electron Mater 2010;39:2059-63.

[187] Fujishiro Y, Miyata M, Awano M, Maeda K. Effect of microstructural control on thermoelectric properties of hot-pressed aluminum-doped zinc oxide. J Am Ceram Soc 2003;86:2063-6.

[188] Kim KH, Shim SH, Shim KB, Niihara K, Hojo J. Microstructural and thermoelectric characteristics of zinc oxide-based thermoelectric materials fabricated using a spark plasma sintering process. J Am Ceram Soc 2005;88:628-32.

[189] Park K, Ko KY. Effect of TiO_2 on high-temperature thermoelectric properties of ZnO. J Alloy Compd 2007;430:200-4.

[190] Park K, Seong JK. Influence of simultaneous addition of Sb_2O_3 and SnO_2 on thermoelectric properties of $Zn_{1-x-y}Sb_xSn_yO$ prepared by tape casting. J Alloy Compd 2008;464:1-5.

[191] Park K, Seong JK, Kwon Y, Nahm S, Cho WS. Influence of SnO_2 addition on the thermoelectric properties of $Zn_{1-x}Sn_xO$(0.01 <= x <= 0.05). Mater Res Bull 2008;43:54-61.

[192] Park K, Seong JK, Nahm S. Improvement of thermoelectric properties with the addition of Sb to ZnO. J Alloy Compd 2008;455:331-5.

[193] Guilmeau E, Maignan A, Martin C. Thermoelectric Oxides: Effect of Doping in Delafossites and Zinc Oxide. J Electron Mater 2009;38:1104-8.

[194] Park K, Seong JK, Kim GH. NiO added $Zn_{1-x}Ni_xO$ (0 <= x <= 0.05) for thermoelectric power generation. J Alloy Compd 2009;473:423-7.

[195] Berardan D, Byl C, Dragoe N. Influence of the Preparation Conditions on the Thermoelectric Properties of Al-Doped ZnO. J Am Ceram Soc 2010;93:2352-8.

[196] Colder H, Guilmeau E, Harnois C, Marinel S, Retoux R, Savary E. Preparation of Ni-doped ZnO ceramics for thermoelectric applications. J Eur Ceram Soc 2011;31:2957-63.

[197] Michiue Y, Mori T, Prytuliak A, Matsushita Y, Tanaka M, Kimizuka N. Electrical, optical, and thermoelectric properties of $Ga_2O_3(ZnO)_{(9)}$. RSC Adv 2011;1:1788-93.

[198] Jung KH, Lee KH, Seo WS, Choi SM. An enhancement of a thermoelectric power factor in a Ga-doped ZnO system: A chemical compression by enlarged Ga solubility. Appl Phys Lett 2012;100.

[199] Paul GK, Sen SK. Sol-gel preparation, characterization and studies on electrical and thermoelectrical properties of gallium doped zinc oxide films. Mater Lett 2002;57:742-6.

[200] Gregoryz OJ, Amani M. Thermoelectric Properties of $Zn_xIn_yO_{x+1.5y}$ Films. J Electrochem Soc 2011;158:J15-J9.

[201] Seo DK, Shin S, Cho HH, Kong BH, Whang DM, Cho HK. Drastic improvement of oxide thermoelectric performance using thermal and plasma treatments of the InGaZnO thin films grown by sputtering. Acta Mater 2011;59:6743-50.

[202] Shi LH, Chen J, Zhang G, Li BW. Thermoelectric figure of merit in Ga-doped 0001 ZnO nanowires. Phys Lett A. 2012;376:978-81.

[203] Yang Y, Pradel KC, Jing Q, Wu JM, Zhang F, Zhou Y, et al. Thermoelectric Nanogenerators Based on Single Sb-Doped ZnO Micro/Nanobelts. ACS Nano 2012;6:6984-9.

[204] Rodríguez-Gattorno G, Santiago-Jacinto P, Rendon-Vazquez L, Németh J, Dékány I, Díaz D. Novel synthesis pathway of ZnO nanoparticles from the spontaneous hydrolysis of zinc carboxylate salts. J Phys Chem B 2003;107:12597-604.

[205] Caglar M, Ilican S, Caglar Y, Yakuphanoglu F. The effects of Al doping on the optical constants of ZnO thin films prepared by spray pyrolysis method. J Mater Sci-Mater El 2008;19:704-8.

[206] Zhang J, Sun L, Yin J, Su H, Liao C, Yan C. Control of ZnO morphology via a simple solution route. Chem Mater 2002;14:4172-7.

[207] Kamalasanan M, Chandra S. Sol-gel synthesis of ZnO thin films. Thin Solid Films 1996;288:112-5.

[208] Choi K-S, Lichtenegger HC, Stucky GD, McFarland EW. Electrochemical synthesis of nanostructured ZnO films utilizing self-assembly of surfactant molecules at solid-liquid interfaces. J Am Chem Soc 2002;124:12402-3.

[209] He S, Zheng M, Yao L, Yuan X, Li M, Ma L, et al. Preparation and properties of ZnO nanostructures by electrochemical anodization method. Appl Surf Sci 2010;256:2557-62.

[210] Banerjee A, Ghosh C, Chattopadhyay K, Minoura H, Sarkar AK, Akiba A, et al. Low-temperature deposition of ZnO thin films on PET and glass substrates by DC-sputtering technique. Thin Solid Films 2006;496:112-6.

[211] Yi G-C, Wang C, Park WI. ZnO nanorods: synthesis, characterization and applications. Semicond Sci Tech 2005;20:S22.

[212] Pung S-Y, Choy K-L, Hou X, Shan C. Preferential growth of ZnO thin films by the atomic layer deposition technique. Nanotechnology 2008;19:435609.

[213] Gonzalez-Valls I, Lira-Cantu M. Vertically-aligned nanostructures of ZnO for excitonic solar cells: a review. Ener Environ Sci 2009;2:19-34.

[214] Kim KH, Shim SH, Shim KB, Niihara K, Hojo J. Microstructural and Thermoelectric Characteristics of Zinc Oxide-Based Thermoelectric Materials Fabricated Using a Spark Plasma Sintering Process. J Am Ceram Soc 2005;88:628-32.

[215] Jin B, Im S, Lee S. Violet and UV luminescence emitted from ZnO thin films grown on sapphire by pulsed laser deposition. Thin Solid Films 2000;366:107-10.

[216] Gou X, Wang G, Yang J, Park J, Wexler D. Chemical synthesis, characterisation and gas sensing performance of copper oxide nanoribbons. J Mater Chem 2008;18:965-9.

[217] Ito T, Yamaguchi H, Okabe K, Masumi T. Single-crystal growth and characterization of Cu_2O and CuO. J Mater Sci 1998;33:3555-66.

[218] Yin M, Wu C-K, Lou Y, Burda C, Koberstein JT, Zhu Y, et al. Copper oxide nanocrystals. J Am Chem Soc 2005;127:9506-11.

[219] Zirin MH, Trivich D. Thermoelectric effect in single-crystal cuprous oxide at high temperatures. J Chem Phys 1963;39:870-&.

[220] Balamurugan B, Mehta B. Optical and structural properties of nanocrystalline copper oxide thin films prepared by activated reactive evaporation. Thin Solid Films 2001;396:90-6.

[221] Muhibbullah M, Hakim MO, Choudhury MGM. Studies on Seebeck effect in spray deposited CuO thin film on glass substrate. Thin Solid Films 2003;423:103-7.

[222] Jeong YK, Choi GM. Nonstoichiometry and electrical conduction of CuO. J Phys Chem Solids. 1996;57:81-4.

[223] Koffyberg FP, Benko FA. A Photo-Electrochemical determination of the position of the conduction and valence band edges of p type CuO. J Appl Phys 1982;53:1173-7.

[224] Yu JD, Inaguma Y, Itoh M, Oguni M, Kyomen T. Effect of oxygen content on the anomalies at successive phase transitions of $La_2CuO_{4+delta}$ single crystal below 320 K. Phys Rev B 1996;54:7455-61.

[225] Hord R, Luetkens H, Pascua G, Buckow A, Hofmann K, Krockenberger Y, et al. Enhanced two-dimensional behavior of metastable $T-La_2CuO_4$, the parent compound of electron-doped cuprate superconductors. Phys Rev B 2010;82.

[226] Liu Y, Lin YH, Zhang BP, Zhu HM, Nan CW, Lan JL, et al. High-Temperature Thermoelectric Properties in the $La_{2-x}R_xCuO_4$ (R: Pr, Y, Nb) Ceramics. J Am Ceram Soc 2009;92:934-7.

[227] Yamanaka S, Kobayashi H, Kurosaki K. Thermoelectric properties of layered rare earth copper oxides. J Alloy Compd 2003;349:321-4.

[228] Armelao L, Barreca D, Bertapelle M, Bottaro G, Sada C, Tondello E. A sol–gel approach to nanophasic copper oxide thin films. Thin Solid Films 2003;442:48-52.

[229] Li S, Zhang H, Ji Y, Yang D. CuO nanodendrites synthesized by a novel hydrothermal route. Nanotechnology 2004;15:1428.

[230] Kosugi T, Kaneko S. Novel Spray-Pyrolysis Deposition of Cuprous Oxide Thin Films. J Am Ceram Soc 2005;81:3117-24.

[231] Allam NK, Grimes CA. Electrochemical fabrication of complex copper oxide nanoarchitectures copper anodization in aqueous and non-aqueous electrolytes. Mat Lett 2011;65:1949-55.

[232] Switzer JA, Kothari HM, Poizot P, Nakanishi S, Bohannan EW. Enantiospecific electrodeposition of a chiral catalyst. Nature 2003;425:490-3.

[233] Maruyama T. Copper oxide thin films prepared by chemical vapor deposition from copper dipivaloylmethanate. Sol Ener Mat Sol C 1998;56:85-92.

[234] Eyert V, Höck K-H. Electronic structure of V_2O_5: Role of octahedral deformations. Phys Rev B 1998;57:12727.

[235] Cao AM, Hu JS, Liang HP, Wan LJ. Self-assembled vanadium pentoxide (V_2O_5) hollow microspheres from nanorods and their application in lithium-ion batteries. Angew Chem-Int Ed 2005;44:4391-5.

[236] Sides CR, Martin CR. Nanostructured electrodes and the low-temperature performance of Li-ion batteries. Adv Mater 2005;17:125.

[237] Liu J, Xia H, Xue DF, Lu L. Double-Shelled Nanocapsules of V_2O_5-Based Composites as High-Performance Anode and Cathode Materials for Li Ion Batteries. J Am Chem Soc 2009;131:12086-+.

[238] Chernova NA, Roppolo M, Dillon AC, Whittingham MS. Layered vanadium and molybdenum oxides: batteries and electrochromics. J Mater Chem 2009;19:2526-52.

[239] El Mandouh ZS, Selim MS. Physical properties of vanadium pentoxide sol gel films. Thin Solid Films 2000;371:259-63.

[240] Talledo A, Granqvist CG. Electrochromic vanadium-pentoxide based films-Structural,Electrochemical and optical properties. J Appl Phys 1995;77:4655-66.

[241] Xiong CR, Aliev AE, Gnade B, Balkus KJ. Fabrication of silver vanadium oxide and V2O5 nanowires for electrochromics. ACS Nano 2008;2:293-301.

[242] Darling RB, Iwanaga S. Structure, properties, and MEMS and microelectronic applications of vanadium oxides. Sadhana-Academy Proc Eng Sci 2009;34:531-42.

[243] Kounavis P, Vomvas A, Mytilineou E, Roilos M, Murawski L. Thermopower, conductivity and the Hall-effect in V_2O_5 gels. J Phys C-Sol State Phys 1988;21:967-73.

[244] Bahgat AA, Ibrahim FA, El-Desoky MM. Electrical and optical properties of highly oriented nanocrystalline vanadium pentoxide. Thin Solid Films 2005;489:68-73.

[245] Iwanaga S, Marciniak M, Darling RB, Ohuchi FS. Thermopower and electrical conductivity of sodium-doped V_2O_5 thin films. J Appl Phys 2007;101.

[246] Liu YJ, Schindler JL, DeGroot DC, Kannewurf CR, Hirpo W, Kanatzidis MG. Synthesis, structure, and reactions of poly(ethylene oxide) V_2O_5 intercalative nanocomposites. Chem Mater 1996;8:525-34.

[247] Ramesh KV, Sastry DL. Transport properties of ZnO substituted lead vanadate glass system at eutectic composition. Mat Sci Eng B 2006;126:66-73.

[248] Beke S. A review of the growth of V_2O_5 films from 1885 to 2010. Thin Solid Films 2011;519:1761-71.

[249] Chirayil T, Zavalij PY, Whittingham MS. Hydrothermal synthesis of vanadium oxides. Chem Mater 1998;10:2629-40.

[250] Pan D, Shuyuan Z, Chen Y, Hou J. Hydrothermal preparation of long nanowires of vanadium oxide. J Mater Res 2002;17:1981-4.

[251] Takahashi K, Limmer SJ, Wang Y, Cao G. Synthesis and electrochemical properties of single-crystal V2O5 nanorod arrays by template-based electrodeposition. J Phys Chem B 2004;108:9795-800.

[252] Takahashi K, Limmer SJ, Cao G. Template-based growth of V2O5 nanorods by electrodeposition. Optical Science and Technology, SPIE's 48th Annual Meeting: Inter Soc Opt and Phot 2003. p. 33-42.

[253] Stefanovich G, Pergament A, Velichko A, Stefanovich L. Anodic oxidation of vanadium and properties of vanadium oxide films. J Phys Cond Mat 2004;16:4013.

[254] Navone C, Pereira-Ramos J, Baddour-Hadjean R, Salot R. High-capacity crystalline V2O5 thick films prepared by RF sputtering as positive electrodes for rechargeable lithium microbatteries. J Electrochem Soc 2006;153:A2287-A93.

[255] Badot J-C, Mantoux A, Baffier N, Dubrunfaut O, Lincot D. Electrical properties of V2O5 thin films obtained by atomic layer deposition (ALD). J Mater Chem 2004;14:3411-5.

[256] Ramana C, Smith R, Hussain O, Julien C. Growth and surface characterization of V2O5 thin films made by pulsed-laser deposition. J Vac Sci Technol A 2004;22:2453-8.

[257] Barreca D, Armelao L, Caccavale F, Di Noto V, Gregori A, Rizzi GA, et al. Highly oriented V2O5 nanocrystalline thin films by plasma-enhanced chemical vapor deposition. Chem Mater 2000;12:98-103.

[258] Barreca D, Massignan C, Daolio S, Fabrizio M, Piccirillo C, Armelao L, et al. Composition and microstructure of cobalt oxide thin films obtained from a novel cobalt(II) precursor by chemical vapor deposition. Chem Mater 2001;13:588-93.

[259] Wollenstein J, Burgmair M, Plescher G, Sulima T, Hildenbrand J, Bottner H, et al. Cobalt oxide based gas sensors on silicon substrate for operation at low temperatures. Sensors Actuat B-Chem. 2003;93:442-8.

[260] Kowalski K, Ijjaali M, Bak T, Dupre B, Gleitzer C, Nowotny J, et al. Semiconducting Properties of CoO Thin Films. Ionics. 2001;7:394-9.

[261] Tong XC. Thermoelectric Cooling Through Thermoelectric Materials. Adv Mater for Thermal Manag Electron Pack 2011. p. 477-525.

[262] Lee M, Viciu L, Li L, Wang YY, Foo ML, Watauchi S, et al. Large enhancement of the thermopower in Na_xCoO_2 at high Na doping. Nat Mater 2006;5:537-40.

[263] Nagira T, Ito M, Katsuyama S, Majima K, Nagai H. Thermoelectric properties of $(Na_{1-y}M_y)_xCo_2O_4$(M= K, Sr, Y, Nd, Sm and Yb; y= 0.01- 0.35). J. Alloy. Compd. 2003;348:263-9.

[264] Kim JY, Kim JI, Seo WS. Exfoliation Route to Nanostructured Cobalt Oxide with Enhanced Thermoelectric Performance. Appl Phys Exp 2011;4.

[265] Kim J-Y, Kim J-I, Choi S-M, Lim YS, Seo W-S, Hwang HJ. Nanostructured thermoelectric cobalt oxide by exfoliation/restacking route. J Appl Phys 2012;112:113705-8.

[266] Wang Y, Sui Y, Cheng J, Wang X, Su W. Comparison of the high temperature thermoelectric properties for Ag-doped and Ag-added $Ca_3Co_4O_9$. J Alloy Compd 2009;477:817-21.

[267] Zhang F, Lu Q, Zhang J. Synthesis and high temperature thermoelectric properties of $Ba_xAg_yCa_{3-x-y}Co_4O_9$ compounds. J Alloy Compd 2009;484:550-4.

[268] Song Y, Sun Q, Zhao L, Wang F, Jiang Z. Synthesis and thermoelectric power factor of $(Ca_{0.95}Bi_{0.05})_3Co_4O_9$/Ag composites. Mater Chem Phys 2009;113:645-9.

[269] Wang Y, Sui Y, Cheng J, Wang X, Su W. Efficient room temperature thermoelectric characteristics of $Ca_{3-x}Ag_xCo_4O_{9+\delta}/Ag_y$ composites. J Phys D: Appl Phys 2008;41:045406.

[270] Matsubara I, Funahashi R, Takeuchi T, Sodeoka S. Thermoelectric properties of spark plasma sintered $Ca_{2.75}Gd_{0.25}Co_4O_9$ ceramics. J Appl Phys 2001;90:462-5.

[271] Yao Q, Wang D, Chen L, Shi X, Zhou M. Effects of partial substitution of transition metals for cobalt on the high-temperature thermoelectric properties of $Ca_3Co_4O_{9+\delta}$. J Appl Phys 2005;97:103905--5.

[272] Wang Y, Sui Y, Wang X, Su W, Liu X. Enhanced high temperature thermoelectric characteristics of transition metals doped $Ca_3Co_4O_{9+\delta}$ by cold high-pressure fabrication. J Appl Phys 2010;107:033708--9.

[273] Nong N, Liu CJ, Ohtaki M. Improvement on the high temperature thermoelectric performance of Ga-doped misfit-layered $Ca_3Co_{4-x}Ga_xO_{9+\delta}$(x= 0, 0.05, 0.1, and 0.2). J Alloy Compd 2010;491:53-6.

[274] Sugiura K, Ohta H, Nomura K, Hirano M, Hosono H, Koumoto K. High electrical conductivity of layered cobalt oxide $Ca_3Co_4O_9$ epitaxial films grown by topotactic ion-exchange method. Appl Phys Lett 2006;89:032111.

[275] Sugiura K, Ohta H, Nomura K, Hirano M, Hosono H, Koumoto K. Fabrication and thermoelectric properties of layered cobaltite, gamma-$Sr_{0.32}Na_{0.21}CoO_2$ epitaxial films. Appl Phys Lett 2006;88.

[276] Wang G, Shen X, Horvat J, Wang B, Liu H, Wexler D, et al. Hydrothermal synthesis and optical, magnetic, and supercapacitance properties of nanoporous cobalt oxide nanorods. J Phys Chem C 2009;113:4357-61.

[277] Shao Y, Sun J, Gao L. Hydrothermal Synthesis of Hierarchical Nanocolumns of Cobalt Hydroxide and Cobalt Oxide. J Phys Chem C 2009;113:6566-72.

[278] Xie XW, Shen WJ. Morphology control of cobalt oxide nanocrystals for promoting their catalytic performance. Nanoscale. 2009;1:50-60.

[279] Casella IG. Electrodeposition of cobalt oxide films from carbonate solutions containing Co (II)–tartrate complexes. Journal of Electroanalytical Chemistry. 2002;520:119-25.

[280] Grillo ME. Stability of corundum- versus rutile-type structures of ruthenium and rhodium oxides. Phys Rev B 2004;70.

[281] Music S, Saric A, Popovic S, Ivanda M. Formation and characterisation of nanosize alpha-Rh_2O_3 particles. J Molec Str 2009;924-26:221-4.

[282] Watson P, Somorjai G. The hydrogenation of carbon monoxide over rhodium oxide surfaces. J Catal 1981;72:347-63.

[283] Dautremont-Smith W. Transition metal oxide electrochromic materials and displays: a review: Part 2: oxides with anodic coloration. Displays. 1982;3:67-80.

[284] Ligthart DAJM, van Santen RA, Hensen EJM. Supported Rhodium Oxide Nanoparticles as Highly Active CO Oxidation Catalysts. Angew Chem Int Edit 2011;50:5306-10.

[285] Koshibae W, Tsutsui K, Maekawa S. Thermopower in cobalt oxides. Phys Rev B 2000;62:6869-72.

[286] Okada S, Terasaki I. Physical properties of Bi-based rhodium oxides with RhO_2 hexagonal layers. Jpn J Appl Phys Part 1-Reg Papers Brief Commun Rev Pap 2005;44:1834-7.

[287] Okada S, Sakai A, Kanno T, Yotsuhashi S, Adachi H. Thermoelectric properties of bismuth based cobalt-rhodium oxides with hexagonal $(Co,Rh)O_2$ layers. J Appl Phys 2009;105.

[288] Kobayashi W, Tamura W, Terasaki I. Thermal conductivity of thermoelectric rhodium oxides measured by a modified Harman method. J Phys Soc Jpn 2008;77.

[289] Saeed Y, Singh N, Schwingenschlögl U. Colossal Thermoelectric Power Factor in $K_{7/8}RhO_2$. Adv Funct Mater 2012;22:2792-6.

[290] Wang HH, Yan MM, Jiang ZY. Electrochromic properties of rhodium oxide films prepared by a sol-gel method. Thin Solid Films 2001;401:211-5.

[291] Wang HH, Zhao CJ, Yan MM, Jiang ZY. Preparation of rhodium oxide films and its electrochromic study. Acta Chim Sin 2002;60:1203-8.

[292] Moran-Miguelez E, Alario-Franco M. Hydrothermal synthesis and reactivity of rhodium dioxide and oxyhydroxide. Thermochimica Acta 1983;60:181-6.

[293] Marot L, Mathys D, Temmerman GD, Oelhafen P. Characterization of sub-stoichiometric rhodium oxide deposited by magnetron sputtering. Surf Sci 2008;602:3375-80.

[294] Muller O, Roy R. Formation and stability of the platinum and rhodium oxides at high oxygen pressures and the structures of Pt_3O_4, β-PtO_2 and RhO_2. J Less Common Metals. 1968;16:129-46.

[295] Yao JN, Hashimoto K, Fujishima A. Photochromism induced in an electrolytically pretreated MoO_3 thin film by visible light. Nature. 1992;355:624-6.

[296] He T, Yao JN. Photochromism in composite and hybrid materials based on transition-metal oxides and polyoxometalates. Prog Mater Sci 2006;51:810-79.

[297] Azad AM, Mhaisalkar SG, Birkefeld LD, Akbar SA, Goto KS. Behavior of a new ZrO_2-MoO_3 sensor for carbon-monoxide detection. J Electrochem Soc 1992;139:2913-20.

[298] Ouyang QY, Li L, Wang QS, Zhang Y, Wang TS, Meng FN, et al. Facile synthesis and enhanced H_2S sensing performances of Fe-doped alpha-MoO_3 micro-structures. Sensors Actuat B-Chem 2012;169:17-25.

[299] Zhao DW, Sun XW, Jiang CY, Kyaw AKK, Lo GQ, Kwong DL. Efficient tandem organic solar cells with an Al/MoO_3 intermediate layer. Appl Phys Lett 2008;93.

[300] Cattin L, Dahou F, Lare Y, Morsli M, Tricot R, Houari S, et al. MoO_3 surface passivation of the transparent anode in organic solar cells using ultrathin films. J Appl Phys 2009;105.

[301] Zhang FJ, Xu XW, Tang WH, Zhang J, Zhuo ZL, Wang J, et al. Recent development of the inverted configuration organic solar cells. Sol Energy Mat Sol C 2011;95:1785-99.

[302] Balendhran S, Walia S, Nili H, Ou JZ, Zhuiykov S, Kaner RB, et al. Two-Dimensional Molybdenum Trioxide and Dichalcogenides. Adv Funct Mater 2013:10.1002/adfm.201300125.

[303] Carcia PF, McCarron EM. Synthesis and properties of thin-film polymorphs of molybdenum trioxide Thin Solid Films. 1987;155:53-63.

[304] Di Yao D, Ou JZ, Latham K, Zhuiykov S, O'Mullane AP, Kalantar-zadeh K. Electrodeposited alpha- and beta-Phase MoO3 Films and Investigation of Their Gasochromic Properties. Cryst Growth Des 2012;12:1865-70.

[305] Kalantar-zadeh K, Tang JS, Wang MS, Wang KL, Shailos A, Galatsis K, et al. Synthesis of nanometre-thick MoO_3 sheets. Nanoscale 2009;2:429-33.

[306] Scanlon DO, Watson GW, Payne DJ, Atkinson GR, Egdell RG, Law DSL. Theoretical and Experimental Study of the Electronic Structures of MoO_3 and MoO_2. J Phys Chem C 2010;114:4636-45.

[307] Scanlon DO, Watson GW, Payne D, Atkinson G, Egdell R, Law D. Theoretical and Experimental Study of the Electronic Structures of MoO_3 and MoO_2. J Phys Chem C 2010;114:4636-45.

[308] Xu JX, Sonne M, Pryds N, Kleinke H. Thermoelectric properties of molybdenum oxides $LnMo_{(8)}O_{(14)}$ (Ln = La, Ce, Pr, Nd and Sm). J Alloy Compd 2010;489:353-6.

[309] Xu JX, Sonne M, Yanangiya SI, Van Nong N, Pryds N, Nygren M, et al. High thermoelectric performance of reduced lanthanide molybdenum oxides densified by spark plasma sintering. J Alloy Compd 2010;500:22-5.

[310] Anilkumar KR, Parveen A, Badiger GR, Prasad M. Thermoelectric Power Factor for Polyaniline/Molybdenum Trioxide Composites. Ferroelectrics 2009;386:88-93.

[311] Mulenko SA. Synthesis of nanometric iron and chromium oxide films by reactive pulsed laser deposition for photo-thermo sensors. In: Veiko VP, Vartanyan TA, editors. Fundamentals of Laser-Assisted Micro- and Nanotechnologies 2010. Bellingham: Spie-Int Soc Optical Engineering; 2011.

[312] Sugihara S, Suzuki C, Kameya R. High thermoelectric performance of metal substituted samples of α Fe_2O_3 and computation of their electronic structures by the DVXα method. Inter J Quantum Chem 2009;109:2788-92.

[313] Rajendran S, Rao VS. An anomalous behaviour in the phase stability of the system Fe2O3 and NiO. J Mater Sci 1994;29:5673-9.

[314] Vayssieres L, Sathe C, Butorin SM, Shuh DK, Nordgren J, Guo J. One-Dimensional Quantum-Confinement Effect in α-Fe_2O_3 Ultrafine Nanorod Arrays. Adv Mater 2005;17:2320-3.

[315] Maldonado F, Novillo C, Stashans A. Ab initio calculation of chromium oxide containing Ti dopant. Chem Phys 2012;393:148-52.

[316] Young EWA, Gerretsen JH, Dewit JHW. The oxygen partial pressure dependence of the defect structure of chromium(III) oxide. J Electrochem Soc 1987;134:2257-60.

[317] Nagai H, Ohbayashi K. Effect of TiO_2 on the Sintering and the Electrical Conductivity of Cr_2O_3. J Am Ceram Soc 1989;72:400-3.

[318] Hayashi K, Sato K, Nozaki T, Kajitani T. Effect of doping on thermoelectric properties of delafossite-type oxide $CuCrO_2$. Jpn J Appl Phys 2008;47:59-63.

[319] Tomes P, Logvinovich D, Hejtmanek J, Aguirre MH, Weidenkaff A. Magnetic influence on thermoelectric properties of $CrO_{0.1}N_{0.9}$. Acta Mater 2011;59:1134-40.

[320] Kakehi Y, Satoh K, Yotsuya T, Ashida A, Yoshimura T, Fujimura N. Electrical and optical properties of excess oxygen intercalated $CuScO_2(0001)$ epitaxial films prepared by oxygen radical annealing. Thin Solid Films. 2008;516:5785-9.

[321] Zhuiykov S. Electrochemistry of zirconia gas sensors: CRC Press; 2010.

[322] Zandiehnadem F, Murray RA, Ching WY. Electronic structures of three phases of zirconium oxide. Physica B,C. 1988;150:19-24.

[323] Jefferson PH, Hatfield S, Veal TD, King P, McConville CF, Zúñiga-Pérez J, et al. Bandgap and effective mass of epitaxial cadmium oxide. Appl Phys Lett 2008;92:022101--3.

[324] Gurumurugan K, Mangalaraj D, Narayandass SK, Nakanishi Y. DC reactive magnetron sputtered CdO thin films. Mater Lett 1996;28:307-12.

[325] Wright R. The Variation with Temperature of the Electrical Properties of a Degenerate Electronic Semiconductor as exemplified by Cadmium Oxide. P Phys Soc S-A. 2002;64:350.

[326] Salunkhe RR, Dhawale DS, Gujar TP, Lokhande CD. Structural, electrical and optical studies of SILAR deposited cadmium oxide thin films: Annealing effect. Mater Res Bull 2009;44:364-8.

[327] Gurumurugan K, Mangalaraj D, Narayandass SK, Sekar K, Vallabhan CG. Characterization of transparent conducting CdO films deposited by spray pyrolysis. Semicond Sci Tech 1999;9:1827.

[328] Li B, Zhang J. Electrical Conductivity of Cadmium Oxide—Antimony Oxide System Ceramics. J Am Ceram Soc 1989;72:2377-80.

[329] Irwin MD, Buchholz DB, Hains AW, Chang RP, Marks TJ. p-Type semiconducting nickel oxide as an efficiency-enhancing anode interfacial layer in polymer bulk-heterojunction solar cells. P Natl Acad Sci USA. 2008;105:2783-7.

[330] Parravano G. Thermoelectric Behavior of Nickel Oxide. J Chem Phys 1955;23:5.

[331] Patil PS, Kadam LD. Preparation and characterization of spray pyrolyzed nickel oxide (NiO) thin films. Appl Surf Sci 2002;199:211-21.

[332] Shin W, Murayama N. Li-doped nickel oxide as a thermoelectric material. Japanese Journal of Appl Phys 1999;38:L1336-L8.

[333] Dutt MB, Banerjee R, Barua AK. Transport properties of Lithium and Sodium doped Nickel oxide. Physica Status Solidi a-Appl Res 1981;65:365-70.

[334] Keawprak N, Tu R, Goto T. Thermoelectricity of $CaIrO_3$ ceramics prepared by spark plasma sintering. J Cer Soc Jpn 2009;117:466-9.

[335] Keawprak N, Tu R, Goto T. Thermoelectric Properties of Ca-Ir-O Compounds Prepared by Spark Plasma Sintering. Mater Trans 2009;50:853-8.

[336] Keawprak N, Tu R, Goto T. Thermoelectric properties of Sr–Ir–O compounds prepared by spark plasma sintering. J Alloy Compd 2010;491:441-6.

[337] Macklin WJ, Moseley PT. On the use of oxides for thermoelectric refrigeration. Mat Sci Eng B 1990;7:111-7.

[338] Androulakis J, Migiakis P, Giapintzakis J. $La_{0.95}Sr_{0.05}CoO_3$: An efficient room-temperature thermoelectric oxide. Arxiv preprint cond-mat/0312670. 2003.

[339] Gross AJ, Hwang GS, Huang BL, Yang HX, Ghafouri N, Kim H, et al. Multistage Planar Thermoelectric Microcoolers. J Microelectromech S 2011;20:1201-10.

[340] Yang RQ, Hill CJ, Mansour K, Qiu YM, Soibel A, Muller RE, et al. Distributed feedback mid-IR interband cascade lasers at thermoelectric cooler temperatures. IEEE Jour Sel Topics in Quantum Electronics. 2007;13:1074-8.

[341] DiSalvo FJ. Thermoelectric cooling and power generation. Science 1999;285:703-6.

[342] Chein R, Huang GM. Thermoelectric cooler application in electronic cooling. Appl Therm Eng 2004;24:2207-17.

[343] Sharp J, Bierschenk J, Lyon HB. Overview of solid-state thermoelectric refrigerators and possible applications to on-chip thermal management. Proceedings of the IEEE 2006;94:1602-12.

[344] Venkatasubramanian R, Siivola E, Colpitts T, O'Quinn B. Thin-film thermoelectric devices with high room-temperature figures of merit. Nature. 2001;413:597-602.

[345] Macklin W, Moseley P. On the use of oxides for thermoelectric refrigeration. Mat Sci Eng B 1990;7:111-7.

[346] Jeffrey WF. Oxide materials for high temperature thermoelectric energy conversion. J Eur Ceram Soc 2012;32.

[347] Ohtaki M. Recent aspects of oxide thermoelectric materials for power generation from mid-to-high temperature heat source. J Ceram Soc Jpn 2011;119:770-5.

[348] Doumerc JP, Blangero M, Pollet M, Carlier D, Darriet J, Delmas C, et al. Transition metal oxides for thermoelectric generation. In: Lin HT, Koumoto K, Kriven WM, Garcia E, Reimanis IE, Norton DP, et al., editors. Developments in Strategic Materials. Westerville: Amer Ceramic Soc 2009: 25-40.

[349] Kawamoto H. R & D Trends in High Efficiency Thermoelectric Conversion Materials for Waste Heat Recovery. Science & Technology Trends 2009:54-69.

[350] Shin W, Murayama N, Ikeda K, Sago S. Fabrication of oxide thermoelectric generator element. Jpn. J. Appl. Phys. Part 1 - Regul. Pap. Short Notes Rev Pap 2000;39:1254-5.

[351] Shin W, Murayama N, Ikeda K, Sago S. Thermoelectric power generation using Li-doped NiO and (Ba, Sr) PbO_3 module. J Power Sour 2001;103:80-5.

[352] Matsubara I, Funahashi R, Takeuchi T, Sodeoka S, Shimizu T, Ueno K. Fabrication of an all-oxide thermoelectric power generator. Appl Phys Lett 2001;78:3627-9.

[353] Funahashi R, Urata S, Mizuno K, Kouuchi T, Mikami M. CaBiCoO∕ LaBiNiO thermoelectric devices with high output power density. Appl Phys Lett 2004;85:1036.

[354] Funahashi R, Mikami M, Mihara T, Urata S, Ando N. A portable thermoelectric-power-generating module composed of oxide devices. J Appl Phys 2006;99.

[355] Funahashi R, Urata S. Fabrication and application of an oxide thermoelectric system. Int. J Appl Ceram Technol 2007;4:297-307.

[356] Kosuga A, Urata S, Kurosaki K, Yamanaka S, Funahashi R. Mechanical Properties of $Ca_{0.9}Yb_{0.1}MnO_3$/Ag Composites for n-Type Legs of Thermoelectric Oxide Devices. Jpn J Appl Phys 2008;47:6399-403.

[357] Reddy ES, Noudem J, Hebert S, Goupil C. Fabrication and properties of four-leg oxide thermoelectric modules. J Physics D: Appl Phys 2005;38:3751.

[358] Noudem JG, Lemonnier S, Prevel M, Reddy ES, Guilmeau E, Goupil C. Thermoelectric ceramics for generators. J Eur Ceram Soc 2008;28.

[359] Su HM, Jiang Y, Lan XZ, Liu XM, Zhong HH, Yu DB. $Ca_{3-x}Bi_xCo_4O_9$ and $Ca_{1-y}Sm_yMnO_3$ thermoelectric materials and their power-generation devices. Phys Status Solidi A-Appl Mat 2011;208:147-55.

[360] Lim CH, Choi SM, Seo WS, Park HH. A Power-Generation Test for Oxide-Based Thermoelectric Modules Using p-Type $Ca_3Co_4O_9$ and n-Type $Ca_{0.9}Nd_{0.1}MnO_3$ Legs. J Electron Mater 2012;41:1247-55.

[361] Souma T, Ohtaki M, Ohnishi K, Shigeno M, Ohba Y, Shimozaki T. Power generation characteristics of oxide thermoelectric modules incorporating nanostructured ZnO sintered

materials. In: Kim I, editor. Proceedings Ict 07: Twenty-Sixth International Conference on Thermoelectrics. New York: IEEE 2008. 38-41.

[362] Tomes P, Trottmann M, Suter C, Aguirre MH, Steinfeld A, Haueter P, et al. Thermoelectric Oxide Modules (TOMs) for the Direct Conversion of Simulated Solar Radiation into Electrical Energy. Materials 2010;3:2801-14.

[363] Choi SM, Lee KH, Lim CH, Seo WS. Oxide-based thermoelectric power generation module using p-type $Ca_3Co_4O_9$ and n-type $(ZnO)_{(7)}In_2O_3$ legs. Energy Conv Manag 2011;52:335-9.

[364] Tritt TM, Boettner H, Chen L. Thermoelectrics: Direct solar thermal energy conversion. MRS Bull 2008;33:366-8.

[365] Telkes M. Solar thermoelectric generators. J Appl Phys 1954;25:765-77.

[366] Robert R, Romer S, Reller A, Weidenkaff A. Nanostructured complex cobalt oxides as potential materials for solar thermoelectric power generators. Adv Eng Mater 2005;7:303-8.

[367] Robert R, Bocher L, Sipos B, Döbeli M, Weidenkaff A. Ni-doped cobaltates as potential materials for high temperature solar thermoelectric converters. Prog Solid State Ch 2007;35:447-55.

[368] Lange RG, Carroll WP. Review of recent advances of radioisotope power systems. Energy Conv Manag 2008;49:393-401.

[369] Williams HR, Ambrosi RM, Bannister NP, Samara-Ratna P, Sykes J. A conceptual spacecraft radioisotope thermoelectric and heating unit (RTHU). Int J Energ Res 2012;36:1192-200.

[370] O'Brien RC, Ambrosi RM, Bannister NP, Howe SD, Atkinson HV. Safe radioisotope thermoelectric generators and heat sources for space applications. J Nucl Mater 2008;377:506-21.

[371] Singh R, Tundee S, Akbarzadeh A. Electric power generation from solar pond using combined thermosyphon and thermoelectric modules. Sol Energy 2011;85:371-8.

[372] Rajendra Kumar RT, Karunagaran B, Mangalaraj D, Narayandass SK, Manoravi P, Joseph M, et al. Pulsed laser deposited vanadium oxide thin films for uncooled infrared detectors. Sensors Actuat A - Phys 2003;107:62-7.

[373] Ha T-J, Park H-H, Jung S-Y, Yoon S-J, Kim J-S, Jang HW. Effect of porosity on the Seebeck coefficient of mesoporous TiO_2 thin films. Thin Solid Films 2010;518:7196-8.

[374] Roediger T, Knauss H, Gaisbauer U, Kraemer E, Jenkins S, von Wolfersdorf J. Time-resolved heat transfer measurements on the tip wall of a ribbed channel using a novel heat flux sensor-part I: Sensor and benchmarks. J turbomach 2008;130.

[375] Yang Y, Pradel KC, Jing Q, Wu JM, Zhang F, Zhou Y, et al. Thermoelectric Nanogenerators Based on Single Sb-Doped ZnO Micro/Nanobelts. Acs Nano. 2012;6:6984-9.

[376] Janata J, Bezegh A. Chemical sensors. Anal chem 1988;60:62R-74R.

[377] Matsumiya M, Qiu F, Shin W, Izu N, Matsubara I, Murayama N, et al. Thermoelectric CO Gas Sensor Using Thin-Film Catalyst of Au and Co_3O_4. J Electrochem Soc 2004;151:H7-H10.

[378] Rettig F, Moos R. Direct thermoelectric gas sensors: Design aspects and first gas sensors. Sensors Actuat B - Chem. 2007;123:413-9.

[379] Nishibori M, Shin W, Tajima K, Houlet LF, Izu N, Itoh T, et al. Thermoelectric gas sensor using Au loaded titania CO oxidation catalyst. J Ceram Soc Jap 2007;115:37-41.

[380] Shin W, Matsumiya M, Izu N, Murayama N. Hydrogen-selective thermoelectric gas sensor. Sensors and Actuators B: Chem 2003;93:304-8.

[381] Sadek AZ, Choopun S, Wlodarski W, Ippolito SJ, Kalantar-zadeh K. Characterization of ZnO Nanobelt-Based Gas Sensor for H_2, NO_2 and Hydrocarbon sensing. Sensors Journal, IEEE 2007;7:919-24.

[382] Wang Z. Novel nanostructures of ZnO for nanoscale photonics, optoelectronics, piezoelectricity, and sensing. Appl Phys A 2007;88:7-15.

[383] Simon I, Bârsan N, Bauer M, Weimar U. Micromachined metal oxide gas sensors: opportunities to improve sensor performance. Sensors Actuat B - Chem 2001;73:1-26.

[384] Vanherwaarden AW, Sarro PM. Thermal sensors based on the Seebeck effect. Sensor Actuator 1986;10:321-46.

[385] Darling RB, Iwanaga S. Structure, properties, and MEMS and microelectronic applications of vanadium oxides. Sadhana 2009;34:531-42.

[386] Choi W, Abrahamson JT, Strano JM, Strano MS. Carbon nanotube-guided thermopower waves. Mater Today 2010;13:22-33.

[387] Hong S, Kim W, Jeon S-J, Lim SC, Lee H-J, Hyun S, et al. Enhanced Electrical Potential of Thermoelectric Power Waves by Sb_2Te_3-Coated Multiwalled Carbon Nanotube Arrays. J Phys Chem C 2013.

Figure captions

Fig. 1. Operating temperature ranges of various TMOs and TMO composites. (Reproduced with permission from [15].)

Fig. 2. (a) A 2D quantum well structure with width W, (b) 1D conductor (nanowire) with a square cross section of width a, (c) a segmented nanowire superlattice of diameter d_w comprising of quantum dots (0D) of alternating materials A and B, with respective segment lengths L_A and L_B. (d) Energy dependence of the electronic DOS in 3D, 2D, 1D and 0D materials. ((c), (d) Reproduced with permission from [28] and [29].)

Fig. 3. Schematic depiction of the substructuring approach in doped cobalt oxide, comprising of ordered CoO_2 layers that are separated by disordered layers (of Na dopant) to achieve a good electrical conductivity and poor phonon conductivity. (Reproduced with permission from[42].)

Fig. 4. (a) Seebeck coefficient (red) and electrical resistivity (blue) of reduced single crystal rutile TiO_x as a function of annealing temperature and (b) Seebeck coefficient as a function of temperature for a sample annealed in H_2 at 1053 K. (Reproduced with permission from [125].)

Fig. 5. (a) Electrical conductivity, (b) Seebeck coefficient, (c) thermal conductivity, (d) TPF and (e) ZT *vs* temperature for different concentrations of La dopant in STO thin films. (Reproduced with permission from [134].)

Fig. 6. (a) Resistivity, (b) Seebeck coefficient, (c) TPF and (d) ZT of GPR (red) and SSR synthesised (black) Yb-doped $CaMnO_3$ nanoparticles (Reproduced from [22].)

Fig. 7. (a) Seebeck coefficient, (b) electrical conductivity variation with temperature for α-WO_3 films and (c) TPF obtained for varying ZnO doping concentrations in WO_3 ceramics. (Reproduced with permission from (a), (b) [168] and (c) [161].)

Fig. 8. Temperature dependence of TPF of Zn$_{1-x-y}$Al$_x$Ga$_y$O ceramics. (Reproduced with permission from [88].)

Fig. 9. (a) Electrical conductivity variation of CuO sintered at different temperatures, (b) Seebeck coefficient variation with temperature for CuO films of different thicknesses and (c) Temperature dependence of TPF for various La$_2$CuO$_4$ ceramics, (inset shows ZT values at 330 K) [LNCO (Nb doped La$_2$CuO$_4$), LPCO (Pr doped La$_2$CuO$_4$), LYCO (Y doped La$_2$CuO$_4$)]. (Reproduced with permission from (a) [222], (b)[226] and (c) [221].)

Fig. 10. Temperature dependence of (a) electrical conductivity, (b) Seebeck coefficient for the as-cast and heat treated films during heating and cooling cycles of hydrated V$_2$O$_5$. (Reproduced with permission from [244].)

Fig. 11. (a) Resistivity and (b) Seebeck coefficient variations with temperature for NaCo$_2$O$_4$ single crystals in plane (ρ_a) and out of plane (ρ_c) and (c) comparison of ZT and TPF for SPS and hot pressed (HP) synthesised Ca$_{2.75}$Gd$_{0.25}$Co$_4$O$_9$ samples. (Reproduced with permission from (a), (b) [11] and (c) [270].)

Fig. 12. Temperature (*T*) dependence of (a) resistivity (ρ), (b) Seebeck coefficient (*S*), and (c) thermal conductivity (κ) for Bi$_{1.7}$Ba$_2$(Co$_{1-z}$Rh$_z$)O$_y$ of varying rhodium concentration (*z*) (Reproduced with permission from [287].)

Fig. 13. (a) Temperature dependence of TPF of RMo$_8$O$_{14}$ (R:La, Ce, Nd, Sm) pellets, and (b) electrical conductivity *vs* TPF of PANI/MoO$_3$ composites *vs* MoO$_3$ concentration in the composite. (Reproduced with permission from (a) [309] and (b) [310].)

Fig. 14. Pictorial representation of a TE cooling device. (Reproduced with permission from [261].)

Fig. 15. Schematic of a solar thermoelectric generator (STEG), comprising of a solar concentrator and both p and n type TE elements. (Reproduced with permission from[371].)

Fig. 16. (a) Schematic of thin film thermopower wave system and output voltage profiles for (b) ZnO and (c) MnO$_2$ based thermopower wave sources. (Reproduced with permission from (b) [5] and (c) [9].)